ČESKÉ VYSOKÉ UČENÍ TECHNICKÉ V PRAZE
FAKULTA JADERNÁ A FYZIKÁLNĚ INŽENÝRSKÁ
KATEDRA DOZIMETRIE A APLIKACE IONIZUJÍCÍHO ZÁŘENÍ

BAKALÁŘSKÁ PRÁCE

Produkce mezonů na experimentu COMPASS, kalibrace detektoru Straw

Autor: Eliška Jelínková
Vedoucí: Ing. Kamil Augsten, Ph.D.
Praha, 2021

CZECH TECHNICAL UNIVERSITY IN PRAGUE

FACULTY OF NUCLEAR SCIENCES AND PHYSICAL ENGINEERING

DEPARTMENT OF DOSIMETRY AND APPLICATION OF IONIZING RADIATION

BACHELOR'S THESIS

Meson production at the COMPASS experiment, calibration of the Straw detector

Author: Eliška Jelínková

Supervisor: Ing. Kamil Augsten, Ph.D.

Prague, 2021

ČESKÉ VYSOKÉ UČENÍ TECHNICKÉ V PRAZE
FAKULTA JADERNÁ A FYZIKÁLNĚ INŽENÝRSKÁ
PRAHA 1 - STARÉ MĚSTO, BŘEHOVÁ 7 - PSČ 115 19

Katedra: KDAIZ *Akademický rok:* 2020/2021

ZADÁNÍ BAKALÁŘSKÉ PRÁCE

Student:	Eliška Jelínková
Studijní program:	Aplikace přírodních věd
Obor:	Dozimetrie a aplikace ionizujícího záření
Název práce: (česky)	Produkce mezonů na experimentu COMPASS, kalibrace detektoru Straw
Název práce: (anglicky)	Meson production at the COMPASS experiment, calibration of the Straw detector

Pokyny pro vypracování:

1. Vypracujte rešerši na téma experimentu COMPASS – princip experimentu a systém detektorů.
2. Podrobněji se seznamte s detektorem Straw a v práci popište.
3. Seznamte se s fyzikálním programem experimentu COMPASS a v práci se zaměřte především na mionovou produkci mezonů.
4. Ověřte kalibraci detektoru Straw pro run 2021 – popište, jak se plynové dráhové detektory toho typu kalibrují v RT závislosti.

Doporučená literatura:

[1] ŽÁČEK, J. *Úvod do fyziky elementárních částic*, Karolinum 2005.

[2] ZYLA, P. A., R. M. BARNETT, J. BERINGER, et al. Review of Particle Physics. *Progress of Theoretical and Experimental Physics*. 2020, **2020**(8). ISSN 2050-3911. DOI:10.1093/ptep/ptaa104.

[3] ABBON, P., E. ALBRECHT, V.Yu. ALEXAKHIN, et al. The COMPASS experiment at CERN. *Nuclear Instruments and Methods in Physics Research Section A: Accelerators, Spectrometers, Detectors and Associated Equipment*. 2007, **577**(3), 455-518. ISSN 01689002. DOI:10.1016/j.nima.2007.03.026.

[4] BYCHKOV, V.N., N. DEDEK, W. DÜNNWEBER, et al. The large size straw drift chambers of the COMPASS experiment. *Nuclear Instruments and Methods in Physics Research Section A: Accelerators, Spectrometers, Detectors and Associated Equipment*. 2006, **556**(1), 66-79. ISSN 01689002. DOI:10.1016/j.nima.2005.10.026

[5] COMPASS Collaboration. *COMPASS-II Proposal*, CERN-SPSC-2010-014 SPSC-P340.

Jméno a pracoviště vedoucího bakalářské práce:

Ing. Kamil Augsten, Ph.D.
České vysoké učení technické v Praze
Fakulta jaderná a fyzikálně inženýrská
Katedra dozimetrie a aplikace ionizujícího záření
Břehová 7
115 19 Praha 1

Jméno a pracoviště konzultanta bakalářské práce:

Datum zadání bakalářské práce: 15.10.2020

Termín odevzdání bakalářské práce: 7.7.2021

Doba platnosti zadání je dva roky od data zadání.

.....	.....	.....
garant oboru	*vedoucí katedry*	*děkan*

V Praze dne 15.10.2020

Prohlášení

Prohlašuji, že jsem svou bakalářskou práci vypracovala samostatně a použila jsem pouze podklady uvedené v přiloženém seznamu.

V Praze .....

.....
Eliška Jelínková

Poděkování

Děkuji vedoucímu mé bakalářské práce Ing. Kamilovi Augstenovi, PhD. za cenné rady a za trpělivost a ochotu při konzultacích a vypracování práce.

Eliška Jelínková

Název práce: **Produkce mezonů na experimentu COMPASS, kalibrace detektoru Straw**

Autor: Eliška Jelínková

Obor: Dozimetrie a aplikace ionizujícího záření

Druh práce: Bakalářská práce

Vedoucí práce: Ing. Kamil Augsten, Ph.D., Katedra dozimetrie a aplikace ionizujícího záření, Fakulta jaderná a fyzikálně inženýrská, České vysoké učení technické v Praze

Konzultant: —

Abstrakt: Tato práce se zabývá terčovým experimentem COMPASS, který je součástí CERN (Evropské organizace pro jaderný výzkum). Fyzikální program experimentu COMPASS je zaměřen na výzkum struktury hadronů a hadronovou spektroskopii. Pro tento účel jsou studovány výlučné procesy, jako jsou např. mezonové produkce a hluboce virtuální Comptonův rozptyl. Ty lze měřit pomocí rozsáhlého spektrometru tvořeného mnoha detektory. Jedním z nich je detektor Straw skládající se z trubičkových driftových komor. Kalibrace jeho RT závislosti pro rok 2021 byla ověřena pomocí dat z roku 2018. Dále byl proveden výpočet z měření survey z roku 2021, který slouží určení polohy detektoru, což je základní požadavek pro úspěšnou kalibraci a co nejvyšší účinnost při dráhové rekonstrukci.

Klíčová slova: COMPASS, detektor Straw, produkce mezonů, kalibrace RT závislosti, měření survey

Title: **Meson production at the COMPASS experiment, calibration of the Straw detector**

Author: Eliška Jelínková

Abstract: This thesis deals with the target experiment COMPASS, which is a part of CERN (European Organization for Nuclear Research). The physics program of the COMPASS experiment is focused on the research of the hadrons structure and hadrons spectroscopy. For this purpose, exclusive processes such as productions of mesons and deeply virtual Compton scattering are studied. These processes can be measured using an extensive spectrometer consisting of many detectors. One of them is the detector Straw composed of tube drift chambers. The calibration of its RT relation for the year 2021 was verified using the data from the 2018 run. Furthermore, a calculation from the 2021 survey measurement was performed. It serves to determine the position of the detector, which is essential for successful calibration and for high efficiency of the chamber in track reconstruction.

Key words: COMPASS, detector Straw, meson production, calibration of the RT relation, survey measurement

Contents

Introduction

One of the most important and challenging questions of physics is the structure of matter. It can be explored starting from the understanding of how the nucleons are built in terms of their quarks and gluons constituents. Many high energy physics experiments emerged for this purpose. An excellent facility to study the structure of the nucleons is the COMPASS (COmmon Muon and Proton Apparatus for Structure and Spectroscopy) experiment. This fixed target experiment is set up at the M2 beam line of the Super Proton Synchrotron at CERN (European Organization for Nuclear Research) in Geneva, Switzerland. It is located in North Area. The COMPASS experiment, also called NA58, is the main subject of this work. The first experiment proposal was accepted in 1998. One of the main goals for the nucleon structure was then to measure the gluon polarization and its contribution to nucleon spin. In the second phase, which started in 2012 and continues up to this day, the research field expanded. The aim is to study so-called Generalized Parton Distributions (GPDs) and thus discover the structure of nucleons. Today, about 200 physicists from 13 countries and 23 institutions work on the COMPASS experiment.

The thesis is divided into three chapters. The first one contains an overview of the COMPASS experimental setup. The wide physics program of the COMPASS experiment requires a very adaptable setup, which allows measurement with muon beams as well as hadron beams. It also allows to perform some unique measurements. In this chapter, the emphasis is put on the detector Straw. The detector Straw is a tracking detector composed of tube drift chambers. Each straw tube is filled with gas and it has an anode wire in the centre. The response of this detector is characterized by the RT relation, which is a dependence of a distance from the place of the primary ionization to the wire on the drift time.

The second chapter is dedicated to the description of the COMPASS experiment physics program and an introduction to the theoretical background. The COMPASS experiment aims to study in detail hadron structure and hadron spectroscopy. The current object of study is the parametrization of the GDPs which provide information about how quarks and gluons create hadrons. The GPDs can be accessed via measurement of exclusive processes such as Hard Exclusive Meson Production (HEMP) or Deeply Virtual Compton Scattering (DVCS). The focus of this thesis is, to be more specific, on the HEMP process.

Third chapter deals with Straw detector calibration. To provide as precise measurements as possible, it is convenient to validate the calibration of the detector Straw periodically. Before the 2021 run, currently scheduled to start taking physics data in August, preliminary calibrations are needed. To achieve an accurate track recon-

struction, it is necessary to ensure the correct position of the Straw detector. That is performed by the survey measurement, which is a starting point of the alignment procedure. It is also essential to calibrate the RT relation of the detector using a reconstruction C++ software package called CORAL (COmpass Reconstruction and AnaLysis) and PHAST software (PHysics Analysis Software Tool). The verification of the calibration of the Straw detector for run 2021 was done and the results are presented in the final chapter. For validation of the calibration were used the data from the 2018 run.

Chapter 1

The COMPASS experiment

The COMPASS (NA58) experiment[1] is a fixed target experiment set up at the M2 beam line of CERN SPS[2] accelerator. It is situated in North Area, shown in Fig. 1.1. The main physics program is the research of the nucleons and other hadrons structure and the spectroscopy of hadrons. For this purpose, the experiment uses the unique CERN M2 beam line, which can produce high intensity muon and hadron beams[3].

The aim of the COMPASS experiment requires a very adaptable setup, which allows measurement with muons as well as hadron beams. Specific demands are large angle and momentum acceptance.

The basic layout of COMPASS experiment as it was used for physics with hadron

[1] COmmon Muon and Proton Apparatus for Structure and Spectroscopy

[2] Super Proton Synchrotron

[3] The projects for the nucleon structure measurements with the muon beam and for the spectroscopy measurements with hadron beams were originally established separately in 1995. [1]

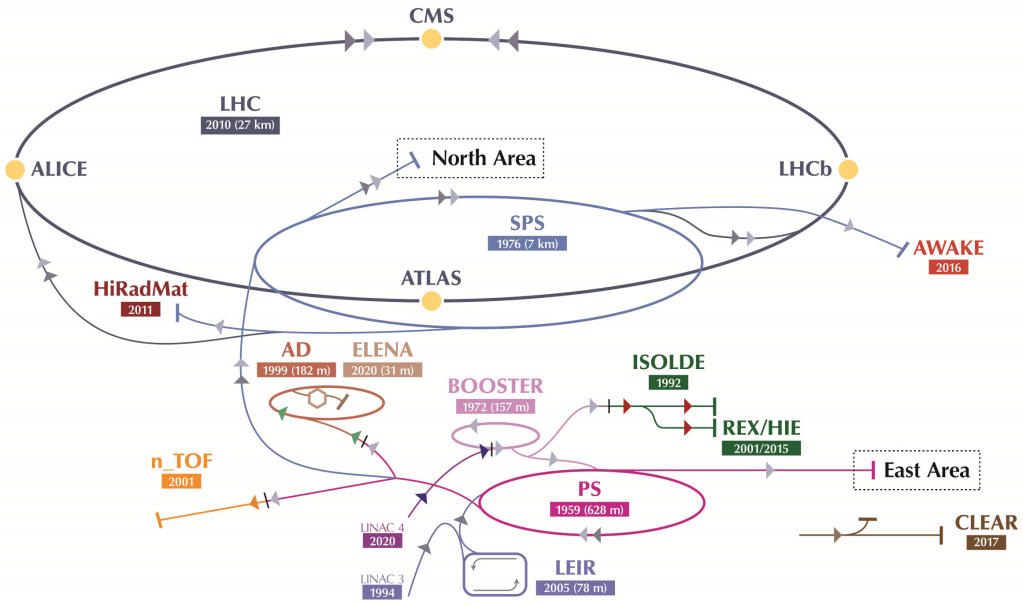

Figure 1.1: System of accelerators and experiments in CERN [2]

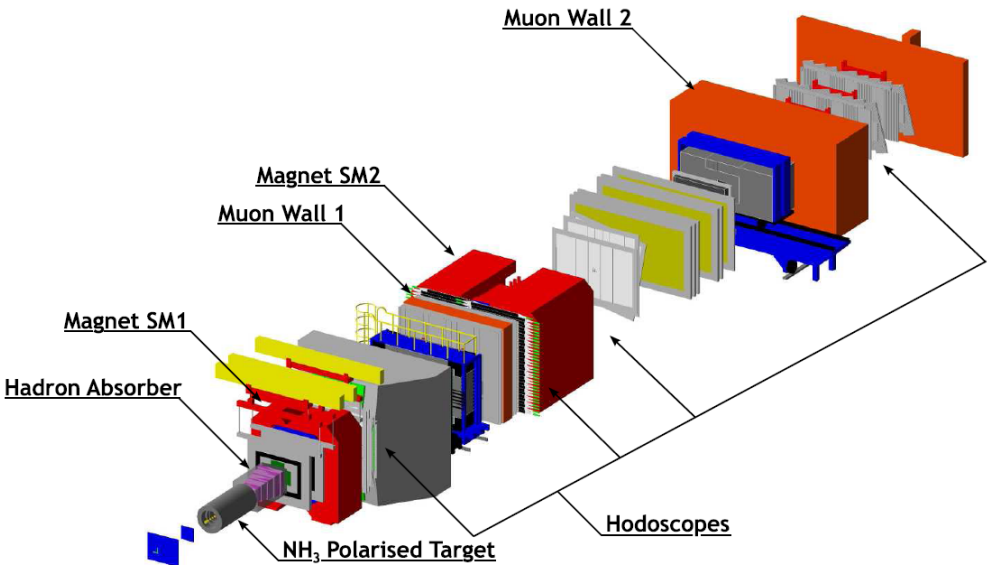

Figure 1.2: Three-dimensional view of COMPASS setup for measurements with hadron beams [3]

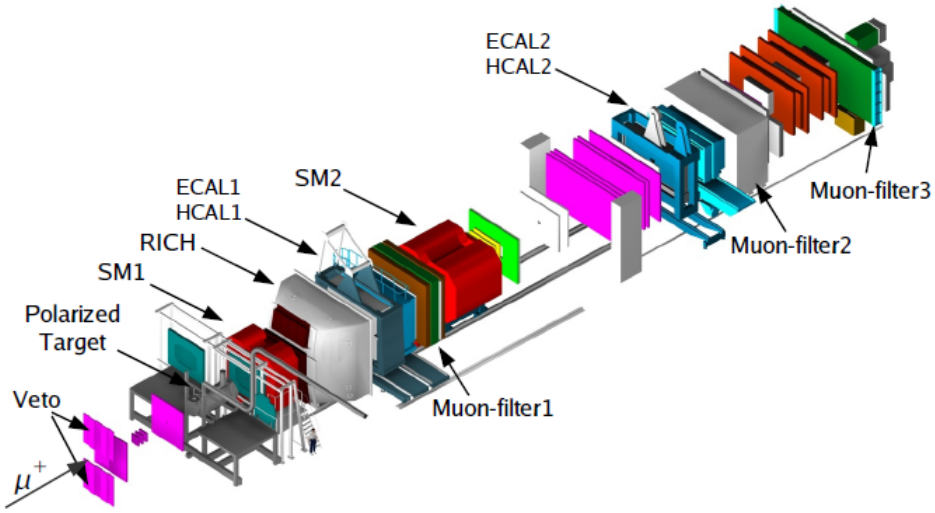

Figure 1.3: Three-dimensional view of COMPASS setup for measurement with muon beams [4]

beams is shown in Fig. 1.2, and for physics with muons in Fig 1.3 [1].

The experimental setup can be divided into four sections. The first part (the beam line section) constitutes the detectors upstream of the target, which can detect particles entering the target. The second sector is the target area, which is particular for each of the COMPASS physics programs. The third and the fourth parts of the layout are large angle spectrometer (LAS) and small angle spectrometer (SAS) and they are situated downstream of the target and take up the length of 50 m [5]. The variability required by the wide area of COMPASS experiment intent is guaranteed by the fact that huge setup elements are mounted on rails, which permits moving some of them at variable distances from the experimental target, putting detectors in the garage position (not to be used) and in the beam position (to be used) or exchange the detectors easily [1].

1.1 The Beam line

COMPASS receives beam from the M2 beam line of the SPS accelerator. M2 is 1.13 km long beam line. It is produced from T6 primary target [6].

The M2 beam line is able to produce high-intensity hadron (mainly proton or pion, positive or negative) beams up to 280 GeV/c or high-intensity positive muon beams up to 190 GeV/c and negative muon beams with lower intensity. Furthermore, the production of low-intensity electrons is also possible for testing and absolute calibration of electromagnetics calorimeters. Switching between the generation of these various beam models is fast and fully controlled. The changes take typically 30 minutes [5].

The T6 primary target consists of beryllium blocks with variable sizes adapting the particle flux to the experiment. Usually is used target with 500 mm thickness, although for lower flux can be selected thinner target. The proton flux on T6 is around $1.2 \cdot 10^{13}$ protons during 4.8 s long spills in a 16.8 s long SPS cycle[4].

Protons striking the beryllium target produce a muon beam. Interactions with the target generate secondary particles, mainly pions with a kaon contamination of about 3.6 %. Behind T6, there are collimators and absorbers, which select the momentum range of pions up to $\pm$ 10 % around a nominal momentum up to 225 GeV/c. In following 650 m long decay section are created muons by the weak decay of the secondary pions and kaons [7]. Dominant decay models for pions and kaons are [8]:

- $\pi^+ \rightarrow \mu^+ + \nu_\mu$ Branching ratio: (99.98770 $\pm$ 0.00004) %
- $\mathrm{K}^+ \rightarrow \mu^+ + \nu_\mu$ Branching ratio: (63.56 $\pm$ 0.011) %

However, the mean length of decay of pion is 9.5 km at energies of 10^2 GeV. That is the reason why the hadron absorber (made of nine motorised modules of berrylium, 1.1 m long each) has to be installed at the end of the decay section. Its function is to filter out the remaining hadronic states.

While pions and kaons decay, they are transferred through a section of focusing and defocusing (FODO) quadrupoles regularly distributed in 600 m. After that muons are cleaned and momentum selected by magnetic collimators. The resulting muons are transported to the surface level by a second FODO channel, which is 250 m long. Finally, muons are bent back onto a horizontal target and focused onto a polarized target. The scheme of the production and transfer of μ^+ from the SPS is shown in Fig. 1.4.

The CERN SPS M2 beam was originally created as a high-energy, high-intensity muon beam. However, the beam line was partially rebuilt to include high-intensity hadron beams and low-intensity electron beams for COMPASS experiment [5].
If high intensity secondary hadron beam is required, it could be created by moving nine motorised hadron absorber modules out of the beam and loading settings corresponding to a single momentum all along the beam line. The front part of

[4]The beams are delivered in bunches (also called spills). Typical length of the spill is 5–10 s and it is usually repeated after 15–60 s. Duration of the spill depends on the stability of magnets and the share of the beam. [7]

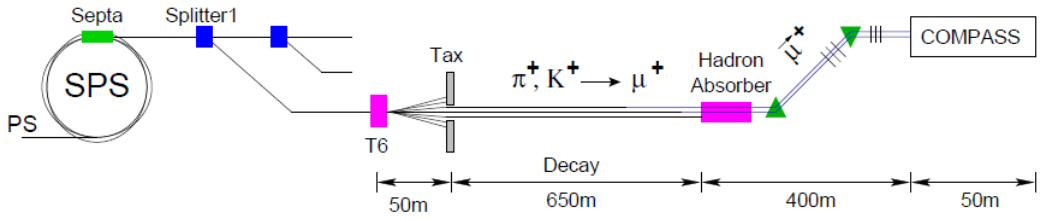

Figure 1.4: Schematic overview of the production and transfer of μ^+ from the SPS accelerator to the COMPASS experiment [9]

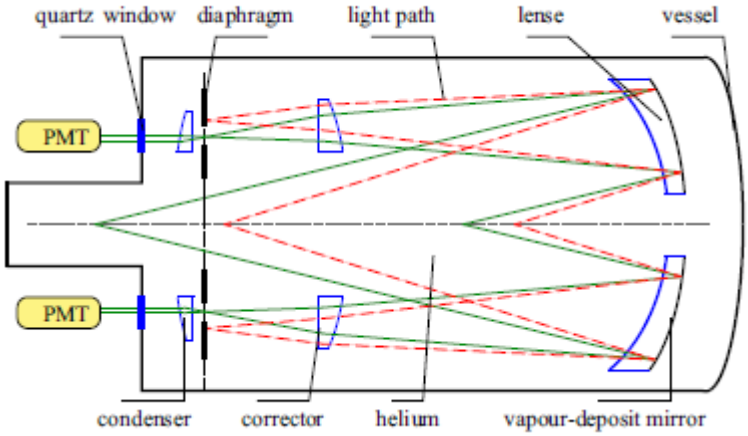

Figure 1.5: The basic principle of a CEDAR counter. Cherenkov photons are produced by two particles with different masses and with the same momentum (here dashed and full lines). Photons are radiated at different angles, resulting in rings with different radii. A ring shaped diaphragm, located in the focal plane perpendicular to the beam direction, selects the rings from the required particle type. The radius of the photon ring is matched to the radius of the diaphragm by regulating the pressure of the helium gas in the vessel. [5]

the beam line runs with the same optics as for the muon mode of the beam up to 225 GeV/c. At higher momenta is necessary to use different optics [1]. For beam particle identification two CEDARs[5] were added 30 m before the COMPASS target region. It is depicted in Fig. 1.5. The CEDAR detector was upgraded for run 2018. More details about the improvement can be found in [11].

Positive beams are mainly composed of protons for momenta larger than 150 GeV/c and negative beams have a predominant pion component. In both cases, it is possible that beams include electrons and kaons (at a level of a few percent depending on the energy). In the negative beam, the CEDAR counter is used for the distinguishing of the kaons from the pions [5].

The 40 GeV/c tertiary electron beam could be also provided from the negative secondary muon beam, which impinges on a 5 mm thick lead converter[6]. The converter is located about 50 m upstream of the hadron absorbers, which are moved out of the beam for this purpose [1]. A high-intensity negative hadron beam of 100 GeV/c containing electrons at the level of 10 % is directed to the electron target. Most of the electrons pass through the target, but they also lose energy by bremsstrahlung. The outcoming electrons have momentum spectrum same as a parent beam and

[5] CheErenkov Differential counter with Achromatic Ring focus [10]

[6] Also called the electron target [5].

very low intensity. The required electron momentum is picked out with the beam line magnets located downstream of the electron target [5].

1.2 Target

The COMPASS experiment is very flexible, therefore it could use various targets according to the actual physics program – various solid unpolarized targets, short and long liquid hydrogen targets equipped with the Recoil Proton Detector (RPD), and proton or deuteron polarized target [12]. The target region consists of the target itself, the silicon detectors, the Sandwich veto detector and the RPD. The target is surrounded by RPD time-of-flight detector CAMERA. Either liquid hydrogen or solid targets can be used during the measurements performed with hadron beams. However, most of the data with hadron beams was collected with hydrogen liquid target. Scheme of the target region is illustrated in Fig. 1.6 [1].

For 2016 and 2017 setup was also used liquid hydrogen (LH_2) target of 2.5 m length for studying GPDs[7]. In these years, positive and negative muon beams were used for measuring processes like DVCS[8] [14]. The polarity of the beam was changing periodically to ensure the same amount of data is collected for each beam.

The liquid hydrogen target can be easily replaced with a solid-target holder. Up to 16 different solid targets can be mounted on the holder (and used at the same time). Closer look to the liquid hydrogen target system with the target cell with cylindrical shape and a length of 400 mm and a diameter of 35 mm, a cryostat tube

[7] Generalized patron distributions [13]

[8] Deeply Virtual Compton Scattering [13]

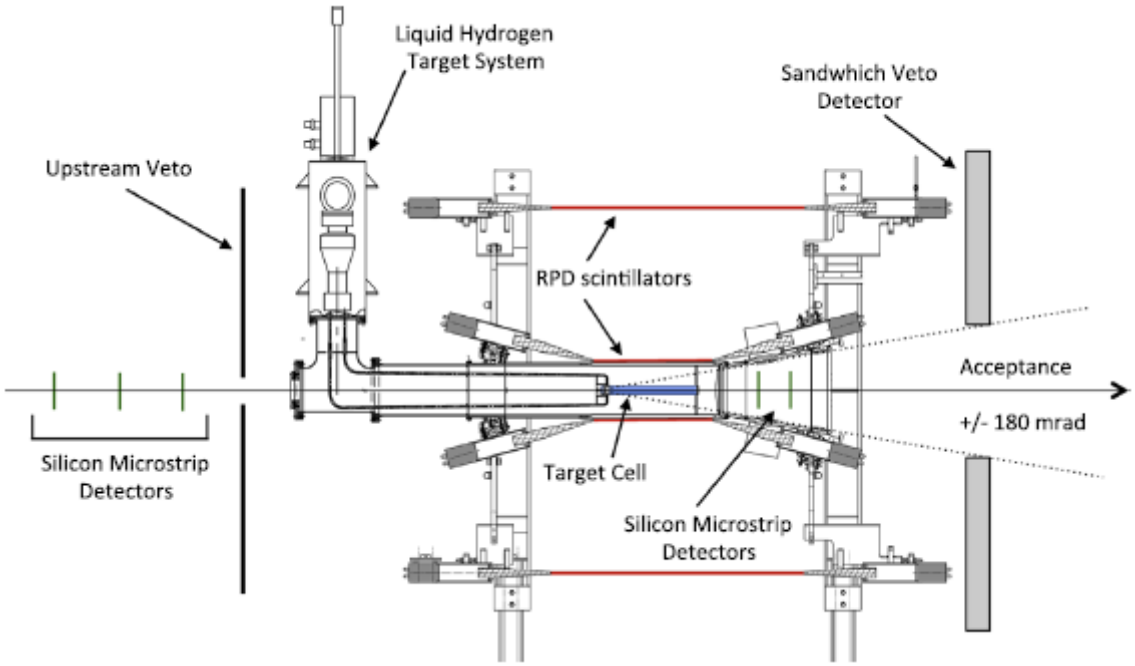

Figure 1.6: The side view of the target region with the liquid hydrogen target system [5]

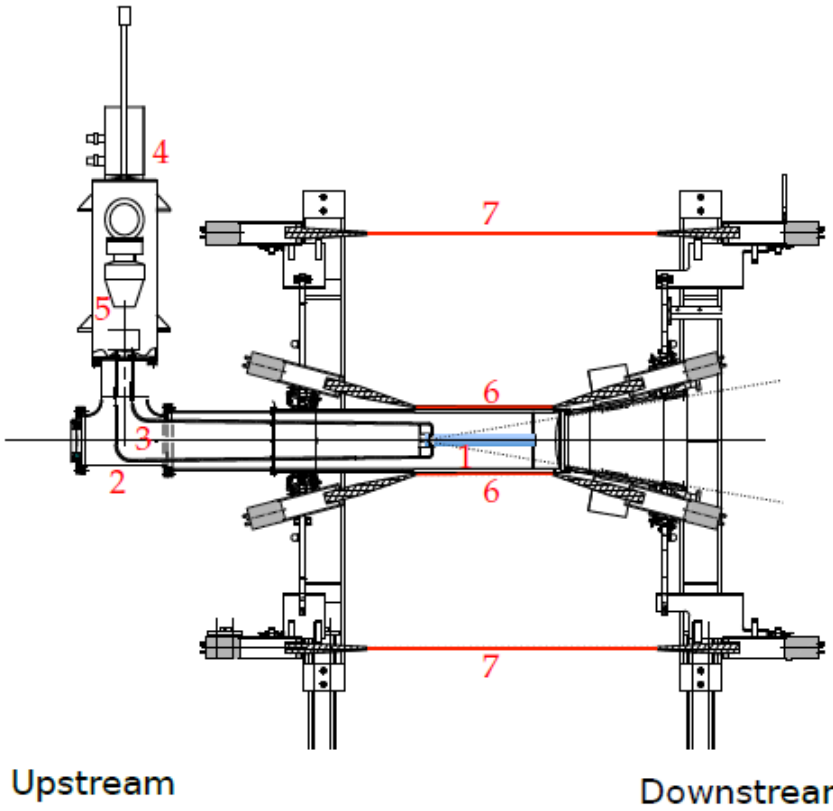

Figure 1.7: The side view of the liquid hydrogen target system. 1:target cell, 2: cryostat, 3: liquid hydrogen in/outlet, 4: LH_2 refrigerator, 5: vacuum system, 6: RPD ring A scintillator, 7: RPD ring B scintillator [7]

made from aluminium, and refrigerator, where is hydrogen gas liquified, is pictured in Fig. 1.7.

Upstream of the target, there are located three silicon detectors. These detectors work at the temperature of 200 K and together with a scintillating fibre counter determine the trajectory of the beam before it enters the target. Two other silicon detectors are situated immediately downstream of the target inside of the CAMERA detector.

The Sandwich veto is a scintillator/iron sampling detector used as a part of the trigger. It is located downstream of the CAMERA. The Sandwich veto detector veto events in which photons or charged particles reach the acceptance gap between CAMERA and Large Angle Spectrometer (LAS). Behind the Sandwich veto, there is a multiplicity counter (MC), which measures the number of charged particles in the final state.

The CAMERA detector measures the velocity and the energy loss of the recoil protons from the target emitted at large angles. This detector guarantees the exclusivity of the studied processes. The RPD detector CAMERA is also used in the trigger system [5]. For the proposed measurements with the 2.5 m long liquid hydrogen target a 4 m long CAMERA is required to fully cover the recoil-protons kinematics [13]. The CAMERA detector consists of two concentric layers of the scintillator (Ring A and Ring B). The inner ring of the CAMERA detector consists of 24 scintillators

around the target. All of the scintillators are connected with light guides to two photomultiplier tubes (PMT). The outer ring is set around the inner ring. It also consists of 24 PMTs [15].

1.3 Spectrometer

The COMPASS spectrometer [1] allows to reconstruct the tracks of all particles involved in a scattering event. In addition, kinematic reconstruction and particle identification is required. For this reason, many various detectors are distributed over the entire length of the spectrometer (50 m). The spectrometer is divided into two parts:

- Large Angle Spectrometer (LAS)
- Small Angle Spectrometer (SAS)

Large Angle Spectrometer

The LAS starts directly behind the target region. It has been designed to guarantee 180 mrad polar acceptance. It is placed around the SM1 (Spectrometer Magnet 1) dipole magnet, which is situated 4 m downstream of the target centre. Telescopes of trackers are located just before and after the SM1 magnet. The SM1 magnet is followed by a Ring Imaging Cherenkov (RICH) detector with large traverse dimensions to match the LAS acceptance requirements, which is used to identify charged hadrons up to 43 GeV/c momenta. An electromagnetic calorimeter (ECAL1) is also located in the LAS. It is followed by a large hadron calorimeter (HCAL1). The calorimeter detects outgoing hadrons. It is also used in the trigger formation. Muon filter completes the LAS.

Small Angle Spectrometer

The last part of the COMPASS setup is a the small angle spectrometer. The SAS detects particles at small angles ($\pm$ 30 mrad) and large momenta of 5 GeV/c and higher. A 4 m long SM2 (Spectrometer Magnet 2) is a central element of the SAS. The SM2 magnet is preceded and followed by telescopes of trackers. The downstream part of the SAS includes muon filter and hadron (HCAL2) and electromagnetic (ECAL2) calorimetres. ECAL2 is used for detection of neutral pions and photons. HCAL2 has the same function as HCAL1. A second muon filter is located at the downstream end of the spectrometer.

The COMPASS spectrometer setup as it was used in 2016 is pictured in Fig. 1.8. This section gives a basic description of the detectors used in the COMPASS spectrometer downstream of the target.

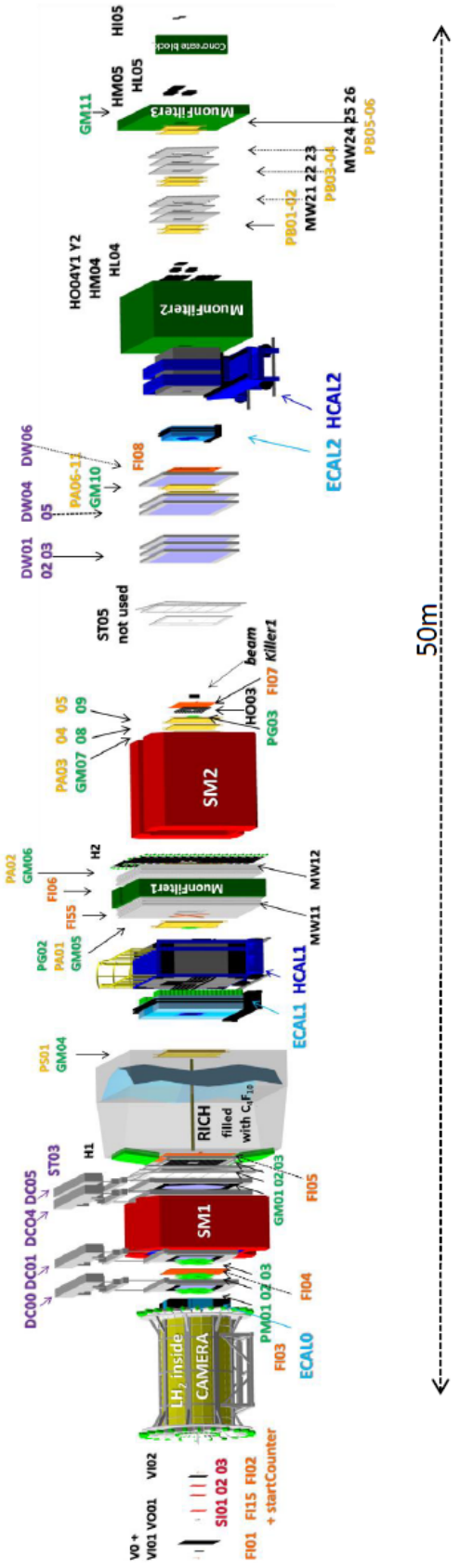

Figure 1.8: The COMPASS spectrometer setup for 2016 [16]

1.3.1 Spectrometer magnets

Two dipole magnets define the momentum of the final-state particles. Reconstructed tracks before and behind the magnets are compared to obtain the momentum of each particle within the acceptance of the spectrometer.
The COMPASS spectometer uses two magnets (SM1 in LAS and SM2 in SAS) [7]. The SM1 magnet is 110 cm long and it has a horizontal gap of 229 cm and a vertical gap of 152 cm in the middle. The main field component is in the vertical direction. An average integrated magnetic field of SM1 is 1.0 T/m. The SM2 magnet is the larger spectrometer magnet. The SM2 is a rectangular shape dipole magnet with a gap of 2 x 1 m and a total field integral of 4.4 T/m for its nominal current of 4000 A [1]. Because it has a higher bending power than SM1, the SM2 allows a more accurate determination of the momentum of high momentum tracks [15].

1.3.2 Calorimeters

Electrons and hadrons can be separated by calorimeters. Both stages of COMPASS spectrometer include electromagnetic and hadron calorimeters. Two hadron calorimeters (HCALs) and three electromagnetic calorimeters (ECALs) were used in COMPASS setup in 2016/2017 [16].

- The HCALs are located behind the ECALs and before muon filters. Both hadron calorimeters serve a double purpose in the experiment. They participate in triggering on inelastic muon scattering events and they also measure the energy of hadrons produced in the target. The hadron calorimeters are designed to stop hadrons with a dense matter (lead or iron). The HCALs are sampling calorimeters. The hadron calorimeter 1 (HCAL1) has a modular structure. Each module consists of layers of iron and scintillator plates. The HCAL1 has the outside dimensions of 4.2 x 3 m and a central rectangular window of 8 x 4 modules. The hadron calorimeter 2 (HCAL2) also consists of modules. Two types of modules are used in this calorimeter. The HCAL2 has a hole with a dimension of 2 x 2 modules to pass the high intensity beam.

- Electromagnetic calorimeters ECAL1 and ECAL2 are situated (as was already mentioned) in the LAS and the SAS. In addition to that, for 2016/2017 setup the ECAL0 has been installed directly behind the CAMERA recoil proton detector. ECALs are homogenous calorimeters consisting of lead glass cells of different types such as GAMS, OLGA and Shaslik. The ECAL1 and ECAL2 are shown in Fig. 1.9. Inside the lead glass, photons and electrons generate electromagnetic showers. Electrons and positrons from showers emit Cherenkov light [1].

  Large-angle electromagnetic calorimeter ECAL0 uses Shaslik elements having lead/scintillator stack and Multipixel Avalanche PhotoDiode (MAPD) as photodetectors [13]. With the help of electron beams are the ECALs recalibrated after important changes of the detectors and at beginning of each year of data taking [14].

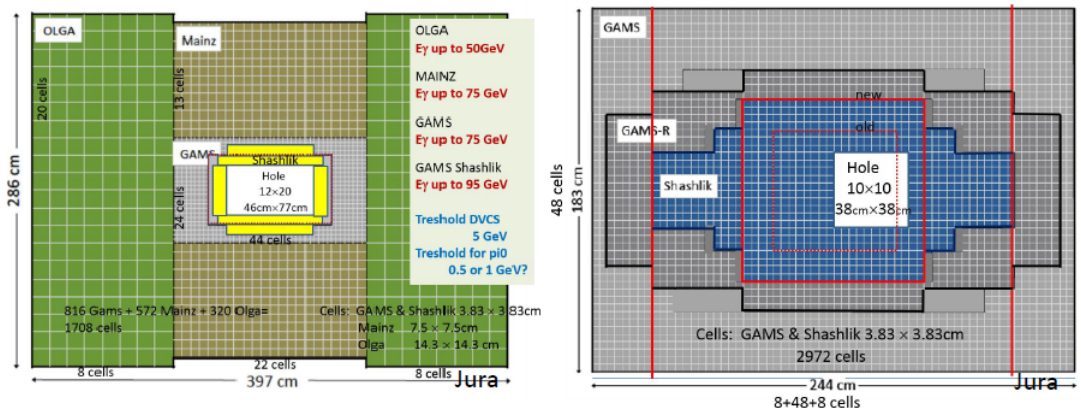

Figure 1.9: The electromagnetic calorimetres - left: ECAL1, right: ECAL2 [16]

1.3.3 RICH

Ring imagining Cherenkov [17] is one of the key detectors of the COMPASS experiment. The RICH detector separates outgoing hadrons into pions, kaons and protons. It is located in the LAS. The detector volume is filled with a radiator gas C_4F_{10}. If a particle passes through the detector with a velocity greater than the phase velocity of light in the medium, Cherenkov light is emitted under the characteristic angle. This angle is measured and the velocity of the particle can be determined. If the momentum of the particle is known, the corresponding mass can be calculated and thus particle type can be identified [18].

1.3.4 Trigger system

The COMPASS experiment records the data event by event. Therefore, a trigger system is needed. The trigger system selects interesting event candidates and activates the data recording. The trigger system is based on fast hodoscope signals, energy deposits in calorimeters and a veto system. Which elements are used to form the trigger signal depends on the incident beam (muons or hadrons) [1].

Muon trigger

Muons are detected behind thick concrete or iron absorbers for muon identification. There are two approaches how to trigger either by measuring muon's scattering angle in a plane perpendicular to the dipole bending plane[9] or by measuring the energy loss using the deflection in the dipole fields[10].

In order to guarantee triggering only on muons, at least one of the two hodoscopes is located behind an absorber (muon filter). The muon trigger hodoscopes are divided into four subsystems. Each of them covers a different kinematic region.

[9] Target pointing trigger [13]

[10] Energy loss trigger [13]

- The Ladder trigger (HL04, HL05 in Fig.1.8) selects muons with small scattering angles and high energy losses. Both hodoscopes consist of short vertical strips read out on both sides by photomultiplier tubes.

- The Middle trigger (HM04, HM05 in Fig. 1.8) combines the features of an energy loss trigger with a target pointing trigger.

- The Outer trigger consists of a horizontal hodoscope plane at the exit of the second spectrometer magnet (HO03 in Fig. 1.8) and a second one behind the hadron absorber in the SAS (HO04 in Fig. 1.8) to obtain vertical target pointing. HO04 is divided into two halves (Y1 Y2 in Fig. 1.8) to avoid very long strips.

- The LAS trigger (H1, H2 in Fig. 1.8) comprises two horizontal hodoscope planes. H1 is located in front of the RICH and H2 is situated behind the first hadron absorber and the MW1.

In addition to the hodoscope trigger system, the COMPASS experiment use veto system and calorimetric trigger [13]. A fraction of the beam muons is not focused on the beam axis. A large amount of these halo muons can be detected and cause false trigger signals when reaching the hodoscopes [4]. The main purpose of veto system is to remove these false signals. It consists of hodoscopes upstream of the target, leaving the central region around the beam uncovered. A large fraction of the unwanted trigger signals can be eliminated by demanding the absence of a signal in the veto system together with a coincidence in two hodoscope planes [19].

1.3.5 Tracking detectors

The tracking system of COMPASS includes many tracking stations distributed over the entire length of the spectrometer. Each tracking station consists of a set of detectors of the same type. A charged trajectory is measured in several transverse projections to the beam direction to reduce ambiguities [1]. Near the beam, the detector requirements are stricter. Capability to stand high flux, good timing and spatial resolutions are key demands. For detectors more distant from the beam are requirements less demanding [15]. The tracking detectors can be divided into three groups.

Very Small Area Trackers

Very Small Area Trackers (VSAT) cover the beam region up to a radial distance of 2.5–3 cm. Scintillating fibres (SciFi) and silicon microstrip detectors are needed because the very high rate of the beam particles in this area requires excellent time or position resolution of the corresponding detectors in order to identify hits belonging to the same track. The SciFi detectors provide tracking of incoming and scattered beam particles as well as of all other charged reaction products in and very near the centre of the primary beam. They consist of several staggered layers of scintillating fibres, allowing large overlap and good detection efficiency. The silicon

microstrip detectors are used for the detection of the incoming muon beam track. For the hadron program, they are used for vertex and track reconstruction downstream of the target. These detectors have an active area of 5 x 7 cm.

Small Area Trackers

Small Area Trackers (SAT) cover the intermediate region at a radial distance of 2.5 cm to about 20 cm. This region contains detectors characterized by high spatial resolution and low material budget, with an inactive zone in the beam area. Two types of micro-pattern gaseous detectors are used: Micromegas (Micromesh Gaseous Structure) detectors and GEM detectors. The Micromegas detector is based on a parallel plate electrode structure and a set of parallel microstrips for readout. A metallic micromesh separates the gaseous volume into two regions. In the conversion gap, ionisation takes place. The amplification gap with a higher electric field produces avalanches, which are then collected on the microstrips. The working principle is pictured in Fig. 1.10. The active area of the detector is 40 x 40 cm and the central dead zone is 5 cm in diameter. The GEM (Gas Electron Multiplier) detectors consist of three GEM amplification stages, stacked on top of each other and separated by thin spacer grids. Similar to the Micromegas detectors, the GEM detector focuses on the measurements of electrons created in an avalanche shower inside the fiducial volume of the detector. The COMPASS GEM detector volume is divided into several subvolumes by a thin foil with a large number of micro-holes. This thin polyamide foil has a copper cladding on both sides. Upon application of a potential difference of several 100 V across the foil, avalanche multiplication of primary electrons drifting into the holes is obtained and electron signal is then read out. Fig. 1.10 depicts the electric field lines near the GEM hole for typical voltage settings. The active area of each GEM detector is 31 x 31 cm. The central region with a diameter of 6 cm is deactivated during normal high-intensity physics runs.

Large Area Trackers

Large Area Trackers (LAT) cover the large areas defined by the experimental setup acceptance. The LAT have a good spatial resolution. Drift chambers (DC)

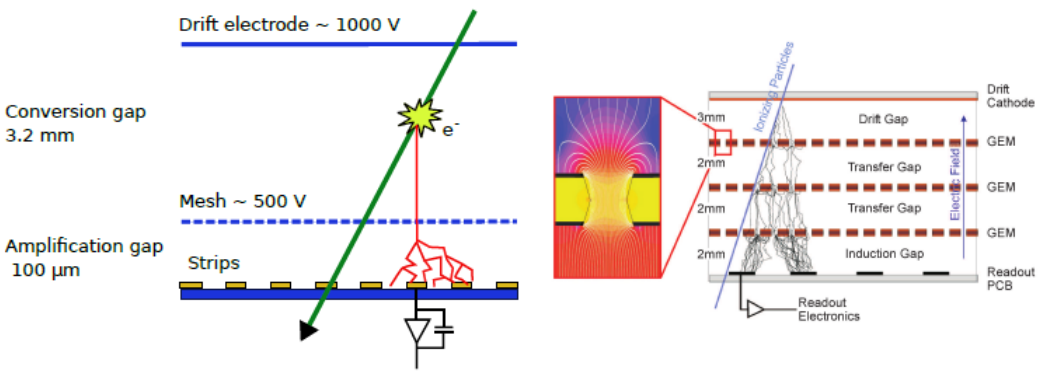

Figure 1.10: Left: Principle of the Micromegas detector, right: Schematic cross-section of a triple GEM detector [1]

track particles emerging at large angles. The DC have an active area of 1.8 x 1.3 m with a central dead zone of 30 cm diameter. The drift chambers measure charged particles. The detector consists of a drift cell filled with gas, cathode planes, anode wires and potential wires. The potential wires are used to achieve a homogenous electric field inside the detector volume. The gaseous volume comprised between two cathodes is ionized by fast charged particles. Created electrons are accelerated and multiplied in avalanche through the acceleration in the electric field. This electron cloud is read out by the anode wire. In fact, the drift time of the avalanche to the anode wire is measured to improve the spatial resolution. The LAT also comprise straw drift tubes (more details about detector Straw can be found in section 1.4). From downstream of the RICH counter to the far end of the setup the particles scattered at small angles are detected by multiwire proportional chamber (MWPC) stations with active areas of 1.8 x 0.9–1.2 m. The diameters of their central dead zones increase along the beam line from 16 cm to 22 cm. The outer region downstream of the SM2 is covered by straw stations and large area DC with active areas of 5.0 x 2.5 m and 50 cm or 100 cm diameter insensitive central zone [1].

1.4 Detector Straw

The 15 double layers of large area straw drift chambers are used for tracking and momentum determination of charged particles produced at large scattering angles (15–200 mrad). The chambers are grouped together in modules[11]. Each of them measures one space point and consists of double layers with vertical (type X), horizontal (type Y) and inclined[12] (type U and V) straw tubes. Schematic view of a chamber (type X) is shown in Fig. 1.11 [20]. The main purpose of the inclined straws is the separation of real tracks from ghost ones. When two vertical and two horizontal neighbouring wires get a hit, it is not known which tracks are real and which are ghost. These possible candidates are shown in Fig. 1.12. Thus, additional information on the drift times of the inclined wires is needed [21].

Each chamber consists of two layers of thin-film straws oriented in the same direction, which are mounted into an aluminium frame [20]. The second layer is shifted by half a diameter with respect to the first one. This arrangement is used for specifying a position determination. When a particle traverses a single straw, it can not be distinguished whether it passes through the left or the right side of the wire since the only information kept is the drift time to the wire. The drift time in the straw will be the same for all positions on a circle inside the straw. In the second layer, two straws cover the straw in the first layer. One covers the right side of the straw and the second the left side. With information about which straw in the second layer the particle hits it is possible to separate the cases where the particle

[11] Initially, there were three modules - ST02 (with 6 double layers), ST03 (with 6 double layers), ST05 (with 3 double layers). Before 2015 run, the ST02 module was replaced with a more modern drift chamber detector - DC05. The ST05 module was discarded before 2016 run due to its unreliability. Thus in the 2016/2017 setup was used only one Straw module - ST03 (as can be seen in Fig. 1.8). The ST03 was located in the LAS. [16]

[12] The inclined tubes are rotated by 10° with respect to the vertical ones. [20]

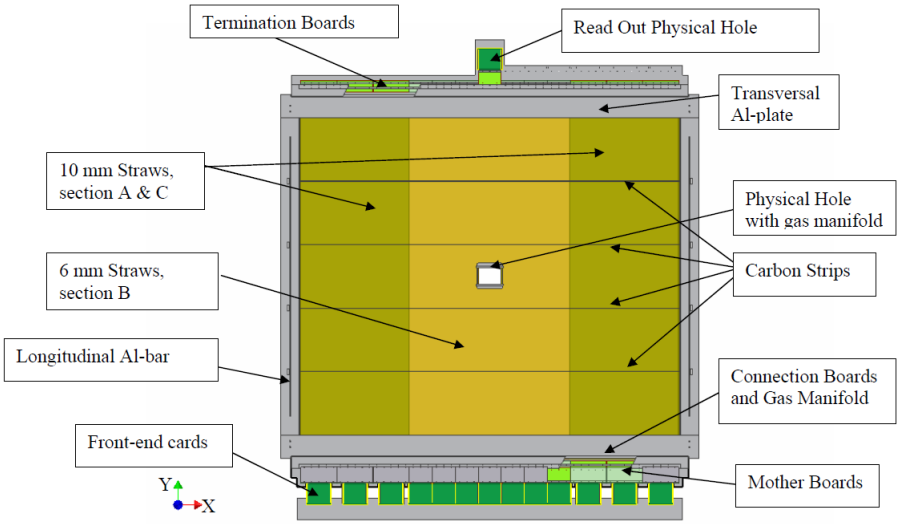

Figure 1.11: Schematic view of a chamber (type X) [20]

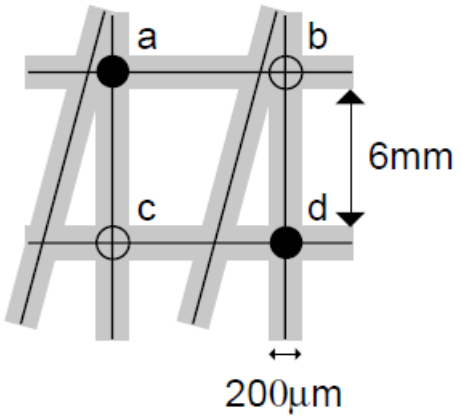

Figure 1.12: The real hits a, d and the ghost hits b, c. The black lines represent the measured coordinates and the grey areas correspond to the resolution of the straws [21]

passes through the left side or the right side of the wire of the straw in the first layer [21].

The straws in one layer are glued together to one plane, which is divided into three sections. Because the central part (section B in Fig. 1.11) is closer to the beam axis, it is exposed to higher rates. Therefore, it comprises 222 straws with 6.144 mm outer diameter while the two outer parts (sections A and C in Fig. 1.11) have 96 straws with 9.654 mm outer diameter[13]. The central part of the detector, called the physical hole, has a rectangular hole of about 20 x 10 cm for the beam. The design has been optimised with respect to rate capability, spatial resolution, low material budget and compactness of the detector.

[13]The detailed dimensions refer to the type X chambers with vertical wires. [20]

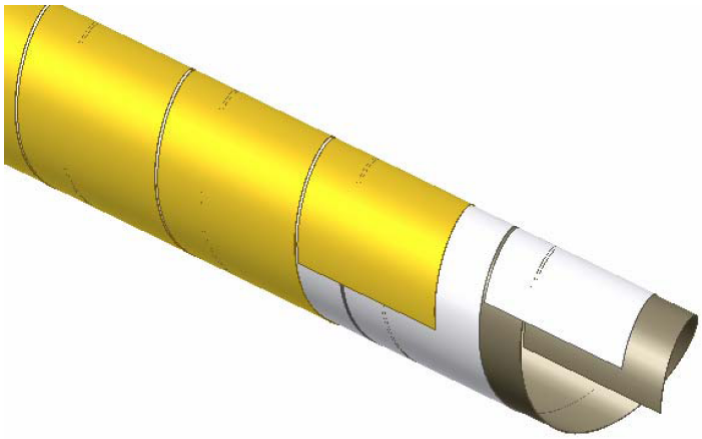

Figure 1.13: The straw tube consisting of an inner layer of Kapton XC (40 μm), glue film (7 μm) and an outer layer of aluminized Kapton (12 μm) [20]

The straw tubes

The structure of the straw tube is illustrated in Fig. 1.13. The straw tubes are made of two layers of thin plastic films. The inner layer consists of carbon loaded Kapton 160 XC 370 foil with a thickness of 40 μm $\pm$ 10%. This layer is glued onto a Kapton foil of a thickness of 12 μm and aluminized on one side. The advantage of the plastic foils is a low density and good mechanical stability at low thickness. In addition, Kapton XC is an intrinsically conductive material, which makes the straws more stable against discharges and sparking.

The anode gold-plated tungsten wires of the drift tubes with a 30 μm diameter are centred in the straws by two end-pugs and four small plastic pieces so-called spacers. The spacers are positioned at intervals of about 60 cm along each tube. Tubes are filled with a fast counting gas ($Ar/CO_2/CF_4$, 80/10/10[14]). The length of COMPASS straw tube increases with increasing humidity, because the plastic foils used for the straw tubes are hydroscopic[15].

Due to the high resistance of the cathodes of the straw tubes, cathodes are transparent for electromagnetic fields to a certain extent. This has impacts on the signal attenuation, on cross talk effects between adjacent straw tubes and on electromagnetic interferences from external noise sources. Therefore, the electrical properties of the straw tubes were analyzed during the detector design stage. The aging properties of straws were also studied. Besides problematical radiation induced deposits on the anode wires, it was suspected, that carbon clusters, providing the conductivity of Kapton XC, might get electrically disconnected from each other by irradiation. This could lead to local inefficiencies of the detector, an increased dark current or even sparking.

For the large area chambers is required the high absolute precision and minimiz-

[14]Initially, it was used $Ar/CO_2/CF_4$, 74/6/20. However, the CF_4 gas is very expensive and also environmentally dangerous as greenhouse gas. It was shown that the amount of CF_4 can be decreased by half, while maintain almost the same efficiency of the detector. [22]

[15]For maintaining constant humidity each straw station is surrounded by a protective gas volume of N_2 gas surrounded by 12 μm thin Mylar aluminised foils. [1]

ation of the amount of the material in the active section of the detector at the same time. Used materials require many properties. It is necessary to understand them in detail. The straw tubes have to be sufficiently gas tight, the plastic materials have to be adhesive to commercially available glues and for both the Al-frame and the Kapton straw tubes is important to have relatively large temperature expansion coefficients.

The straw chambers

As was already mentioned the active part of each chamber consists of two layers of straws of a length of 3202 mm. They are glued together to a plane with higher mechanical stability compared to individual straws. This improves the mechanical precision and ruggedness, which can be achieved. The load onto the frame, which ensures that the individual straws will be kept straight by tension, can be significantly reduced. The ends of the straws of a double layer are glued gas tight between two transversal aluminium plates on each side of the frame. This arrangement can be seen in Fig. 1.14. Carbon fibre strips are parallel to the transversal Al-frame elements. They are glued to the planes every 60 cm and they are fixed to longitudinal Al-bars of the frame. The aim of carbon fibre strips is to support the straw layers. The counting gas streams through a gas manifold and through the end-plugs into the straws from the bottom side of the chambers and exits through the manifold on the top. The manifold also ensures a proper gas flow through the physical hole. This material-free hole is created by cutting 32 straws in the centre of section B[20].

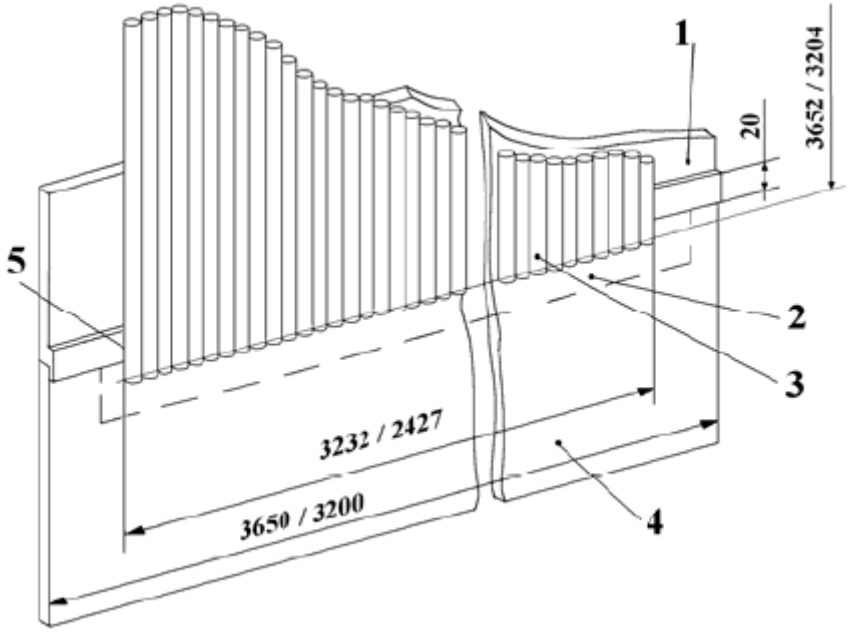

Figure 1.14: The two straw-planes are sandwiched and glued gas tight between two transversal Al-plates. Only one plane and one transversal plate are shown. 1 – transversal Al plate, made with an accuracy of better than 0.1 mm, 2 – boundary dimensions of the chamber gas volume, 3 – straw-plane, 4 – Al element used to mount peripheral elements (mother boards, readout cards) of the chamber, 5 – area where the straw-plane is gas tightly sealed into the Al frame [20]

Chapter 2

Physics program

2.1 Introduction

The aim of the COMPASS experiment is to study in detail how nucleons and other hadrons are made up from quarks and gluons. The research fields of hadron structure and hadron spectroscopy are closely connected since their very beginnings[13]. The first indications of a possible nucleon structure appeared in the 1950s when experiments with electron beams of several hundred MeVs were performed in the SLAC laboratory[16]. The electrons were elastically scattered on hydrogen or on heavier targets[17] [24]. The results confirmed the already known fact that nuclei are composed of protons and neutrons [25].

In 1964, Murray Gell-Mann and George Zweig independently postulated that hadrons are formed by combinations of elementary constituents. Moreover, for some reason, these fundamental objects are not observed as free particles. Gell-Mann named these hypothetical constituents quarks[18]. In Gell-Mann's model, baryons are made up of three quarks and mesons consist of quark and antiquark. Each quark carries a spin of $1/2$ and has a property called a color charge. The Gell-Mann's model was first experimentally demonstrated in the SLAC laboratory in 1968 by series of electron-proton scattering [26].

The basic principles of elastic and inelastic scattering are described in the following two sections.

[16] SLAC laboratory is a research centre in the United States of America. The original name was Stanford Linear Accelerator Center. Today it is the SLAC National Accelerator Laboratory. [23]

[17] The study of the structure of hadrons is carried out in a manner similar to the method used by Rutherford at the beginning of the last century to scatter particles α on atoms. The number of cases when the scattering angle of particle α was large was surprisingly high. Such interactions could be explained theoretically, assuming the fact that the positive charge in the atom is concentrated within a small volume. [25]

[18] According to James Joyce's book $Finnegans\ Wake$, which contains the phrase "Three quarks for Muster Mark". [26]

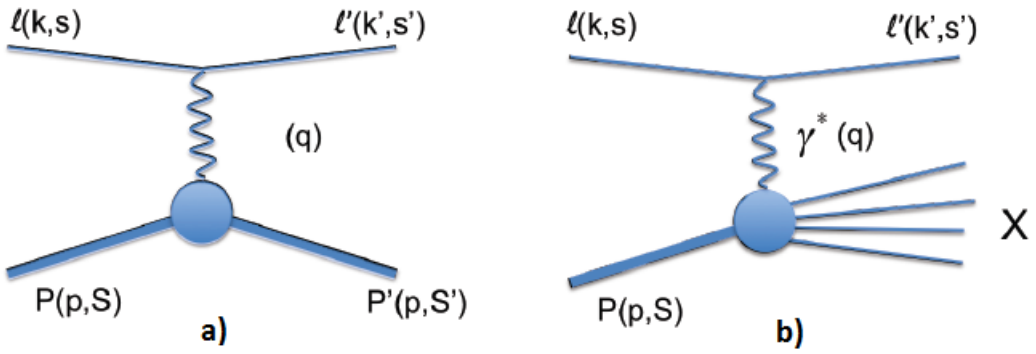

Figure 2.1: a) The elastic scattering, b) the inelastic scattering of a lepton off a proton [28]

Elastic scattering The elastic scattering of a lepton off a proton is illustrated in Fig. 2.1. The lepton has a four-momentum k and a spin s and the proton has a four-momentum p and spin S. In the final state, the momentum and spin of the particles are denoted with a prime (‘) as can be seen in Fig. 2.1. The four-momentum of an exchanged virtual photon is q. For a given lepton energy, the kinematics of elastic scattering is described with only one variable – the virtuality of the photon:

$$Q^2 = -q^2 = -(k - k‘)^2 \tag{2.1}$$

The square of any four-momentum is invariant, which means it remains unchanged under some transformations [27] [28].

Inelastic scattering To study small structures inside a proton, it is necessary to increase the energy of the leptons and thus increase the energy of the virtual photon. At higher values of Q^2, the significance of elastic scattering decreases and inelastic scattering is much more common. However, such scattering usually breaks the proton and creates other hadrons (represented with X):

$$l + p \rightarrow l' + X \tag{2.2}$$

The scheme of the inelastic scattering is pictured in Fig. 2.1. Moreover, another invariant dimensionless quantity x_B can be defined.

$$x_B = \frac{Q^2}{2pq} \tag{2.3}$$

This so-called Bjorken scaling variable can be in the infinite momentum frame[19] interpreted as the not measurable mean value of fraction x of the nucleon's four-momentum, which is carried by the struck quark before the virtual photon is absorbed [30]. It takes values from zero to one. For elastic scattering, x=1, while for inelastic scattering, $x < 1$ [23] [31]. When x is small and Q^2 reaches large values, so-called Deep Inelastic Scattering (DIS) occurs. In the DIS, the momentum fraction

[19] It is convenient to consider the infinite momentum frame. In such a frame, the nucleon has a very large momentum and the momentum of the parton is almost collinear with the longitudinal momentum of the nucleon. [29]

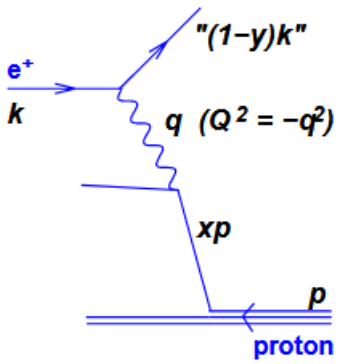

Figure 2.2: Interaction of electron and proton with assigned kinematic quantities [31]

x carried by struck parton is always identified with Bjorken variable x_B. However, in the hard exclusive Deeply Virtual Compton Scattering (DVCS), x could be equal to different values [14].

The momentum fraction lost by electron in proton rest frame is represented by variable y, which also belongs to the interval $0 \leq \mathrm{y} \leq 1$ [25].

$$y = \frac{qp}{pk} \tag{2.4}$$

These basic kinematic quantities are shown in Fig. 2.2.

The significance of the height of the photon virtuality Q^2 in the investigation of the structure of the proton using virtual photons can also be viewed from the point of view of wave-particle duality. A photon is a quantum of electromagnetic waves and for examining objects by their interaction with waves, in general, the amount of achievable details is proportional to the wavelength of the waves used [23]. At small values of Q^2 a coherent scattering with the whole nucleon realizes, at higher values interactions with partons are happening. The growth of Q^2 is equivalent to the reduction of the wavelength of the photon[20] and with sufficiently large Q^2 the photon "sees" individual components rather than the entire proton [25]. Therefore, better ability to investigate small structures inside a proton is achieved at higher values of Q^2 as can be seen in Fig. 2.3 [23].

The first experiments performed in the SLAC laboratory with the electron beam reached relatively small values of $Q^2 \simeq 10$ GeV^2. The cases with the highest values of the transmitted momentum $Q^2 \simeq 10000$ GeV^2 were detected in H1 and ZEUS experiments located on the HERA electron/positron-proton beam accelerator in the DESY laboratory[21][25].

[20] A virtual photon can be understood as a particle of mass Q^2. The wavelength of $\sim 1/Q^2$ can be assigned to it. [25]

[21] The HERA (Hadron Electron Ring Accelerator) located in laboratory DESY (German Electron Synchrotron) in Hamburg, Germany, was unique for its time. It was able to accelerate the beams of two different types of particles and realize their frontal collision. For the HERA construction were for the first time used superconducting magnets. [23]

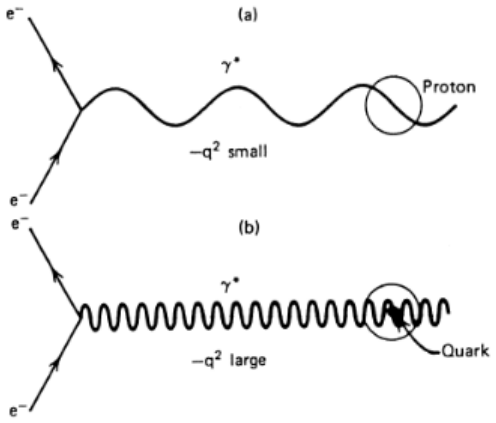

Figure 2.3: Schematic drawing of the relationship between Q^2 and the wavelength of the photon [32]

In 1969, when interpreting data from the first direct studies of the structure of the proton, partons were hypothesised as its internal constituents. They were later identified with quarks and gluons [13]. The physical interpretation of the experimental data was first proposed by Feynman. It was based on the hypothesis that the high energy deep inelastic scattering of electrons off protons can be expressed as the sum of the cross-sections of elastic electron scattering off partons, each carrying only part of the proton momentum [33]. The fact that the partons have spin 1/2 was one of the reasons why they were initially identified with quarks that had already been successfully used to elucidate the statistical properties of hadrons. The quantum numbers of a proton can be explained by the fact that it consists of two up quarks u and one down quark d[22], which are called valence quarks. If the proton also contains any number of virtual quark-antiquark pairs $q\bar{q}$, it has the same quantum numbers because their additive quantum numbers are zero. Experimental results from deep inelastic scattering prefer the hypothesis of such pairs named sea quarks. The sea quarks are generated by gluons. The gluons, massless particles with spin 1, serve as mediators. They are exchanged between two quarks in the strong interaction. They do not have an electric or a weak charge, but they carry a color charge that keeps the quarks inside the nucleons[23] [25].

Development of the idea of proton structure from the original model of valence quarks to the parton model, in which the proton is formed by valence quarks, sea quarks and gluons, is shown in Fig. 2.4.

Strong interactions between partons are described in the theory of strong interactions, i.e. quantum chromodynamics (QCD). As already mentioned, a color charge[24] is attributed to quarks and gluons. There are three types of the color charge: red, blue and green. The strong bond between the particles asymptotically weakens with increasing energy and decreasing distance, hence the hadrons are indivisible. This

[22] A neutron is composed of two down quarks and one up quark. [14]

[23] Gluons can be only detected within hadrons or in colorless combinations with other gluons so-called glueballs. [34]

[24] The color charge in strong interactions has an analogous meaning as the electric charge in electromagnetic interactions. [25]

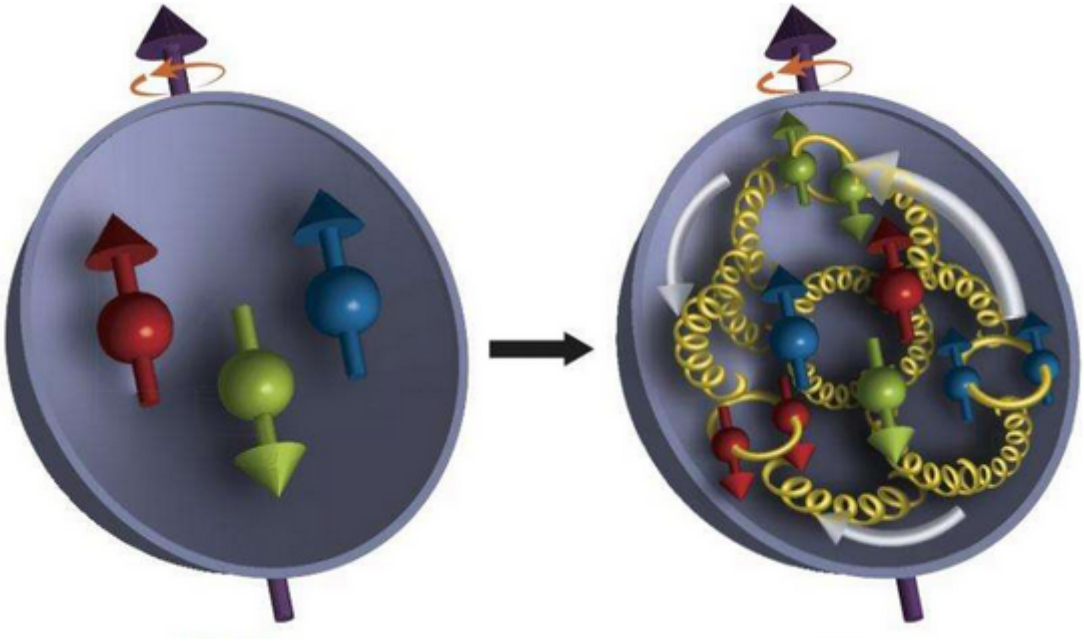

Figure 2.4: Model of the structure of proton. Left: naive picture of proton with three valence quarks, right: realistic picture of proton with partons (three valence quarks, indefinite number of sea quarks and gluons). Arrows are representing spins of the particles. [35]

phenomenon is called quark confinement. If the quarks approach each other and Q^2 is large, the quarks achieve so-called asymptotic freedom and they can be considered as quasi-free[25][25].

Due to the quark confinement, Parton Distribution Functions (PDFs) are used for describing the structure of the nucleon as a function of the nucleon momentum fraction carried by a parton of a certain species. The PDFs are probability weighting functions and they describe structure via parametrization. Probability amplitude is a function describing the probability that a parton with a given x is found on a certain scale Q^2. The concept of parton distributions distinguishes unpolarized, polarized and other PDFs. The PDFs cannot be calculated using a QCD perturbation theory. That is the reason why they are obtained by fitting variables to experimental data. The PDFs are studied primarily in DIS. They are investigated independently from nucleon electromagnetic form factors [13]. The nucleon electromagnetic form factors are related to the charge and magnetization distribution inside the nucleon. They are studied in elastic scattering [36].

In 1987, the measurements in European Muon Collaboration (EMC)[26] with polarized protons showed that, at higher four-momentum transfer, the spin of the proton was not concentrated in its valence quarks in contrast to the situation for static

[25]This state of matter is called quark-gluon plasma. It is assumed that it was also present in the early stages of the universe's evolution. [26]

[26]The European Muon Collaboration was formed in the years 1972–1974. It aimed to study the quark structure of the nucleon through deep inelastic muon scattering. The EMC was one of the first large experimental particle physics collaborations. After the EMC experiment finished taking data in 1985 new collaborations were formed – first the New Muon Collaboration and then the Spin Muon Collaboration. Finally, the apparatus and infrastructure were taken over by the COMPASS experiment. [37]

protons. The fact that the contribution of the valence quarks to the nucleon spin is much smaller than expected was named proton crisis or proton puzzle [28] [37]. Therefore, Generalized Parton Distributions (GPDs) have been developed in the last few years as a tool to study hadron structure in new ways. The GPDs embodies both form factors and PDFs. They contain a wealth of information about how quark and gluons make up hadrons [38]. The GPDs can be considered as momentum-dissected form factors which provide information on the transverse localisation of a parton as a function of the fraction it carries of the nucleons' longitudinal momentum. This allows to obtain a "three-dimensional picture" of the nucleon. It is sometimes referred to as "nucleon tomography". A complementary approach is by Transverse-Momentum-Dependent PDFs (TMDs), which describe the subtle effects on intrinsic transverse parton momenta. These effects become visible in hadronic Drell-Yan (DY) and Semi-Inclusive DIS (SIDIS) processes (described in 2.2.1, 2.2.2)[13].

The basics of the theory of generalized parton distributions are summarized in the following section.

2.1.1 Generalized Parton Distributions

The concept of generalized parton distributions (GPDs) was introduced by Müller [39], Radyushkin [40] and Ji [41]. The GPDs contain the most complete description of the internal quark-gluon structure of hadrons so far.

As was already mentioned GDPs provide information about the spatial distribution of partons carrying a momentum fraction x. Moreover, the GDPs may for the first time provide an insight into the orbital momenta of quarks and gluons.

There are four of these distributions: nucleon-helicity conserving $\mathrm{H^{f,g}(x,\xi,t)}$, $\mathrm{\widetilde{H}^{f,g}(x,\xi,t)}$ and nucleon-helicity inverting $\mathrm{E^{f,g}(x,\xi,t)}$, $\mathrm{\widetilde{E}^{f,g}(x,\xi,t)}$ (here index f stands for quark flavours u, d, s and g for gluons, the GDPs marked with $\sim$ are polarized, the other unmarked are unpolarized), which depend on three variables: the average longitudinal momentum fraction of the struck parton in the initial and final states, a momentum transfer t to the target nucleon, and a parameter ξ [42]. These additional kinematic variables are defined in following paragraphs.

The Mandelstam variable

$$t = (p - p')^2 = -\Delta^2 \tag{2.5}$$

specifies the transferred four-momentum between the initial and final state of the nucleon. In the so-called Bjorken limit

$$Q^2 \to \infty,\ x_B = const. \tag{2.6}$$

Dimensionless variable ξ ("skewness") is in Bjorken limit established as

$$\xi = \frac{x_B}{2 - x_B} \tag{2.7}$$

It characterizes the direction of the momentum transfer t relative to the direction of the momentum of the nucleon in an infinite momentum frame.

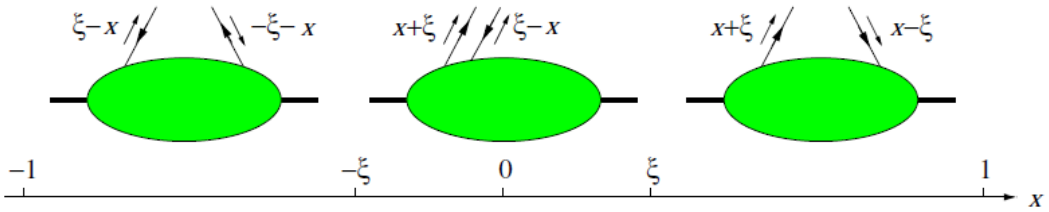

Figure 2.5: The parton representation of GDPs in three different regions of x [43]

The momentum fraction of the interacting quark in the initial and in the final state is given by the sum $x + \xi$ and the difference $x - \xi$ respectively. Generalized parton distributions are defined for $x \in$ [-1,1]. Negative values of x describe the momentum fractions for antiquarks. There are three distinct region in x for a given value of $\xi > 0$, these three regions are shown in Fig. 2.5:

- For $\xi < x < 1$ both momentum fractions $x+\xi$ and $x-\xi$ are positive. The GPDs describe the emission of a quark by the incoming hadron and its absorption by the outgoing one.
- For -1 $< x <$ $-\xi$ both $x + \xi$ and $x - \xi$ are negative. One has emission and reabsorption of an antiquark with momentum fractions $\xi - x$ and $-\xi - x$.
- A central region $-\xi < x < \xi$ has no analogue in the usual parton distributions. One has $x + \xi \geq 0$ and $x - \xi \leq 0$. The second momentum fraction is now interpreted as belonging to antiquark with momentum fraction $\xi - x$ emitted from the initial proton.

The first two cases $\xi < x < 1$ and -1 $< x < \xi$ are known as DGLAP (Dokshitzer, Gribov, Lipatov, Altrarelli, Parisi) regions and the central region $-\xi < x < \xi$ as the ERBL (Efremov, Radyushkin, Brodsky, Lepage) region [43] [44].

How the GPDs depend on x and ξ is in large measure unknown today. A model calculation for $\mathrm{H^u(x, \xi, t = 0)}$ is shown in Fig. 2.6.

In the limit where $p = p$‘ which implies $t = 0$, $\xi = 0$, helicity conserving GPDs become usual PDFs.

In the limit case for $\xi = 0$, the parton carries the same longitudinal momentum fraction x in initial and final state. Hence the momentum transfer $t = -\Delta^2 = -(\Delta_\mathrm{L}^2 + \Delta_\perp^2)$ (where L stands for longitudinal and $\perp$ for transverse) is purely transverse, i.e. $t = -\Delta_\perp^2$. In this case, in analogy to the form factors, the Fourier transformation of the GPD $\mathrm{H^f(x, 0, -\Delta_\perp^2)}$ for fixed x describes the spatial distribution $q_f(x, b_\perp)$ of partons of species f carrying the longitudinal momentum fraction x located at transverse distance $b_\perp$ (so-called an impact parameter) from the center of momentum of the nucleon. The mentioned Fourier transform is called an impact parameter dependent parton distribution and it is defined as

$$q_f(x, b_\perp) = \int \frac{d^2\Delta_\perp}{(2\pi)^2} e^{-i\Delta_\perp b_\perp} H^f(x, 0, -\Delta_\perp^2) \tag{2.8}$$

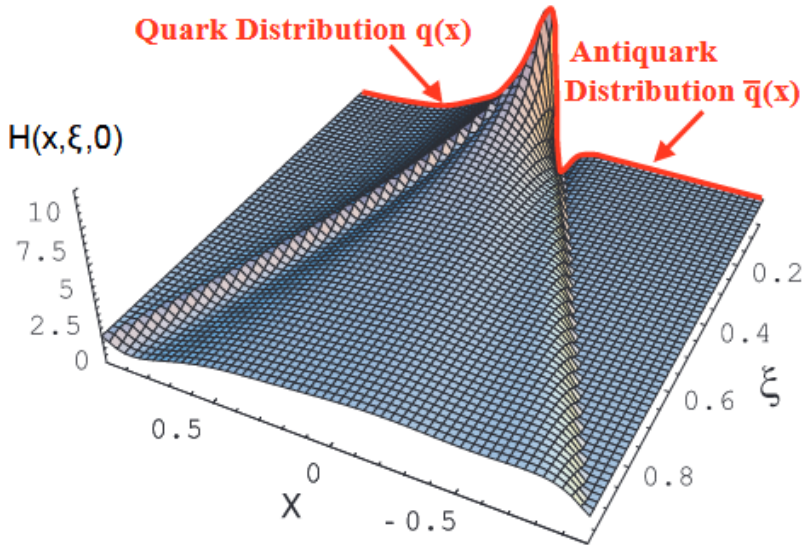

Figure 2.6: The model calculation for $H^u(x, \xi, t = 0)$, the thick (red) line at $\xi = 0$ corresponds to the normal PDFs. The outer region $|x| > \xi$ is accessible via the DVCS process [45]

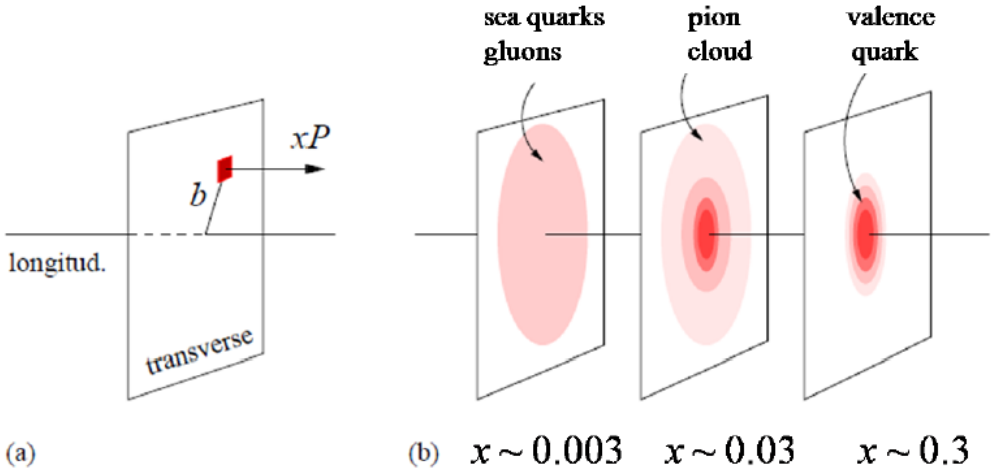

Figure 2.7: a) The Fourier transformation of the GPD $H^f(x, 0, -\Delta_\perp^2)$ describes the distribution of quarks with respect to longitudinal momentum xp and transverse position $b_\perp$, b) 3D image of the quark structure of the nucleon. Depending on the momentum fraction x, either the valence quarks, the pion cloud or the sea quarks and gluons are resolved. [13]

The "three-dimensional" impact parameter dependent parton distribution $q_f(x, b_\perp)$ can be interpreted as providing a set of "tomographic images" of the nucleon. It is visualized in Fig. 2.7. Two dimensions give a position of a transverse plane and one represents longitudinal fractional momentum x[27] [13] [28] [46].

Experimental access to GPDs is provided in suitable hard scattering processes with exclusive final states, especially in processes initiated by a highly virtual photon (mainly DVCS and hard exclusive meson production (HEMP)) [44].

[27] The longitudinal position and x can not be measured simultaneously. It is forbidden by the uncertainty principle. [46]

2.2 Compass physics program

The COMPASS physics program started in summer 2002 with SIDIS experiments. After the shutdown in 2005, these measurements resumed in 2006 and 2007. The spin structure measurements were continued in 2010 and 2011. The years 2008 and 2009 were dedicated to the hadron spectroscopy program with pion and proton beams scattering off a liquid hydrogen target and nuclear targets. Part of 2009 was dedicated to the study of the pion polarizability using Primakoff scattering of pions from heavy nuclei.

After the hardware upgrade, the program was continued in 2012 under COMPASS phase-II. The phase-II of the COMPASS experiment is primarily focused on the transverse and 3D structure of nucleons using DVCS, HEMP, SIDIS and polarized DY reactions [47]. The upgrade included the addition of detectors particularly important for exclusive measurements - Recoil Proton Detector CAMERA and electromagnetic calorimeter ECAL0 (described in Sec.1.2 and Sec.1.3.2). COMPASS-II started in 2012 with a Primakoff run and a DVCS pilot run. The DVCS program uses positive and negative 160 GeV polarized muon beam and a long unpolarized proton target (liquid hydrogen target LH_2 introduced in Sec.1.2) with the huge recoil detector CAMERA. The values of Bjorken variable x_B and photon virtuality Q^2 lie within the following limits:

- x_B is ranging from 0.01 to 0.15
- Q^2 is ranging from 1 to 10 GeV^2

Thus COMPASS explores the uncharted x_B territory between the HERA collider experiments H1 and ZEUS and the fixed-target experiments as HERMES and Jefferson Laboratory (JLab) [13]. A comparison with domains covered by these experiments is shown in Fig. 2.8.

First test measurements were performed in 2008 and 2009 but without ECAL0. The first proper measurement was taken in 2012 [48]. The years 2016 and 2017 were also dedicated to DVCS measurement and simultaneously data on HEMP and SIDIS were collected. The first-ever polarized Drell-Yan measurement with a beam of negative pions and a polarized proton target was successfully performed in 2015 and the data taking was resumed in 2018.

For 2021 after long shut-down 3, the following running schedule is proposed [49]:

- 2021: one year[28] of SIDIS data taking with the transversely polarized deuteron target and at early stage test measurements for the proton radius measurement
- 2022: under the condition of the successful testing phase in 2021, one year of data taking for the proton radius measurement. This will happen within the AMBER (Apparatus for Meson and Baryon Experimental Research) experiment, the next-generation successor of the COMPASS experiment. The AMBER will build on COMPASS's legacy and take it to the next level. Besides

[28] By one year of data taking is intended 150 days of data taking. [49]

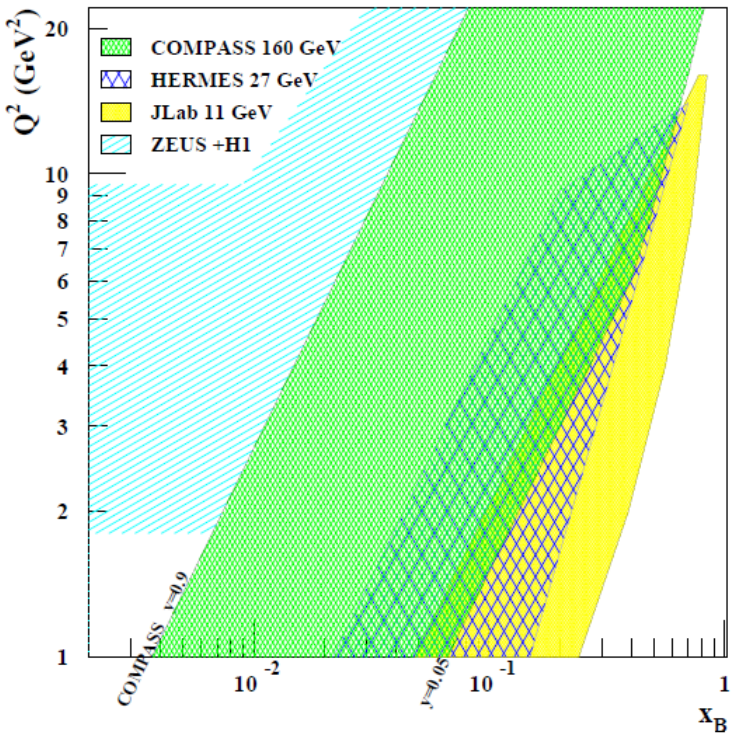

Figure 2.8: Kinematic domains for measurements of hard exclusive processes for the COMPASS experiment, HERMES, JLab and the HERA collider experiments H1 and ZEUS [13]

of determination of the proton's charge radius will be studied the spectroscopy of mesons and baryons by using dedicated meson beams and their structure via the Drell-Yan [50].

The following sections provide basic principles of the main physics processes studied by the COMPASS experiment.

2.2.1 Semi-Inclusive Deep Inelastic Scattering – SIDIS

The information available from the inclusive DIS process has inherent limitations. Deep inelastic scattering is not sensible to each individual quark flavour. Therefore is realized semi-inclusive deep inelastic scattering. The SIDIS process offers a unique opportunity for determining the spin, flavour, and the sea structure of the nucleon, thereby significantly enriching our understanding of QCD and the nucleon structure [51].

Semi-Inclusive DIS measurements in the COMPASS experiment were realized in 2002-2011 with polarized targets and with a pure proton target[29]. These measurements are complementary to DY experiments [13].

The SIDIS process is a specific case of deep inelastic scattering (described in Sec.2.1). In the DIS process, a lepton (muon in the case of the COMPASS experi-

[29]The DIS process is monitored at the COMPASS experiment for verification of the measured data and Monte Carlo simulations.

ment) is scattered off a target nucleon. Only the final state lepton is observed (e.g. $l + p \rightarrow l' + X$). In the case of SIDIS, one hadron from the final state hadrons X is observed in addition (e.g. $l + p \rightarrow l' + h + X$) [52]. The diagram of the SIDIS process is shown in Fig. 2.9.

2.2.2 Drell-Yan process - DY

The key feature of the Drell-Yan process, when compared with the SIDIS process, is the possibility to study a proton TMD convoluted with a pion TMD. The Drell-Yan process is observed in the hadron-hadron collisions where an electromagnetic annihilation of a quark-antiquark pair occurs and the two leptons in the final state are produced. This process is shown in Fig. 2.9.

COMPASS uses the dimuon channel, to take advantage of the excellent muon detection by the spectrometer, with the goal of studying the TMDs of the valence up quark in the proton. The Drell–Yan measurements at COMPASS were realized with 190 GeV pion beam and transversely polarized proton target. High intensity beam is needed owing to the low cross-section of the studied reaction.

A short two months DY pilot run at COMPASS happened in 2014. The DY measurements continued on 2015 and after shutdown in 2018 [53] [54].

2.2.3 Primakoff process

The Primakoff reaction $\pi^- + (A, Z) \rightarrow \pi^- + (A, Z) + \gamma$ as it was realized at COMPASS is illustrated in Fig. 2.10. In this process, high-energetic pions react

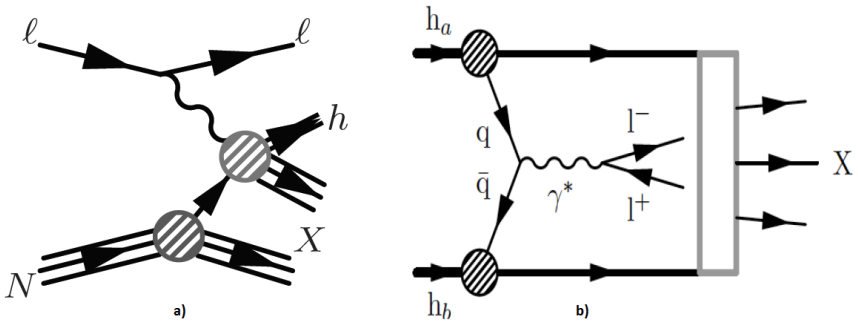

Figure 2.9: The Feynman graphs for a) semi-inclusive DIS [55] b) Drell-Yan scattering [53]. The dashed circles represent PDF, the grey rectangle denote hadronization.

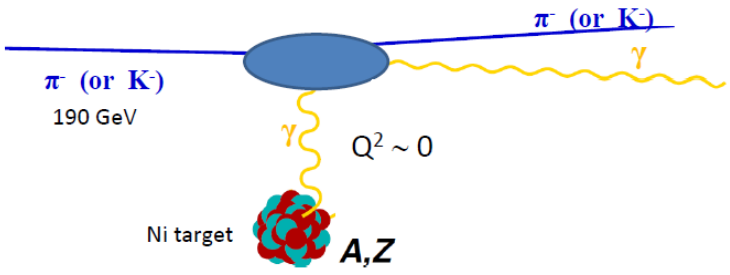

Figure 2.10: The diagram of Primakoff process as it was realized at COMPASS [56]

with the quasi-real photon field surrounding the target nuclei. It can be treated as Compton scattering of the pion off a virtual photon, provided by the nucleus. Using this process the pion polarizability is extracted from the measured cross-section shape [57] [58].

2.2.4 Deeply Virtual Compton Scattering - DVCS

In hard exclusive photon or meson production, observables like cross-sections and asymmetries in dependency of the beam or target polarization or beam charge contain information about the GPDs. The GPDs H, $\widetilde{H}$, E, $\widetilde{E}$ of the u and d quarks can be experimentally investigated. However, they can not be extracted from the data directly. Instead, the functional dependency of the GPDs on x, ξ, and t is parametrized by theoretical models and the parameters are determined by comparison with the data.

One of the processes that will help to determine the GPDs is the deeply virtual Compton scattering (DVCS) [46]. DVCS is the special case of DIS where the struck quark returns back into the hadron, such that the hadron stays intact.

Measurements of DVCS are mostly realized via the process of leptoproduction of a real photon. In this reaction, the final photon can be emitted either by the leptons (Bethe-Heitler process) or the proton (DVCS process). It means that DVCS has the same final state as the competing Bethe-Heitler (BH) process. The electromagnetic BH process is elastic lepton-nucleon scattering with a photon emitted by either the incoming or outgoing lepton. Such a photon does not carry information about the nucleon and therefore can not be used for the determination of GDPs. Thus the BH proces is completely calculable in quantum electrodynamics (QED). The scattering cross-section of the DVCS reaction can be factorized accordingly into a "hard" elec-

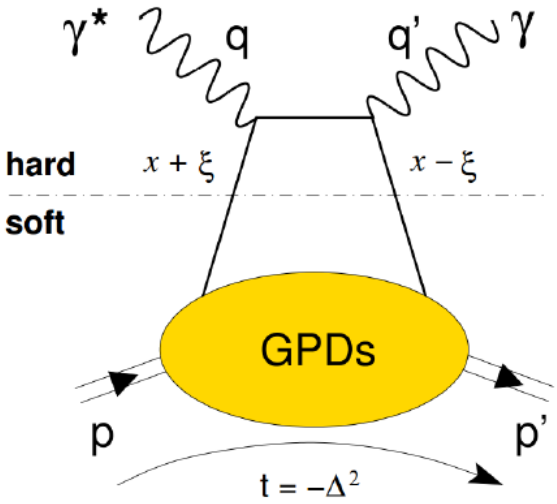

Figure 2.11: A handbag-diagram of DVCS with "hard" and "soft" parts. A quark with longitudinal momentum fraction $x + \xi$ absorbs a virtual photon $\gamma*$ with virtuality Q^2 and four-momentum q. Then it emits a real photon γ with four-momentum q' which reduces the longitudinal momentum fraction to $x - \xi$. The quark GPDs describe the correlation between the initial and final state quarks for given values of t and Q^2. [13]

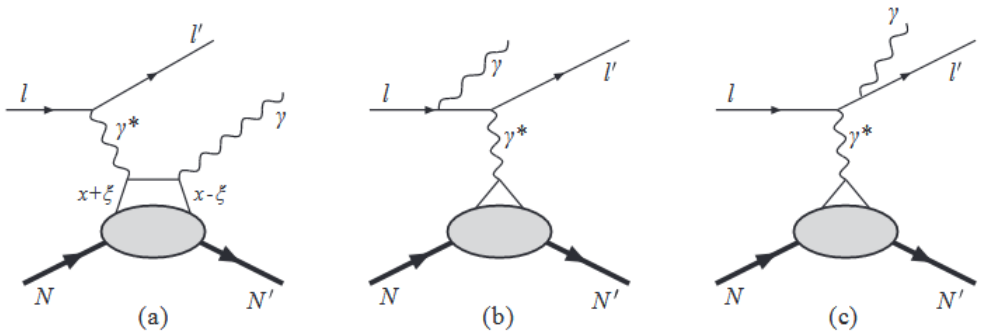

Figure 2.12: Processes of leptoproduction of real photon: a) deeply virtual Compton scattering, b) and c) Bethe-Heitler process [46]

tromagnetic and "soft" hadronic part. Factorization means, that the form factor of the process can be decomposed as the product of the corresponding QED and QCD matrix elements. The "hard" part is calculable in perturbation theory of QED and the "soft" part is described by GPDs. The factorization of the process into the "soft" and the "hard" part in DVCS is visualised in Fig. 2.11 [13] [59].

For a better illustration, both the DVCS process and the Bethe-Heitler process are shown together in Fig. 2.12.

2.2.5 Hard Exclusive Meson Production - HEMP

Besides DVCS, there is another process enabling determining GPDs – hard exclusive meson production (HEMP) also known as deeply virtual meson production (DVMP). The HEMP process is meson production at high values of Q^2. The HEMP measurements, complementary to DVCS measurements, are sensitive to both chiral-even and chiral-odd GPDs. The chiral-odd GPDs are not available via DVCS. The meson production is also divided into two categories: the "soft" scattering regime describing particle production involving small momentum transfers and the "hard" scattering regime, responsible for producing particles with momenta of several GeV/c or more [60]. The GPDs describe the "soft" dynamics of the nucleon emitting and absorbing a (anti-)quark or gluon [61].

The first results from the COMPASS experiment were obtained from COMPASS phase-I (2003-2010) with a muon beam and a polarized target. However, there was a disadvantage of unsecured exclusivity of measurements. In COMPASS phase-II was used recoil proton detector CAMERA. With the time-of-flight measurement, CAMERA determines the kinematic properties of a recoiling proton and plays an important role in ensuring the exclusivity of an event. The COMPASS phase-II measurements also provide bigger statistics of the HEMP process [62].

Both pseudoscalar mesons (spins of the quark and antiquark constituting these mesons are oriented in opposite directions and the total spin is zero) - π, η, and vector mesons (spins of the quark and antiquark are oriented in the same direction and the total spin is equal to one) - ρ, ω, ϕ, J/ψ can be produced. The best measurable are productions of ρ^0, ω, π^0, whose decay modes can be easily detected and distinguished from the background.

Exclusive π^0 Production

In the quark model, the π^0 consists of light-flavor quark-antiquark pairs, $\bar{u}u$ and $\bar{d}d$. The schematic diagram for the hard exclusive meson production of π^0 process is shown in Fig. 2.13. A muon with initial (final) four-momentum k (k') scatters off a (anti-)quark of the target proton with initial (final) four-momentum p (p') by the exchange of a virtual photon γ^* with four-momentum q. The creation of the meson π^0 with four-momentum q' is described by a distribution amplitude (DA) [61]. The scheme of this process is $\mu + p \rightarrow \mu' + p' + \pi^0$. Pion subsequently decays into two photons $\pi^0 \rightarrow \gamma_l + \gamma_h$ (where γ_l has lower energy while γ_h has higher energy). This process is an important background for DVCS, as one of the generated photons is often below the threshold or not detected.

The cross-section of this process is significant for GDP theory. Experimental data are compared with theoretical hypotheses. Data from 2012 measurements with the muon beam and the liquid hydrogen target were presented in the article "Measurement of the cross-section for hard exclusive π^0 leptoproduction" [63]. Its results provided important input for modelling GPDs. In the context of the phenomenological Goloskokov-Kroll model, the statistically significant transverse-transverse interference contribution constitutes clear experimental evidence for the existence of the chiral-odd GPD $\bar{E}_T$. The dependences of the measured cross-section on $|t|$ and ϕ are illustrated in Fig. 2.14. The variable ϕ is defined as the azimuthal angle between the lepton scattering plane and the hadron production plane as shown in Fig. 2.15.

The data are compared with two predictions of the Goloskokov-Kroll (GK) model [64] [65]. The dashed-dotted curve represents the cross-section from the earlier version of the GK model [64]. It is obvious that there is a significant discrepancy between the cross-section predicted by the earlier version of the model and the measurement. The dotted curve corresponds to the later version of the model [65], which was corrected by the results presented in [63]. Therefore, it agrees better with the experimental data.

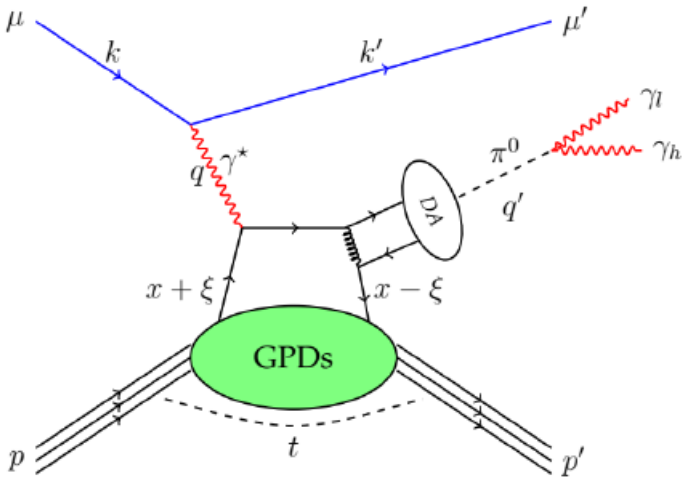

Figure 2.13: A handbag diagram of π^0 production [61]

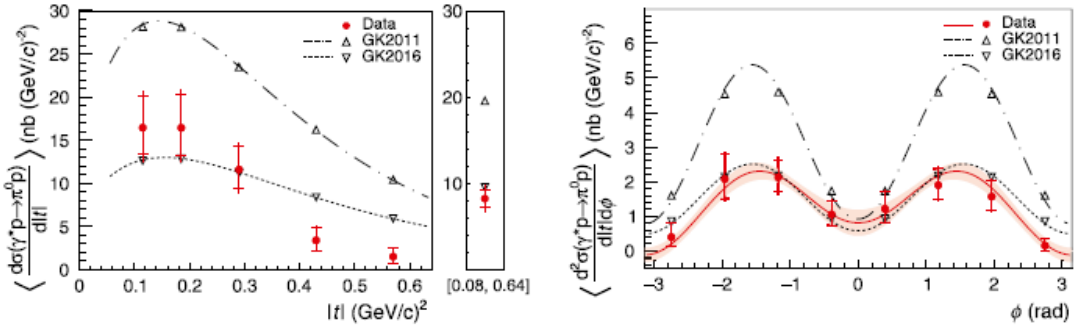

Figure 2.14: Left: Average value of the differential virtual-photon proton cross section as a function of |t|, right: the dependence of the measured cross-section on ϕ [63]

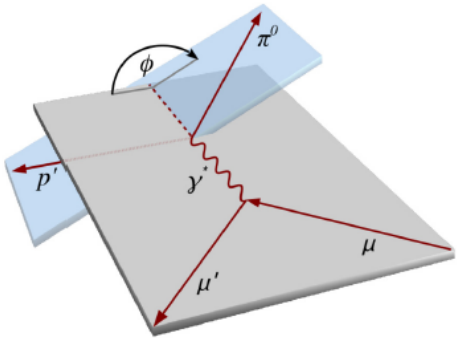

Figure 2.15: Definition of ϕ, the azimuthal angle between the lepton-scattering and π^0 production plane [63]

Following the pilot run in 2012 with a 4-week data taking, in COMPASS 2016 and 2017 runs with few detector upgrades was accumulated about 10 times more statistics than in the 2012 pilot run. The kinematic range was expanded substantially for these measurements. Thus COMPASS probed GPDs within the phase space where the sea quarks contribute significantly [62]. The data from 2016 and 2017 runs are currently being analyzed.

Exclusive ω Production

The vector meson ω is produced in the reaction between muon and proton. Subsequently, it decays into three pions π^+, π^-, π^0 or less likely into π^0, γ (with branching ratio 8.3 %) or into π^+, π^- (with branching ratio 1.5 %) [8]. As was already mentioned π^0 meson afterwards decays into two photons.

$$\mu + p \to \mu' + p' + \omega$$
$$\hookrightarrow \pi^+ + \pi^- + \pi^0 \qquad \text{Branching ratio} \approx 89\ \%$$
$$\hookrightarrow \gamma_l + \gamma_h \quad \text{Branching ratio} \approx 99\ \%$$

The spin structure of reaction: $\mu + p \to \mu' + p' + \omega$ is described by Spin Density Matrix Elements (SMDEs). They are related to helicity amplitudes that describe transitions between specific spin states of virtual photon, target proton, produced

vector meson and recoiling proton. For an unpolarized nucleon target SDMEs only depend on the helicities of virtual photon and produced meson.

The measured SDME values can be used to establish a hierarchy of helicity amplitudes, to evaluate the contribution of unnatural-parity-exchange transitions, to test the hypothesis of s-channel helicity conservation (SCHC), and to assess the role of chiral-odd, i.e. parton helicity-flip GDPs in exclusive ω production. The measurements of SDMEs can also provide further restrictions of GPD parametrizations beyond those obtained from measurements of cross-section and spin asymmetries for HEMP.

From the angular distribution of particles produced in the exclusive ω production, a total number of 23 SMDEs have been extracted. Comparison of these 23 SDMEs with Goloskokov-Kroll GPD model prediction is shown in Fig. 2.16.

The data from the 2012 run allow sorting SDMEs into five different classes depending on the helicity transitions from the virtual photon γ^* to the meson ω. Results from 2012 data taking, providing important information for modelling GPDs, are presented in [66]. They cover a kinematic range that extends considerably beyond the ranges of earlier experimental data in SDMEs for exclusive ω leptoproduction.

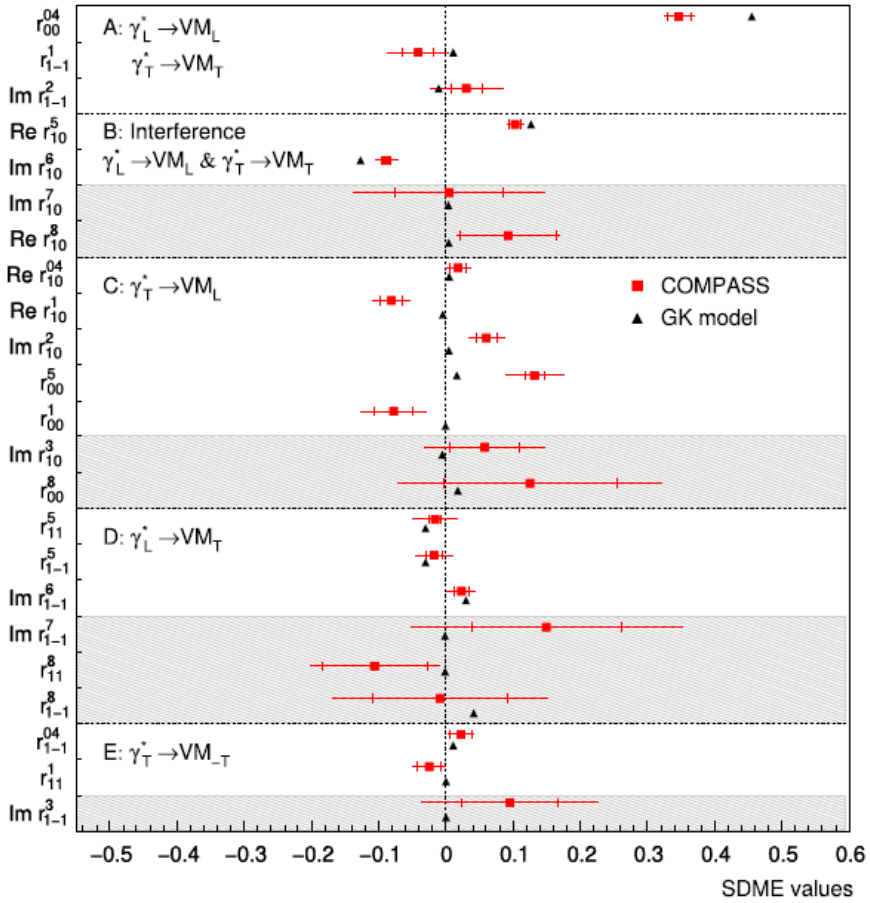

Figure 2.16: Comparison of the 23 SDMEs for exclusive ω leptoproduction with the calculations of the Goloskokov-Kroll GPD model. Inner error bars represent statistical uncertainties and outer ones statistical and systematic uncertainties added in quadrature. Unpolarized (polarized) SDMEs are displayed in unshaded (shaded) areas. [66]

However, the 2012 data do not have sufficient statistics to determine the cross-section of this process. The determination of cross-section will be processed from the data from 2016 and 2017 data taking [62] [66].

Exclusive ρ^0 Production

Hard exclusive ρ^0 meson production in lepton-nucleon scattering provides a convenient tool for studying the production mechanism and the structure of the nucleon. There were numerous measurements of ρ^0 HEMP in lepton scattering off hydrogen, deuterium, and ^{3}He targets. The measurements were performed for example at CORNELL, Jefferson Lab, HERMES, Fermilab, and Hera. The present COMPASS results on SDMEs for exclusive ρ^0 muoproduction have the potential to further constrain the GPDs. The 23 SDMEs extracted from ρ^0 are illustrated in Fig. 2.17 [67].

For analysis can be accepted events with one reconstructed vertex and the same topology as process:

$$\mu + p \to \mu' + p' + \rho^0$$
$$\hookrightarrow \pi^+ + \pi^- \text{ Branching ratio} \approx 99\ \%$$

As in the case of the ω production, the production of ρ^0 in 2012 COMPASS

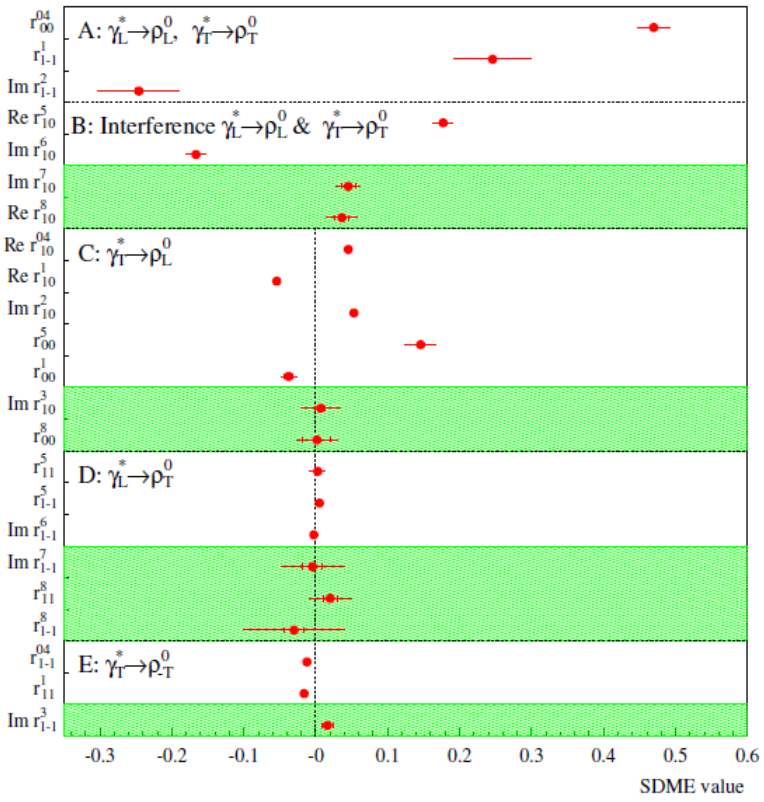

Figure 2.17: The 23 SDMEs for exclusive ρ^0 leptoproduction. Inner error bars represent statistical uncertainties and outer ones statistical and systematic uncertainties added in quadrature. Unpolarized (polarized) SDMEs are displayed in unshaded (shaded) areas. [67]

experiment data taking does not have sufficient statistics for the determination of cross-section. It will be possible to determine it from the 2016 and 2017 data.

Other measurable HEMPs are for vector mesons J/ψ and ϕ. They will be analysed from 2016 and 2017 data.

The J/ψ meson consists of $c\bar{c}$ quarks. The main investigated decay mode is the process: $J/\psi \to \mu^+ + \mu^-$ with branching ratio ≈ 6 %. Other decay modes such as $J/\psi \to e^+ + e^-$ (with branching ratio ≈ 6 %) or decay into hadrons (with branching ratio ≈ 88 %) can also be studied. However, the gluons produced in the dominant hadronic decay mode $J/\psi \to g + g + g$ (with branching ratio ≈ 64 %) can not be detected. Therefore is mainly used decay mode $J/\psi \to \mu^+ + \mu^-$ which is easily detected by the COMPASS experiment. Data on SDMEs of meson J/ψ production will give unique information about gluon contribution.

The ϕ meson is composed of $s\bar{s}$ quarks. The most probable decay mode is: $\phi \to K^+ + K^-$ with branching ratio ≈ 49 %. Again, there is an important gluon contribution in this process. Data on cross-section and SDMEs are important for model analyses.

Large mass particles and their main decay modes are significant for research of the nucleon structure. For example, the mass of ω meson is 782.65 MeV, of ϕ is 1019.461 MeV, and 3096.9 MeV is the mass of J/ψ meson. It is interesting that although the mass of π^0 meson is only 134.977 MeV its production is measured because it is simply detected. On the other hand, the pseudo-scalar meson η with the mass 547.862 MeV is not currently analyzed at COMPASS. This meson subsequently decays by neutral modes into two photons (with branching ratio ≈ 39 %) or for example, three π^0 (with branching ratio ≈ 33 %) which leads to the production of six photons [8]. However, studies of η decays require high statistics precision experiments [68].

Chapter 3

Calibration of the Straw detector

3.1 Survey measurement

In order to achieve the optional reconstruction performance in the COMPASS experiment, a precise knowledge of the position and orientation in space of tracking detector planes of the COMPASS spectrometer is mandatory. Initially, tracks are reconstructed using detector positions determined by the geometrical survey of the experimental setup. In many cases, the geometrical survey does not reach a precision that is comparable to the spatial resolution of the detectors. Then it is used as the starting point for an alignment procedure. The alignment of the tracking detectors uses a sample of reconstructed tracks and it is divided into three steps. Each step uses a different set of data and it is repeated until the corrections become negligible compared to the detector resolution.

The first step uses data recorded with switched off spectrometer magnets. Due to this fact, straight trajectories are assumed and all spectrometer arms contribute to the reconstruction of a particle track. Four detector planes are fixed and their positions are determined by an optical survey of the experimental setup. For all other planes, alignment is performed by minimising their deflections. Corrections for a translation around the measured coordinate, a rotation around the beam axis, and the effective pitch are introduced.

For the second step of the procedure, spectrometer magnets are switched on and the detector planes downstream of the target are aligned. Their magnetic field influences internal processes of charge propagation in gaseous detectors and shifts the position of the mechanical support of some detectors.

As the third step, the beam telescope upstream of the target is aligned with respect to the spectrometer that is kept fixed in space. This is essential for the optimization of the reconstruction of the vertices in the target.

The alignment of the tracking stations is completed by a separate procedure for the silicon stations. The calorimeters are aligned with respect to the tracking detectors by a different procedure [5].

3.1.1 Arrangement of the survey measurement

As was already mentioned, the COMPASS experiment uses only one straw detector module since 2016 - called ST03, which is composed of 6 double layers (X1, Y1, U1, V1, Y2, X2 their arrangement is shown in Fig. 3.1). Each of them has exactly 4 cm and consists of two layers of straws (upstream (u) layer located closer to the target and downstream (d) layer which is farther from the target).

Survey measurements use a coordinate system illustrated in
Fig. 3.2. This cartesian reference frame related to the beam is defined by: origin – an intended centre of the target; x-axis – vertical, positive to the top; y-axis – horizontal, perpendicular to the beam line, positive toward Jura mountains[30]; z-axis – horizontal, along the beam line, positive in the beam direction [69].

During straw survey measurement, 4 points are directly measured. Subsequently, the values of their coordinates are used for the calculation of the position of required points. The survey probe has been placed 1 cm from the downstream end of the Y2 double layer. It is 2 cm long, which means that a part of the survey probe overlaps the X2 double layer. The photo of the placement of the survey probe, as it was used in 2021, is shown in Fig. 3.3. The 4 survey measurement points are distributed depending on their position in relation to the Jura (J) and Salève (S) mountains and their vertical position (top (T) or bottom (B)).

The overall arrangement of ST03 is depicted in Fig. 3.2. In addition, Fig. 3.2 illustrates 6 points which position needs to be determined. They are situated in the middle of the sections (A, B, C) of the straw chambers (described in 1.4). In each section, there are located two of these points (one in the upstream layer (u) and one in the downstream layer (d)) [71].

When determining these points, it is also necessary to pay attention to the internal structure of double layers. The cross section of a double layer is illustrated in Fig. 3.4. It is obvious that it consists of three main sections (A, B, C). The number of straws

[30] When determining the position in the COMPASS experimental setup, the Salève and Jura directions corresponding to the locations of the mountains of the same name in France and Switzerland are used instead of the left and right.

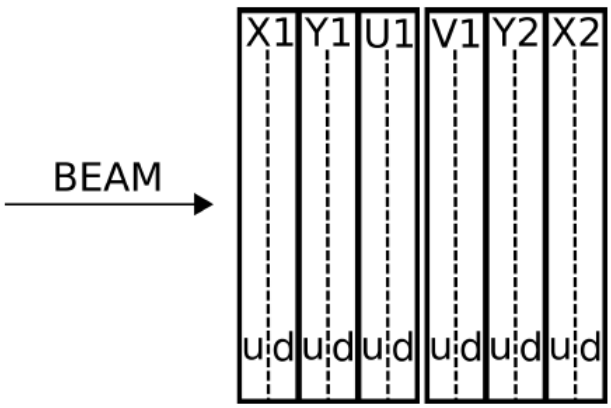

Figure 3.1: Six double (upstream (u) and downstream (d)) layers of detector straw ST03. X represents vertical straw plane, Y horizontal straws and U, V inclined straws. [14]

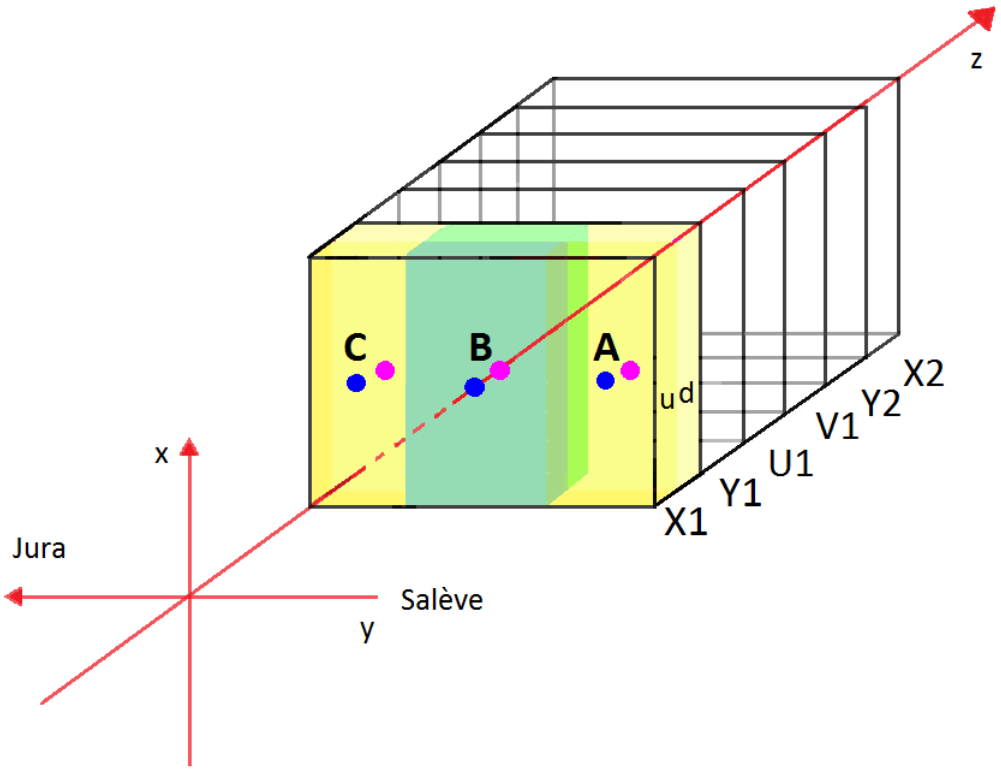

Figure 3.2: The overall scheme of the detector straw module ST03 arrangement. 6 points, whose positions are determined, are represented by blue and pink dots. The blue dots depict the points in the upstream layer. The pink dots stand for the points in the downstream layer. Jura and Salève directions corresponds to the locations of the mountains of the same name.

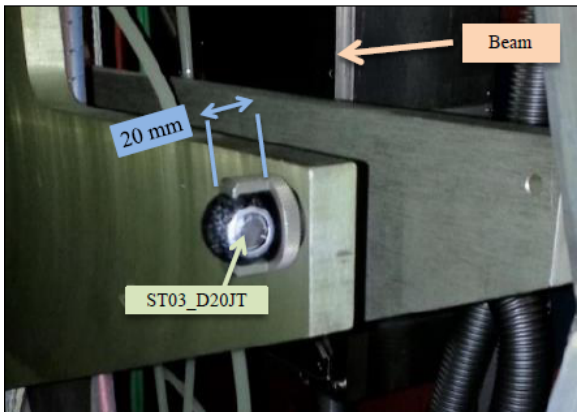

Figure 3.3: The placement of the survey probe as it was used during the 2021 measurement [70]

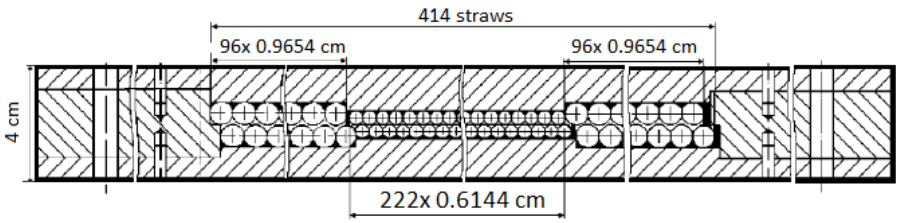

Figure 3.4: The cross section of the double layer. The detailed dimensions refer to one layer of the type X, U, and V chambers.

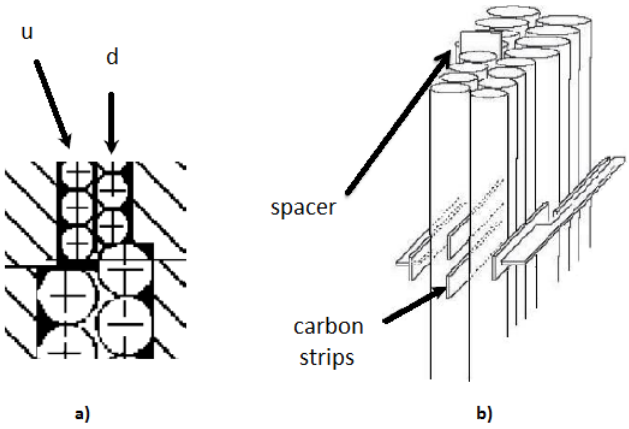

Figure 3.5: The detailed outline a) of the radii difference between straws in inner and outer part b) of the placement of the carbon spacer and the carbon strips [71]

with 0.6144 cm diameter for X, V, and U chambers is 96 for both outer sections A, C and 222 straws with 0.9654 cm diameter for the inner part A. However, for chambers of type Y the numbers of straws are different. In inner section B, there are 192 straws and in both outer parts, there are 64 straws. The diameters of these straws remain unchanged. This difference between numbers of straws is caused by the shape of active areas of the chambers.

As was already mentioned in 1.4 the downstream layer is shifted by half of the diameter with respect to the upstream layer. Therefore, it is necessary to use a 0.1755 cm carbon spacer between the inner and outer part. Due to the difference in the radii of the straws, a gap is created here. This gap is filled with the spacer. The placement of the spacer is shown in Fig. 3.5. Besides carbon spacer, double layers contain also 0.0506 cm carbon strips placed between u and d layers. These thin strips help fix the position of the straw [71] [72].

3.1.2 Results of the survey measurement

The survey measurement is realized typically every year when COMPASS is running (if needed several times). Due to the shutdown results from 2018 (Tab. 3.1) were the last survey before current one taken on May 19th 2021 (Tab. 3.2). From the values shown in Tab. 3.1 and Tab. 3.2 is possible to deduce that positions of points measured in 2018 and 2021 are different.

Name	x [m]	y [m]	z [m]
JB	-1.3986	2.3412	5.5371
JT	1.4059	2.3379	5.5369
SB	-1.4038	-2.3496	5.5424
ST	1.4018	-2.3530	5.5422

Table 3.1: Coordinate values of the positions of the four points (Jura bottom (JB), Jura top (JT), Salève bottom (SB), Salève top (ST)) directly measured during the survey measurement in 2018 [69]

Name	x [m]	y [m]	z [m]
JB	-1.3978	2.3407	5.5362
JT	1.4057	2.3373	5.5364
SB	-1.4041	-2.3484	5.5417
ST	1.4006	-2.3526	5.5422

Table 3.2: Coordinate values of the positions of the four points (Jura bottom (JB), Jura top (JT), Salève bottom (SB), Salève top (ST)) directly measured during the survey measurement in 2021 [70]

The data differ on average by 0.608 mm[31]. The biggest difference is between y-axis values (on average 0.675 mm). Such differences are typically observed because of the manipulation of the detector[32] or because of intended or unintended modifications of stoppers and spacers that puts the detector in correct position with respect to beam and other detectors and magnets.

The positions of 36 points (6 in each from 6 double layers) are calculated from the results of the survey measurement considering the inner structure of the detector straw module described above. The results for data from the 2021 measurement are shown in Tab. 3.3. They do not have significant distinctions from 2018 results.

It indicates that there were no intended changes in module arrangement and the detector is in the correct position. These values are saved in detector description file "detectors.dat", which serves as a start point for the alignment procedure and is later used for many tasks like reconstruction of particle tracks and Monte Carlo generations.

3.2 The calibration of the RT relation of the Straw detector

As was already mentioned the detector straw works on the principle of the drift chamber. When a charged particle passes through the straw tube filled with a gas and connected to a high voltage, it ionizes the gas anywhere within the straw volume and creates primary electron-ion pairs. The originated electrons drift towards the anode (wire) and the resulting ions drift to the cathode (thin conductive tube, the straw wall, that surrounds the wire). Close to the wire, the electrons are accelerated due to the high electrical field. If the electrons get enough energy to further ionize the gas, they will create secondary electron-ion pairs avalanche and the signal will be generated. This process causes that the electrons are collected very quickly while the ions slowly drift towards the cathode.

The current signal is collected on the electrodes. It is rather formed by induction due to the movement of the ions and electrons as they move towards the cathode and anode, than by the collection of charges itself [73]. The first signal generated in a straw travels to the motherboard situated at end of the straw.

[31] Unless otherwise specified, coordinates are given with an accuracy of 0.3 mm at one sigma level. [71]

[32] The detector is hanging on rails and for repairs of this detector or surrounding detectors, it needs to be moved along the rails.

Name	x [cm]	y [cm]	z [cm]
X1uA	-0.1750	-114.9590	534.5458
X1uB	0.1100	-0.4214	534.5800
X1uC	0.3950	114.2917	534.2633
X1dA	-0.1750	-115.4417	535.5618
X1dB	0.1100	-0.7286	535.2450
X1dC	0.3950	113.8090	535.2793
Y1uA	-90.0943	-0.7650	538.5458
Y1uB	-0.0436	-0.5750	538.5800
Y1uC	89.8316	-0.3850	538.2633
Y1dA	-89.6116	-0.7650	539.5618
Y1dB	0.2636	-0.5750	539.2450
Y1dC	90.3143	-0.3850	539.2793
U1uA	-20.2186	-113.6575	542.5458
U1uB	-0.0182	-0.7366	542.5800
U1uC	20.1517	112.0114	542.2633
U1dA	-20.1348	-113.1821	543.5618
U1dB	0.0352	-0.4341	543.2450
U1dC	20.2355	112.4868	543.2793
V1uA	19.8739	-113.7183	546.5458
V1uB	0.2348	-0.6984	546.5800
V1uC	-19.3737	112.1486	546.2633
V1dA	19.7901	-113.2429	547.5618
V1dB	0.1815	-0.3959	547.2450
V1dC	-19.4575	112.6239	547.2793
Y2uA	-89.6116	-0.7650	550.5458
Y2uB	0.2636	-0.5750	550.5800
Y2uC	90.3143	-0.3850	550.2633
Y2dA	-90.0943	-0.7650	551.5618
Y2dB	-0.0436	-0.5750	551.2450
Y2dC	89.8316	-0.3850	551.2793
X2uA	-0.1750	-114.9590	554.5458
X2uB	0.1100	-0.4214	554.5800
X2uC	0.3950	114.2917	554.2633
X2dA	-0.1750	-115.4417	555.5618
X2dB	0.1100	-0.7286	555.2450
X2dC	0.3950	113.8090	555.2793

Table 3.3: Calculated positions of 36 points through 6 double layers of straw detector module ST03

The signal from the straws is read out on the bottom side only. On the top side, straws are terminated by termination boards. In the middle part of the plane with a physical hole, the signal has to be read out on both sides owing to the disconnection of the straws [14]. The motherboard[33] distributes the high voltage to the straws and acts as an interface to the front end card, which recuperates and amplifies the signal. The front end card also has a time to digital converter incorporated, which is an advantage since it reduces the amount of cabling needed. Other advantages of straw drift tubes are for example:

- Very high resolution in a large area.
- In case of breakdown of one channel, only one channel is lost since it can be disconnected easily without affecting other channels.
- When having a radial symmetry for the electrical field, the resolution is equal for tracks of different angles.

The drift time information can be converted to distance r from the place of primary ionization to the wire by the drift velocity, which is different for every gas. The dependence of r on the drift time t is called RT relation. Plotting in a two-dimensional histogram, the distance r as x-axis and the drift time t as y-axis, a so-called V-plot is obtained [21]. The V shape is caused by the fact that the same drift time could correspond to two different positions in the straw, one on the right side of the wire, the other on the left side of the wire. Due to its characteristic shape the RT relation is also called "V-distribution" [14].

The RT relation is important for data analysis. Therefore, it has to be calibrated. The calibration is performed via fitting of the V-distribution. The fitting line is usually obtained by assuming seven points (on each side of V-distribution) between which a linear interpolation is used [20]. Since the alignment of the detector may change (e.g. due to the movement of the detector) or another problem may occur, it is convenient to validate the calibration periodically. The start of data taking for the 2021 run is scheduled for August and the intended end of the run is in October [74]. Before the start of 2021 run, preliminary calibrations are needed. These calibrations are usually taken from the previous run. Therefore, I verified calibration for the latest (2018) run and I analysed the very last run in 2018 i.e. run number 287536[34]. A web-based logbook was developed for COMPASS to keep track of the data taking and the conditions of the experimental setup. The logbook is connected to a MySQL database for the permanent storage and easy searching of the annotations and comments [1]. The link to this logbook is `https://wwwcompass.cern.ch/logbook/?p=runs`.

Several steps were performed to verify the calibration of the Straw detector. After data acquisition, a reconstruction C++ software package called CORAL (COmpass Reconstruction and AnaLysis) was used to reconstruct events and detectors details

[33] The motherboard provides also the possibility of testing the read out system. [21]

[34] Actually the very last run was run number 287537. However, this run had only 43 spills, while normal run has 200 spills.[75]

from raw data[35]. CORAL produced mDST ("mini Data Summary Trees") files as an output. The mDST contain physics data that can then be analyzed using another software - PHAST (PHysics Analysis Software Tool). PHAST software, used along with ROOT data analysis framework, allows further data processing and filtering. PHAST also provides mDST output data stream at the stage of event reconstruction [77]. PHAST is used for accessing reconstructed event information, developing code for physical analysis, processing mDST, and filtering events' sub-samples [78]. Events are selected by PHAST only if they meet the following requirements:

- Track has hits in either next kin (any other coordinate of a detector station) or both upstream and downstream detectors.
- 6 σ wide road – the track width is less than 6 σ (σ is the quadratic sum of detector's intrinsic and tracking resolution).
- Vertexing – studied hit in detector does have a reconstructed track that has origin in the target area.

After PHAST analysis, the RT relations with the calibrations were plotted. They are shown in Fig. 3.6 – 3.11. Each of these figures illustrates six graphs for one double layer. The calibrations are represented with the red line. The upper three graphs marked with the letter "u" show RT relations for the upstream layer of the detector and the bottom three graphs represent the RT relations for downstream "d" layer. The letters a, b, c stand for sections of a straw plane (they were already mentioned as the sections A, B, C).

The shape of the V-distribution provides information about the position resolution of the detector and also about gas properties. When parts of V legs are broad, it means that the resolution is worse.

It is obvious that in the central part b the number of hits is much more higher than in the outer sections a, c. It is caused by the beam intensity, which is higher in the central region [21]. For the outer part a of the U1 double layer (shown in Fig. 3.8), the number of events is unusually low. The causation of this phenomenon is the non-functional large extent of the mentioned area (more precisely two thirds) for this run (for efficiency graph see Appendix 1 - Efficiency graphs, Fig. 3.15). It was caused partly by the failure of the front end card and partly by the high voltage short circuit, which has been a difficulty for many years.

In addition, the efficiency of the detector as a function of position within the straw plane was calculated. The efficiency of the detector is determined by many factors – whether ionizations occur, whether the signal is covered by noise etc.. For example the efficiency for the Y1 double layer of the detector is shown in Fig. 3.12. In this area, the detector worked with sufficient efficiency of at least 94.68 %. The efficiency graphs for the other double layers are given in Appendix 1 - Efficiency graphs.

[35]The role of the CORAL is also Monte Carlo simulation of the response of the tracking detectors (so-called digitization). [76]

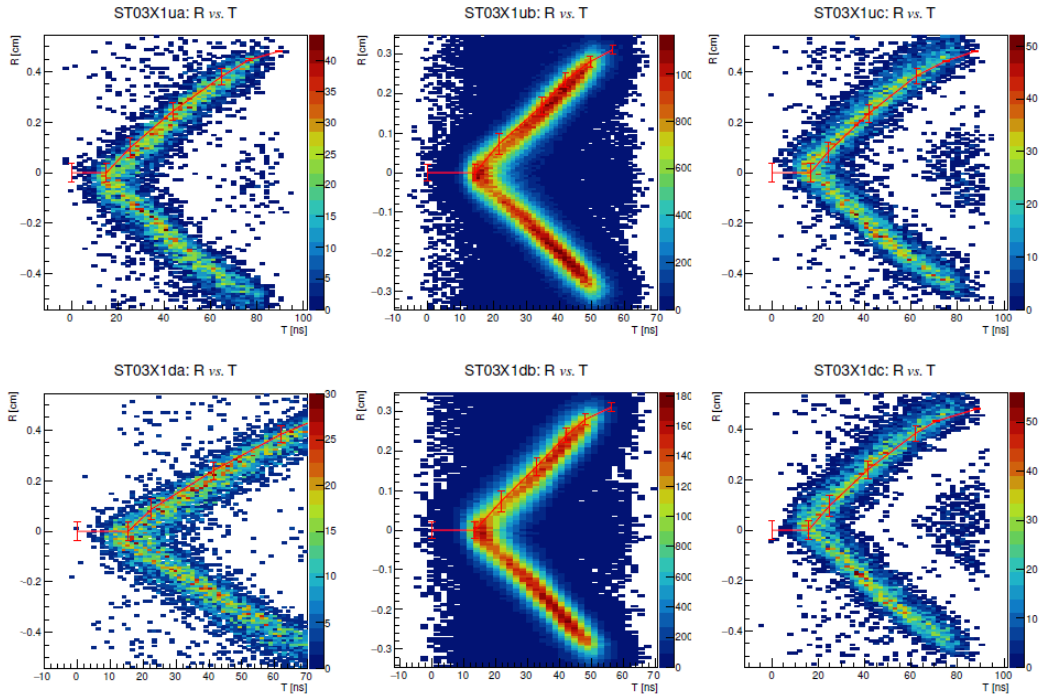

Figure 3.6: RT relation with calibration (represented with the red line) for X1 double layer and run n. 287536

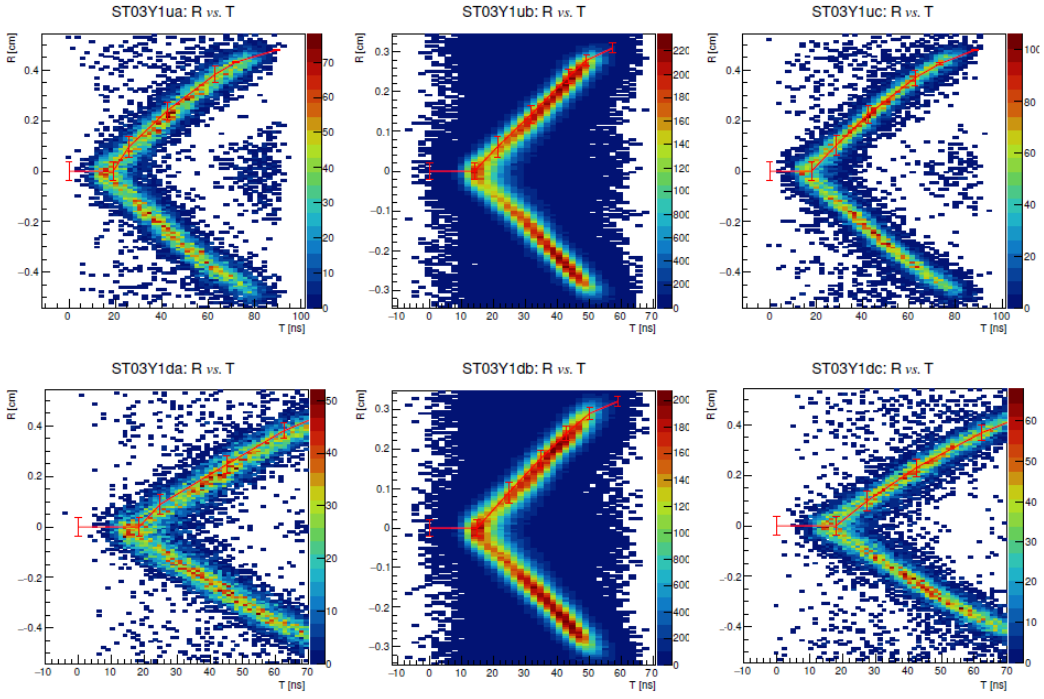

Figure 3.7: RT relation with calibration (represented with the red line) for Y1 double layer and run n. 287536

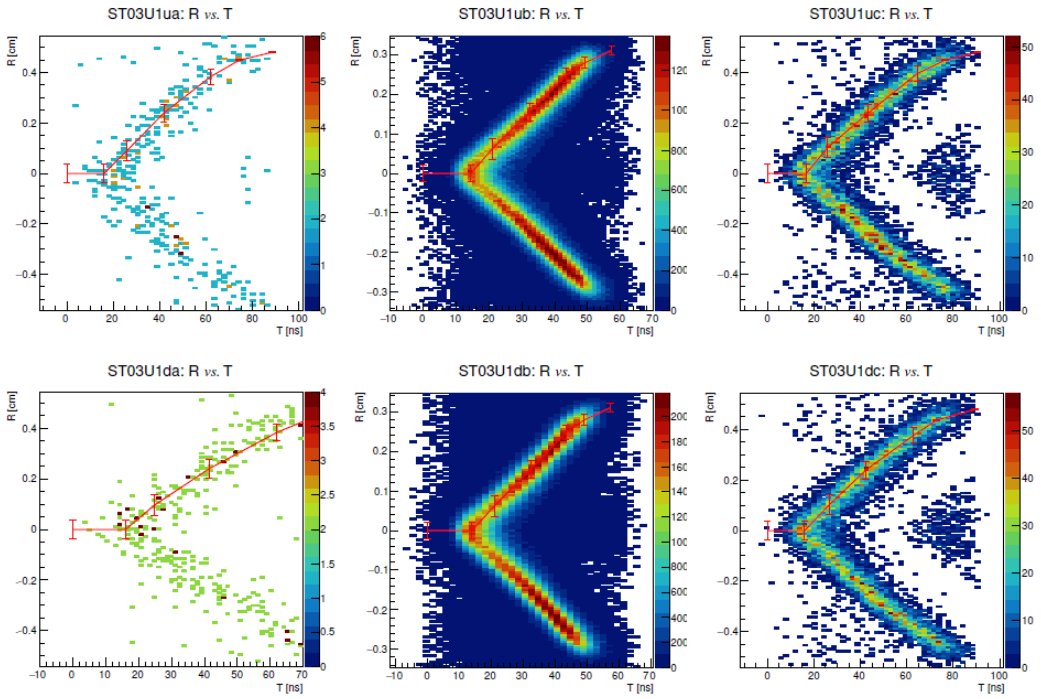

Figure 3.8: RT relation with calibration (represented with the red line) for U1 double layer and run n. 287536

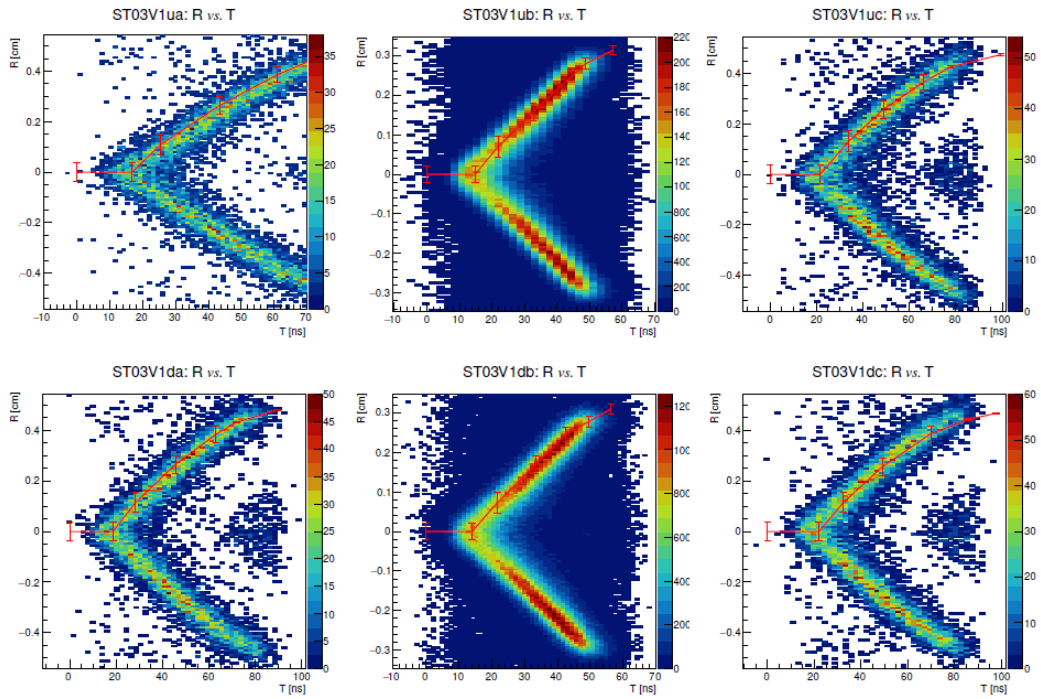

Figure 3.9: RT relation with calibration (represented with the red line) for V1 double layer and run n. 287536

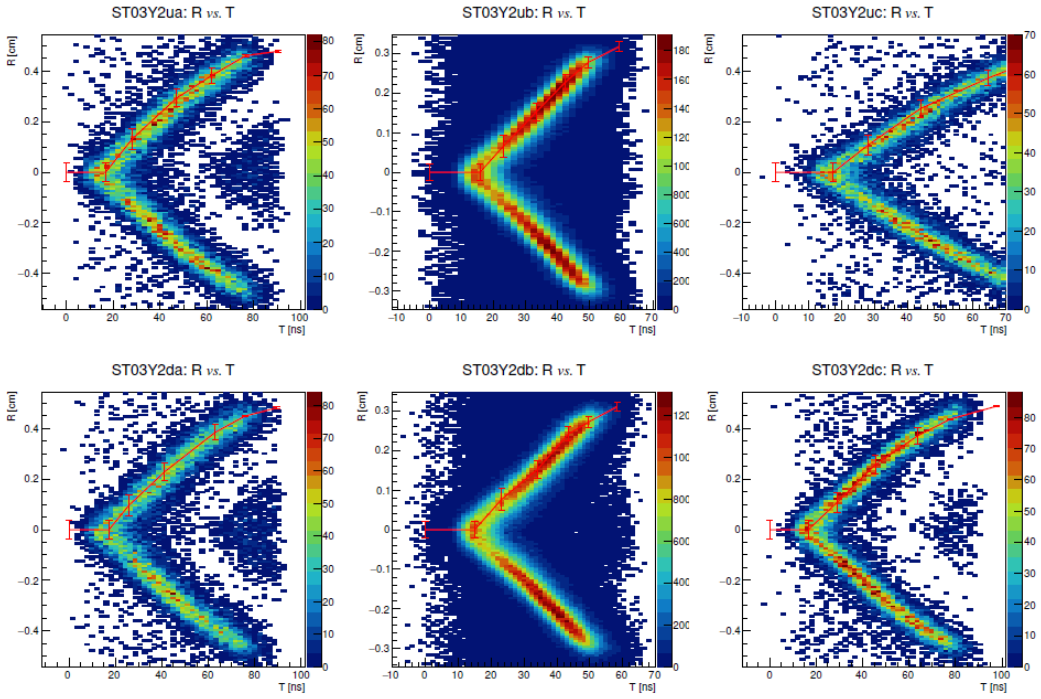

Figure 3.10: RT relation with calibration (represented with the red line) for Y2 double layer and run n. 287536

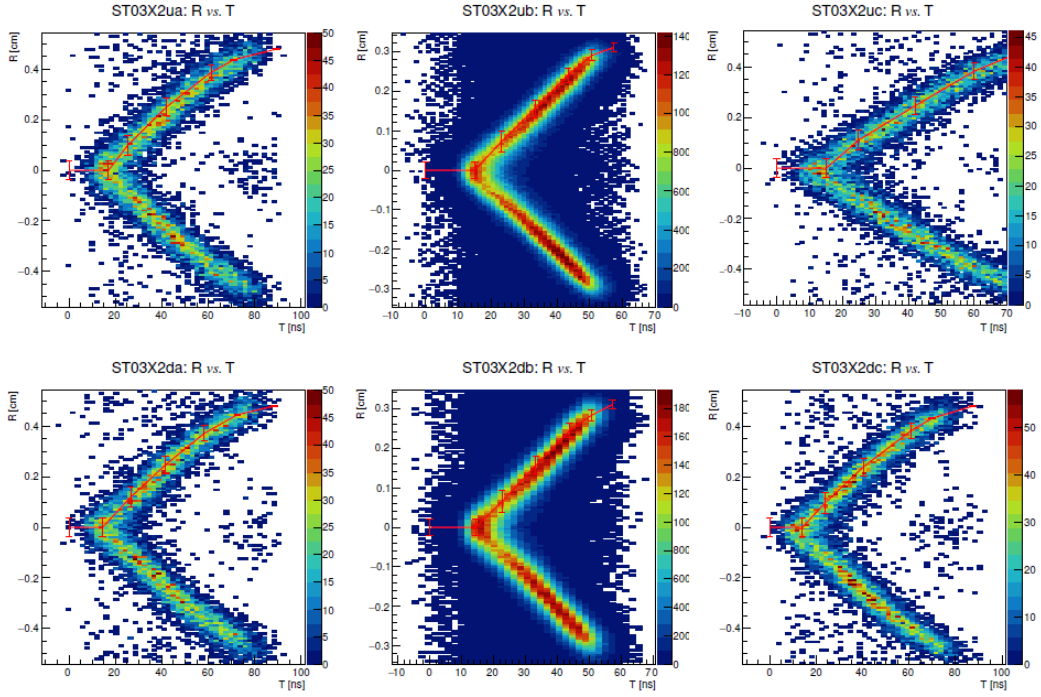

Figure 3.11: RT relation with calibration (represented with the red line) for X2 double layer and run n. 287536

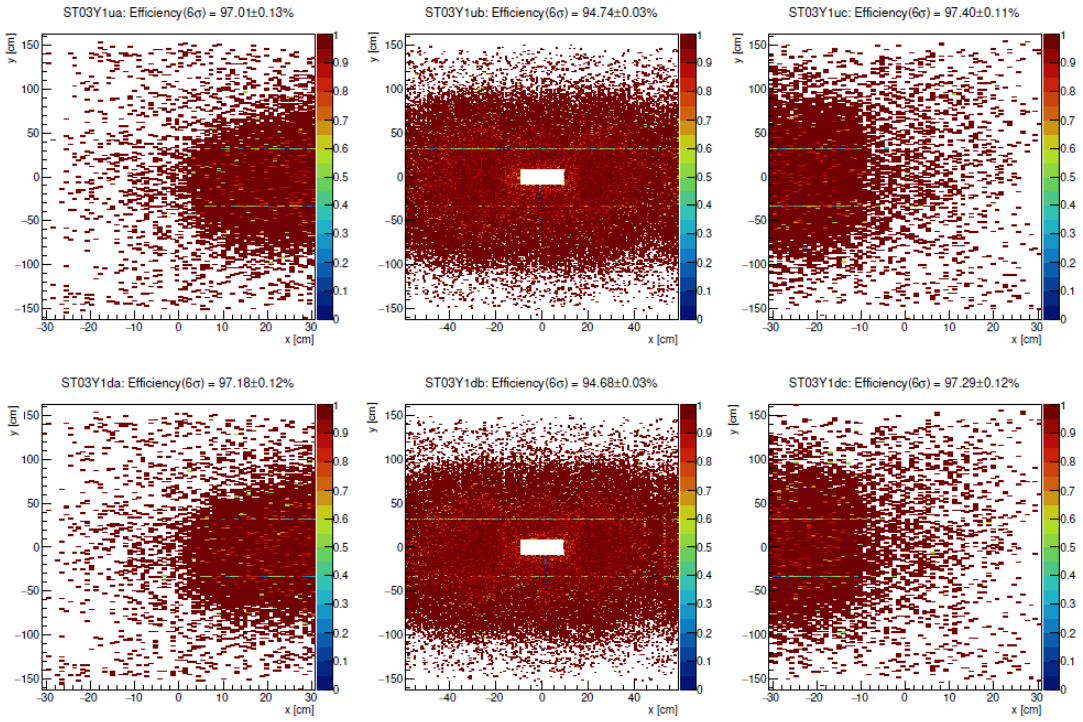

Figure 3.12: The efficiency of the detector for Y1 double layer and run n. 287536

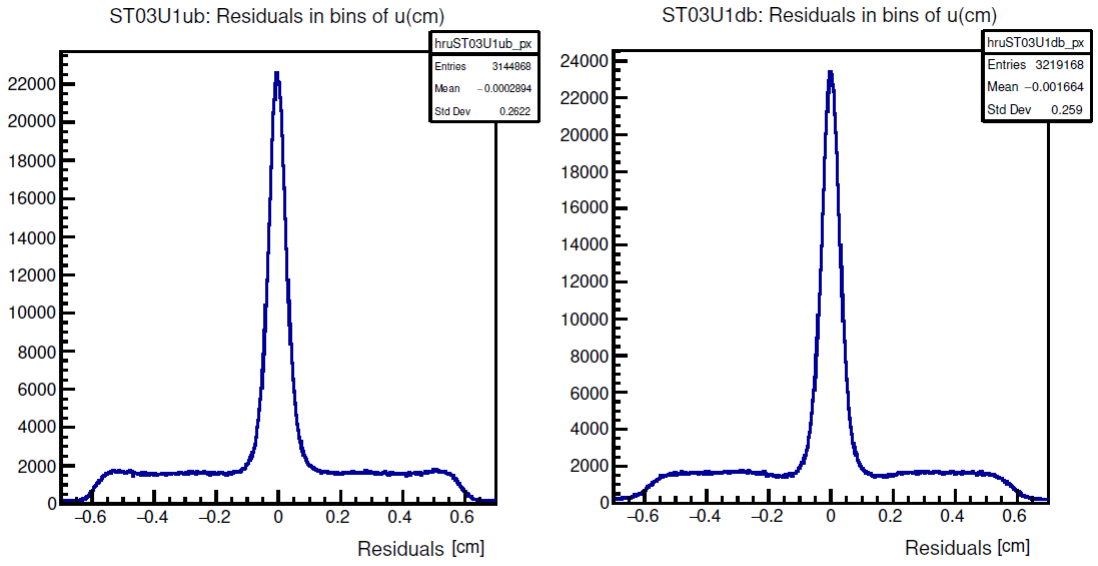

Figure 3.13: Residuals for U1 double layer, section b and run n. 287536

Moreover, the residuals were determined. The residuals are defined as a difference $y - y'$, where y is a measured value in the RT relation and y' is a fitted value (calibration). The difference from fitted value is calculated for each event and the results could be shown either in 2D histograms, or 1D histograms. The 1D histogram is more illustrative. It is obtained by the projection on x-axis. Such a histogram should have one peak ideally. The peak should be centred at zero. If it is not, it means that there is a problem with the calibration or the alignment. The 1D histograms for double

layer U1 and section b are shown in Fig. 3.13 (1D histograms of residuals for the other areas of the detector Straw are shown in Appendix 2 - 1D Histograms of residuals). The fact that the graphs have only one peak indicates that the calibrations and alignment are correct.

The RMS of the peak is also a sign of an accurate calibration. In general, smaller RMS means better calibration and better resolution [14]. For the double layer U1, section b are RMSs -0.0002894 cm for the upstream layer and -0.001664 cm for the downstream layer. These values are very close to zero, which corresponds to the requirements for the correct calibration.

There are few small discrepancies, for example in Fig. 3.6, where RT relations for the double layer of type X1 are shown, in the upstream layer and sections a and c, one can notice that the centre of the V shape is not exactly at zero on the y-axis (r). However, this effect comes from alignment issues (such as wrong pitch, which is the distance between individual wires in straws) and cannot be fixed with re-calibration.

In summary, the plots justify the usage of these calibrations as preliminary for the 2021 run.

Conclusion

The goal of the COMPASS physics program is to study hadron spectroscopy and hadron structure. For exploring of hadron structure in new ways Generalized Parton Distributions (GPDs) have been developed in last decades. The current physics program of the COMPASS experiment is focused on the GPDs. They are researched via measurements of Hard Exclusive Meson Production (HEMP) and Deeply Virtual Compton Scattering (DVCS). These processes are described in this thesis, together with a general summary of the theoretical background. Along with them, other processes related to the COMPASS experiment were introduced.

The wide area of COMPASS experiment intent requires a very adaptable setup allowing measurements with muons as well as hadron beams. This variability is guaranteed by the fact that huge setup elements are mounted on rails, which permits moving some of them at variable distances from the target, using only some of them, or replacing some detectors with detectors of other types. The experimental setup, divided into four sections (beam line section, target area, large angle spectrometer and small angle spectrometer) and spread over a length of 50 m, was described. The setup was built using various technologies. The overview of the detectors used in the COMPASS spectrometer was also given with particular emphasis on the Straw detector and its structure.

One of the main objects of interest of this thesis was the calibration of the RT relation of the tracking detector Straw. It is particularly important for the precise track reconstruction required for the analysis of HEMP and DVCS events. Since the alignment of the detector may change (e.g. due to the movement of the detector) or another problem may occur, it is suitable to validate the calibrations from time to time, especially before the start of the new year of data taking. Before the 2021 run, was necessary to verify whether the calibration used in 2018 is still valid. That was one of the tasks of this thesis. The accuracy of the calibration was tested for the last run of 2018 data taking with an appropriate number of spills. The RT relations were plotted together with detectors efficiency and graphs of residuals. These plots justify the usage of these calibrations as preliminary for the 2021 run.

To guarantee the accurate position of the detector Straw for the 2021 run the results from the survey measurement 2021 were calculated. The positions of six points for each of the six double layers were determined. These points were distributed with respect to the inner structure of the detector. The results of these measurements do not have significant distinctions from the 2018 data. It indicates that there were no intended changes in module arrangement and the detector is in the correct position. These values are saved in detector description file “detectors.dat”, which serves as

the start point of the alignment procedure and is later used for many tasks like reconstruction of particle tracks and Monte Carlo generations.

The COMPASS measurements are provided in the region of kinematic variables unexplored in larger measure by any other experiments. By now, an impressive list of results has been published concerning nucleon structure. The data from last years of data taking are currently analyzed. The COMPASS apparatus has proven to be very versatile. It offers the unique chance to study another large variety of newly opened QCD-related challenges in both hadron spectroscopy and hadron structure in the future. The future of the COMPASS physics program includes measurements of the SIDIS process with the transversely polarized deuteron target, the proton radius measurements, spectroscopy of mesons and baryons, and the Drell-Yan process. Some of these will happen within the AMBER (Apparatus for Meson and Baryon Experimental Research) experiment, the next-generation successor of the COMPASS experiment.

Bibliography

[1] ABBON, P. et al. The COMPASS experiment at CERN. *Nuclear Instruments and Methods in Physics Research Section A.* 2007, 577, 455-518. ISSN 01689002. DOI: 10.1016/j.nima.2007.03.026.

[2] *The CERN accelerator complex* [online]. [Cited on 14th March 2021]. Available at: `https://panoramas-outreach.cern.ch/static/media/cern-complex.51240094.jpg`

[3] MATOUŠEK, Jan.*COMPASS Drell Yan web* [online]. TWiki, published on 23th February 2018 [cited on 14th March 2021]. Available at: `https://twiki.cern.ch/twiki/bin/viewauth/Compass/Drell_Yan/Figures`

[4] WOLBEEK, Johannes ter. *Azimuthal asymmetries in hard exclusive meson muoproduction off transversely polarized protons.* Freiburg im Breisgau, 2015. PhD thesis. Albert - Ludwigs - Universität. Fakultät für Mathematik und Physik. DOI: 10.6094/UNIFR/10172.

[5] ABBON, P. et al. The COMPASS setup for physics with hadron beams. *Nuclear Instruments and Methods in Physics Research Section A.* 2015, 779, 69-115. ISSN 01689002. DOI: 10.1016/j.nima.2015.01.035.

[6] *The M2 beam line for COMPASS* [online]. [Cited on 18th March 2021]. Available at: `http://sba.web.cern.ch/sba/BeamsAndAreas/M2/M2-OperatorCourse.pdf`

[7] HOHENESCHE, Nicolas. *Measurement of Hadron Multiplicities in Deep Inelastic Muon-Nusleon Scattering.* Mainz, 2015. PhD thesis. Johannes Gutenberg - Universität. Fachbereich Physik, Mathematik und Informatik.

[8] ZYLA, P. A. et al. (Particle Data Group). Review of Particle Physics. *Progress of Theoretical and Experimental Physics.* 2020, 2020(8). ISSN 2050-3911. DOI: 10.1093/ptep/ptaa104.

[9] LEBERIG, M., GATIGNON, L. *The M2 Beam Line* [online]. Published in July 2004 [cited on 23th March 2021]. Available at: `https://wwwcompass.cern.ch/compass/open_meetings/pre_villars_040702/Leberig_02-07-04.pdf`

[10] JASINSKI, Prometeusz. *The selection of incoming Kaons in the high energetic hadron beam of the COMPASS - experiment* [online]. Published in 2009 [cited on 29th March 2021].Available at: `https://wwwcompass.cern.ch/compass/publications/talks/t2009/jasinski_prague09.pdf`

[11] ZIEMBICKI, Marcin. *Status of CEDAR Upgrade Project in COMPASS* [online]. Published on 24th July 2018 [cited on 1st April 2021]. Available at: https://indico.cern.ch/event/745422/contributions/3085580/attachments/1692102/2722818/2018-07-24_CEDAR-EATM.pdf

[12] PEŠEK, Michael. *Pion-induced polarized Drell-Yan process at COMPASS*. Prague, 2020. PhD thesis. Charles University. Faculty of Mathematics and Physics.

[13] COMPASS Collaboration. *COMPASS-II proposal*. 2010. CERN-SPSC-2010-014 SPSC-P340.

[14] JURÁŠKOVÁ, Karolína. *Calibration of Straw detector for studies of DVCS process at COMPASS experiment*. Prague, 2017. Master's thesis. Czech technical university Prague. Faculty of Nuclear Sciences and Physical Engineering.

[15] CHATTERJEE, Chandradoy. *Performance study of the RICH at COMPASS experiment for hadron identification in SIDIS physics*. Trieste, 2020. PhD thesis. Università Degli Studi Di Trieste. Department of Physics.

[16] D'HOSE, Nicole. *2016 RUN COMPASS* [online]. Published on 24th November 2016 [cited on 2nd April 2021]. Available at: https://wwwcompass.cern.ch/compass/gpd/meetings/2018/20161124_NdH_CM_Nov_CERN.pdf

[17] ALBRECHT, E. et al. COMPASS RICH-1. *Nuclear Instruments and Methods in Physics Research Section A*. 2002, 478, 340-343. ISSN 01689002.

[18] SCHMIDT, Katharina. *Transverse target spin asymmetries in exclusive vector meson muoproduction*. Freiburg im Breisgau, 2014. PhD thesis. Albert-Ludwigs-Universität. Fakultät für Mathematik und Physik.

[19] BERNET, C. et al. The COMPASS trigger system for muon scattering. *Nuclear Instruments and Methods in Physics Research Section A*. 2005, 550, 217-240. ISSN 01689002. DOI: 10.1016/j.nima.2005.05.043.

[20] BYCHKOV, V. N. et al. The large size straw drift chambers of the COMPASS experiment at CERN. *Nuclear Instruments and Methods in Physics Research Section A*. 2006, 556, 66-79. ISSN 01689002. DOI: 10.1016/j.nima.2005.10.026.

[21] SANS MERCE, Marta. *Development of drift chambers and physics simulations for the COMPASS experiment*. München, 2001. PhD thesis. Ludwig-Maximilians-Universität. Fakultät für Physik.

[22] ZVYAGIN, Alexander. *STRAW gas studies*. 2014

[23] KUČERA, Vít. *Zkoumání struktury protonu v e-p interakcích*. Prague, 2010. Bachelor's thesis, Charles University. Faculty of Mathematics and Physics.

[24] HOFSTADTER, Robert. Electron Scattering and Nuclear Structure. *Reviews of Modern Physics*. 1956, 102. ISSN 0034-6861. DOI: 10.1103/RevModPhys.28.214.

[25] ŽÁČEK, Josef. *Úvod do fyziky elementárních částic*. Prague: Karolinum, 2005. ISBN 978-80-246-1109-9

[26] HOŘEJŠÍ, Jiří. *Historie standardního modelu mikrosvěta*. Prague, Charles University. Institute of Particle and Nuclear Physics Faculty of Mathematics and Physics.

[27] BERTA, Peter. *Zkoumání kvark-gluonové struktury elementárních částic*. Prague, 2010. Bachelor's thesis. Charles University. Faculty of Mathematics and Physics.

[28] BURTIN, Etienne. *Study of nucleon structure through scattering of leptons*. 2010. Habilitation thesis.

[29] FELTESSE, Joël. *Introduction to Parton Distribution Functions* [online]. Scholarpedia, published in 2010 [cited on 10th April 2021]. Available at: `http://www.scholarpedia.org/article/Introduction_to_Parton_Distribution_Functions`. DOI: 10.4249/scholarpedia.10160.

[30] BURKARDT, M., MILLER, C. A., NOWAK, W. D. Spin-polarized high-energy scattering of charged leptons on nucleons. *Reports on Progress in Physics*. 2009, ISSN 0034-4885.

[31] SALAM, Gavin. *QCD (for LHC)Lecture 2: Parton Distribution Functions* [online]. Bautzen, published in June 2009 [cited on 15th April 2021]. Available at: `https://gsalam.web.cern.ch/gsalam/repository/talks/2009-Bautzen-lecture2.pdf`

[32] HALZEN, Francis, MARTIN, Alan D. *Quarks and Leptons: An Introductory Course in Modern Particle Physics*. JOHN WILEY SONS, 1984. ISBN 0-471-88741-2

[33] FEYNMAN, Richard. P. Very high-energy collisions of hadrons. *Physical Review Letters*. 1969. ISSN 0031-9007. DOI: 10.1103/physrevlett.23.1415.

[34] GRIFFITHS, David. *Introduction to Elementary Particles*. Weinheim: WILEY-VCH, 2008. ISBN 9780471603863. DOI: 10.1002/9783527618460.

[35] MCNULTY WALSH, Karen. *Physicists zoom in on gluons' contribution to proton spin* [online]. Published on 16th February 2016 [cited on 1st May 2021]. Available at: `https://phys.org/news/2016-02-physicists-gluons-contribution-proton.html`

[36] GAO, Haiyan. *Review on Nucleon Electromagnetic Form Factors* [online]. Published on 11th October 2010 [cited on 2nd May 2021]. Available at: `https://wwwcompass.cern.ch/compass/gpd/Conf_Trento_2010/2nd/Gao_nucleon-FF-ECT2010.pdf`

[37] SLOAN, Terry. *History of the European Muon Collaboration (EMC)*. Geneva: CERN, 2019. ISBN 978-92-9083-546-2. DOI: 10.23731/CYRM-2019-005.

[38] DIEHL, Markus. *Introduction to Generalized Parton Distributions*. Aachen, RWTH Aachen. Institut für Theoretische Physik.

[39] MÜLLER, D., ROBASCHIK, D., GEYER, B. Wave Functions, Evolution Equations andEvolution Kernels from Light-Ray Operators of QCD. *Progress of Physics*. 1994, 42(2):101, ISSN 1521-3978. DOI: 10.1002/prop.2190420202.

[40] RADYUSHKIN, A. V. Nonforward parton distributions. *Physical Review D*. 1997, 56(9):5524. ISSN 2470-0010. DOI: 10.1103/PhysRevD.56.5524.

[41] JI, Xiangdong. Gauge-Invariant Decomposition of Nucleon Spin. *Physical Review Letters*. 1997, 78(4):610. ISSN 0031-9007. DOI: 10.1103/PhysRevLett.78.610.

[42] GARÇON, Michel. An introduction to the Generalized Parton Distributions. *The European Physical Journal A*. 2003, 18, 389–394. ISSN 1434-6001. DOI: 10.1140/epja/i2002-10242-2.

[43] DIEHL, Markus. Generalized Parton Distributions. *Physics Reports*. 2003, 388, 41-277. ISSN 0370-1573. DOI: 10.1016/j.physrep.2003.08.002.

[44] CLOSE, Frank, DONNACHIE, Sandy, SHAW, Graham. *Electromagnetic Interactions and Hadronic Structure*. Cambridge University Press, 2007. ISBN 9780511534928. DOI: 10.1017/CBO9780511534928.

[45] GOEKE, K., POLYAKOV M. V., VANDERHAEGHEN, M. Hard exclusive reactions and the structure of hadrons. Progress in Particle and Nuclear Physics. *Progress in Particle and Nuclear Physic*.2001, 47(2), 401-515. ISSN 0146-6410. DOI: 10.1016/S0146-6410(01)00158-2.

[46] SCHOPFERER, Sebastian. *An FPGA-based Trigger Processorfor a Measurement ofDeeply Virtual Compton Scatteringat the COMPASS-II Experiment*. Freiburg im Breisgau, 2013. PhD thesis. Albert-Ludwigs-Universität. Fakultät für Mathematik und Physik.

[47] *COMPASS, COmmon Muon Proton Apparatus for Structure and Spectroscopy* [online]. Last revision on 9th July 2021 [cited on 11th July 2021]. Available at: `https://wwwcompass.cern.ch/`

[48] ANDRIEUX, Vincent. et al. *COMPASS physics program: present and future*. 2014

[49] COMPASS Collaboration, PNPI. *d-Quark Transversity and Proton Radius - Addendum to the COMPASS-II Proposal*. 2018. CERN-SPSC-2017-034 SPSC-P-340-ADD-1.

[50] *AMBER, A new QCD facility at the M2 beam line of the CERN SPS* [online]. [Cited on 14th May 2021]. Available at: `https://nqf-m2.web.cern.ch/`

[51] GILMAN, R. et al. A Detailed Study of Semi-Inclusive Deep-Inelastic Pion Productions on Unpolarized Proton and Deuteron Targets with the CLAS12 Detector. *A letter to intent to jefferson lab PAC32.*.

[52] MATOUŠEK, Jan. Nucleon Spin Structure Studies at COMPASS. *WDS'14 Proceedings of Contributed Papers - Physics*. Prague: Matfyzpress, 2014, 193–198. ISBN 978-80-7378-276-4

[53] PEŠEK, M. Pion-induced Polarized Drell-Yan Process at COMPASS. *WDS'15 Proceedings of Contributed Papers - Physics*. Prague: Matfyzpress, 2015, 128–131. ISBN 978-80-7378-311-2

[54] FRANCO, Celso on behalf of the COMPASS collaboration. *Polarized Drell-Yan results from COMPASS*. 2018

[55] NOCERA, Emanuele, R. *Fragmentation and Parton Distribution Functions* [online]. Published on 6th September 2016 [cited on 4th June 2021]. Available at: `http://nnpdf.mi.infn.it/wp-content/uploads/2017/10/NOCERA_IWHSS2016.pdf`

[56] D'HOSE, Nicole. *COMPASS-II: a Facility to study QCD* [online]. Published on 2nd July 2013 [cited on 5th June 2021]. Available at: `https://wwwcompass.cern.ch/compass/gpd/NdH_COMPASS-II_China_4web.pdf`

[57] HUBER, Stefan on behalf of the COMPASS collaboration. *Measurement of the Pion Polarizability at COMPASS*. 2014

[58] GUSKOV, A. The Primakoff reaction study for pion polarizability measurement at COMPASS. *Physics of Particles and Nuclei Letters*. 2010, 7(3), 192-200. ISSN 1547-4771. DOI: 10.1134/S1547477110030052.

[59] LANDGRAF, Steffen. *Luminosity Calculation of the COMPASS Experiment using the F_2 Structure Function*. Freiburg im Breisgau, 2014. Master's thesis. Albert-Ludwigs-Universität.

[60] ALICE Collaboration. π^0 and η meson production in proton-proton collision at $\sqrt{s}$=8 TeV. *The European Physical Journal C* . 2018, 263. ISSN 1434-6052. CERN-EP-2017-2016. DOI: 10.1140/epjc/s10052-018-5612-8.

[61] GORZELLIK, Matthias. *Cross-section measurement of exclusive π^0 muoproduction and filmware design for an FPGA-based detector readout*. Dissertation, Freiburg im Breisgau, 2018. PhD thesis. Albert-Ludwigs-Universität Freiburg. Fakultät für Mathematik und Physik.

[62] LIN, Po-Ju. on behalf of the COMPASS collaboration. GDP measurements at COMPASS. *Hadron Spectroscopy and Structure*. 2019, 586-591. ISBN 978-981-121-931-3. DOI: 10.1142/97898112193130100.

[63] COMPASS Collaboration. Measurement of the cross section for hard exclusive π^0 muoproduction on the proton *Physics Letters B*. 2020, 805. ISSN 0370-2693. CERN-EP-2019-049. DOI: 10.1016/j.physletb.2020.135454.

[64] GOLOSKOKOV, S. V., KROLL, P. Transversity in hard exclusive electroproduction of pseudoscalar mesons. *The European Physical Journal A*. 2011, 112. ISSN 1434-6001. DOI: 10.1140/epja/i2011-11112-6.

[65] GOLOSKOKOV, S. V., KROLL, P. Private communications. *Measurement of the cross section for hard exclusive π^0 muoproduction on the proton*. 2016

[66] COMPASS Collaboration. Spin density matrix elements in exclusive ω meson muoproduction *The European Physical Journal C*. 2021, 126. ISSN 1434-6052. DOI: 10.1140/epjc/s10052-020-08740-y.

[67] Augustyniak, W. et al. *Spin density matrix elements in exclusive ρ^0 meson production using the 2012 COMPASS data* [online]. Published on 24th March 2021 [cited on 20th June 2021]. Available at: `https://wwwcompass.cern.ch/compass/results/2021/march_SDMEs_rho0_2012/SDME_release_noteUpdated.pdf`

[68] KUPŚĆ, Andrzej. What is interesting in η and η Meson Decays?. *AIP Conference Proceedings*. 2007, 950, 165-179. ISSN 1551-7616. DOI: 10.1063/1.2819029.

[69] NIKOLITSAS, Konstantinos, BEYNEL, Alexandre, SAINVITU, Pascal. *COMPASS-NA58 Position of detectors for DY run 2018*. 2018

[70] SAINVITU, Pascal, ZEMANEK, Anna. *COMPASS Measurement of the spectrometer detectors*. 2021

[71] AUGSTEN, Kamil. *ST03 Survey - Position Complete Guide*. 2017

[72] RIEDL, Caroline. *Straw dimensions in z* [online]. Published on 8th October 2015 [cited on 6th July 2021]. Available at: `https://uofi.app.box.com/s/bw5f2j60i8mcowbt1r448a4174imwm2h/file/39746816905`

[73] LEO, William R. *Techniques for Nuclear and Particle Physics Experiments*. Berlin: Springer-Verlag Berlin Heidelberg, 1994. ISBN 978-3-642-57920-2. DOI: 10.1007/978-3-642-57920-2.

[74] *COMPASS 2021 run, SIDIS on transversely polarised deuterons* [online]. Published on 23th July 2021 [cited on 28th July 2021]. Available at: `https://wwwcompass.cern.ch/compass/run/run2021/index.php`

[75] *List of all runs* [online]. [Cited on 28th July 2021]. Available at: `https://wwwcompass.cern.ch/logbook/?p=runs`

[76] *Coral* [online]. Published on 13th October 2020 [cited on 28th July 2021]. Available at: `https://twiki.cern.ch/twiki/bin/viewauth/Compass/DataReconstruction/CoralSoftware`

[77] *PHysics Analysis Software Tools* [online]. Published on 11th May 2021 [cited on 28th July 2021]. Available at: `http://ges.home.cern.ch/ges/phast/index.html`

[78] EL-KHOLY, Reham Ibrahim. *Development of the Event Display of the COMPASS experiment*. Dubna, 2017. Joint Institute for Nuclear Research. Dzhelepov Laboratory of Nuclear Problems (DLNP).

Appendix

Appendix contains additional information on the calibration of the detector Straw. The efficiency graphs for X1, U1, V1, Y2, X2 double layers are presented. Furthermore, the 1D histograms of residuals (as they were described in Sec. 3.2) are included.

Appendix 1 - Efficiency graphs

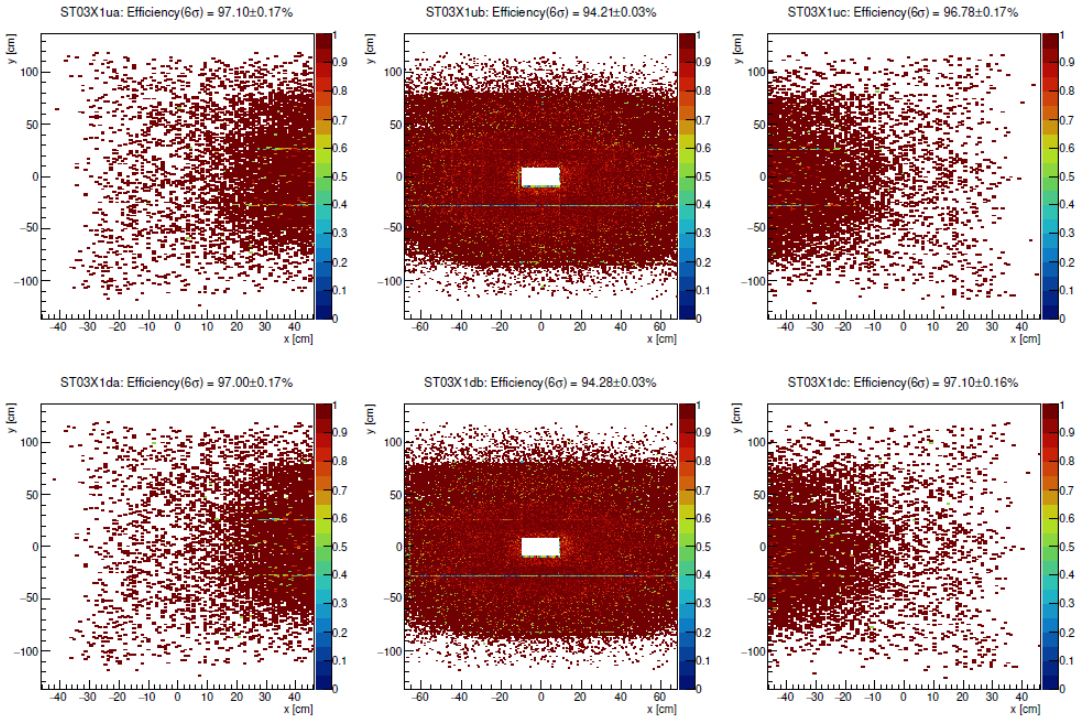

Figure 3.14: The efficiency of the detector for X1 double layer and run n. 287536

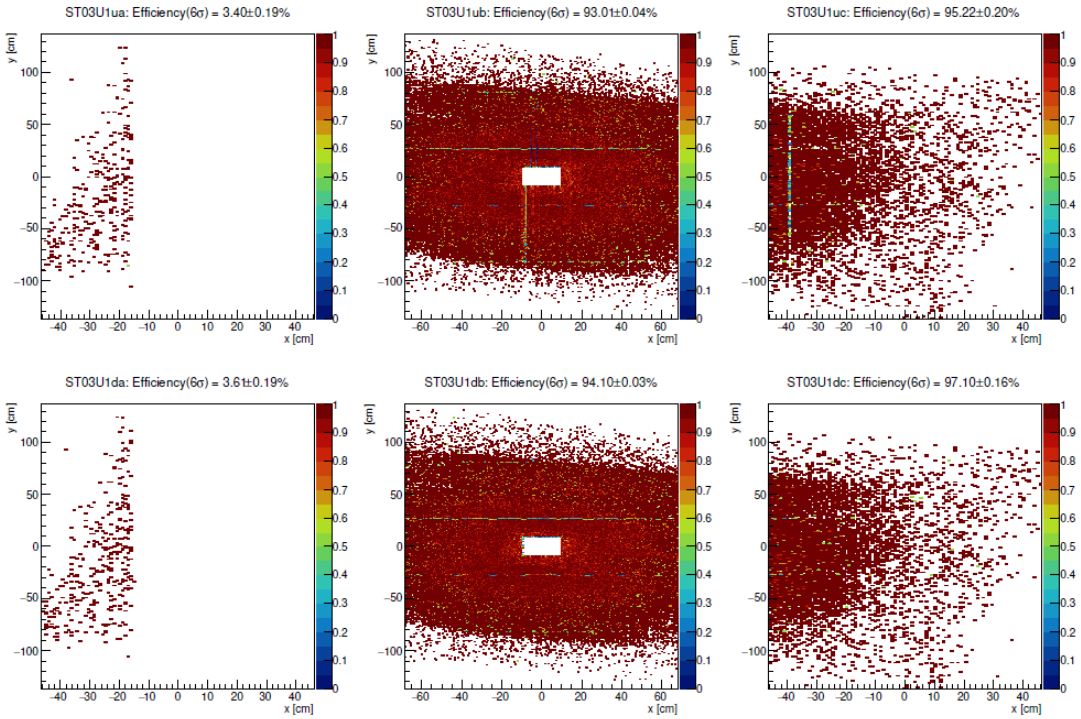

Figure 3.15: The efficiency of the detector for U1 double layer and run n. 287536

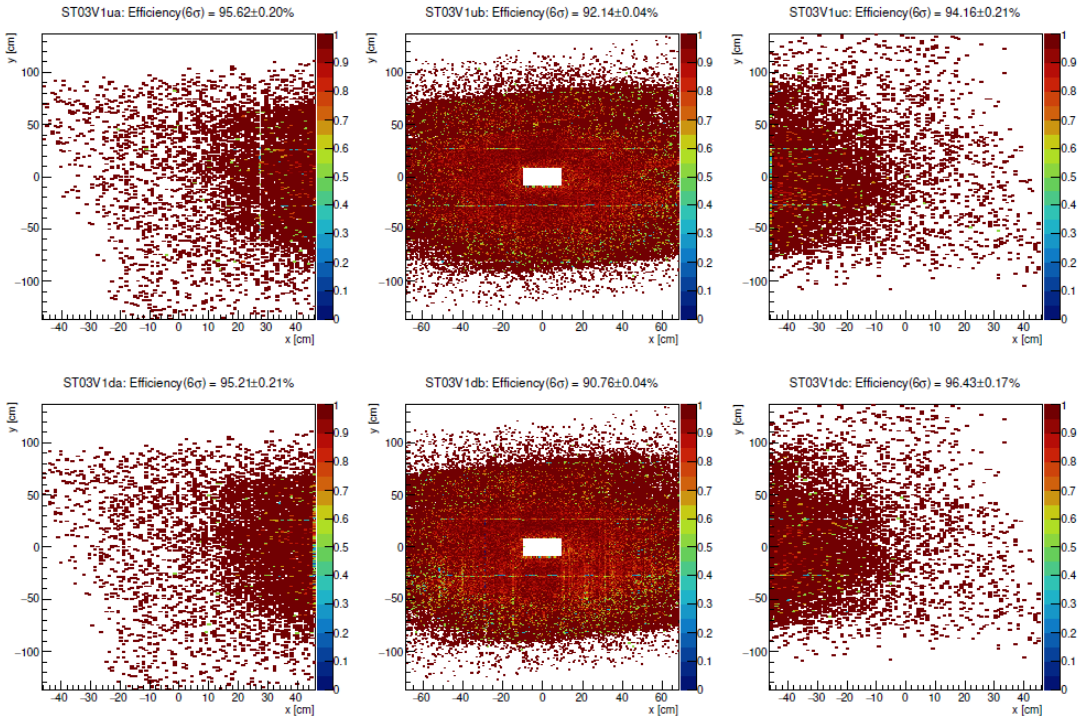

Figure 3.16: The efficiency of the detector for V1 double layer and run n. 287536

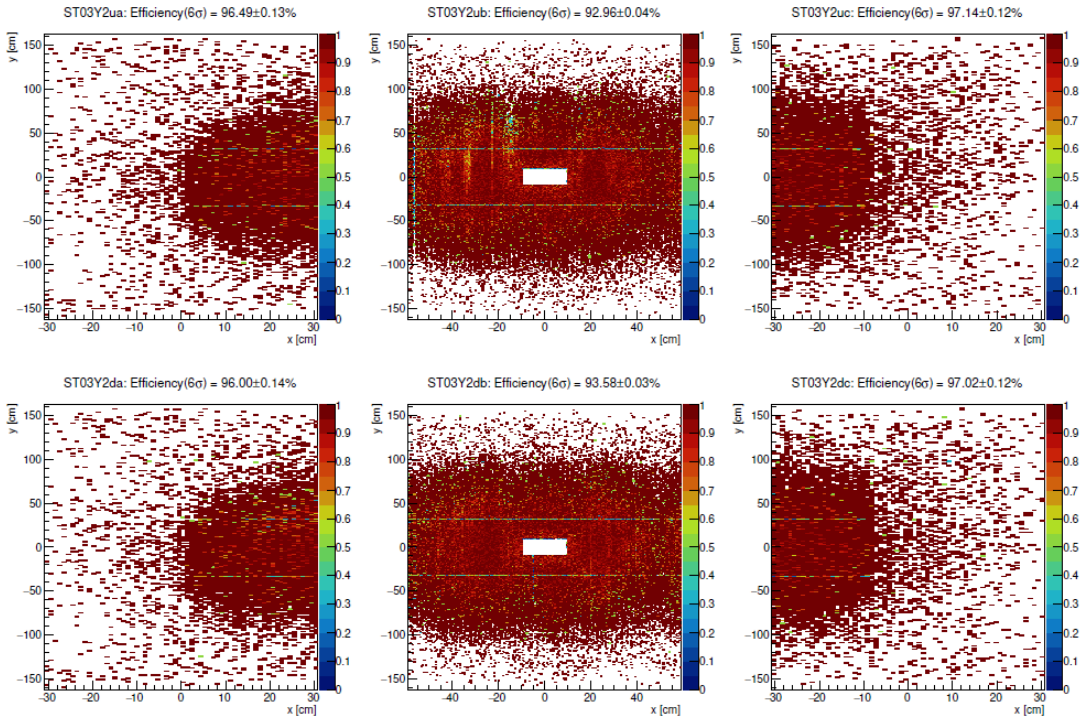

Figure 3.17: The efficiency of the detector for Y2 double layer and run n. 287536

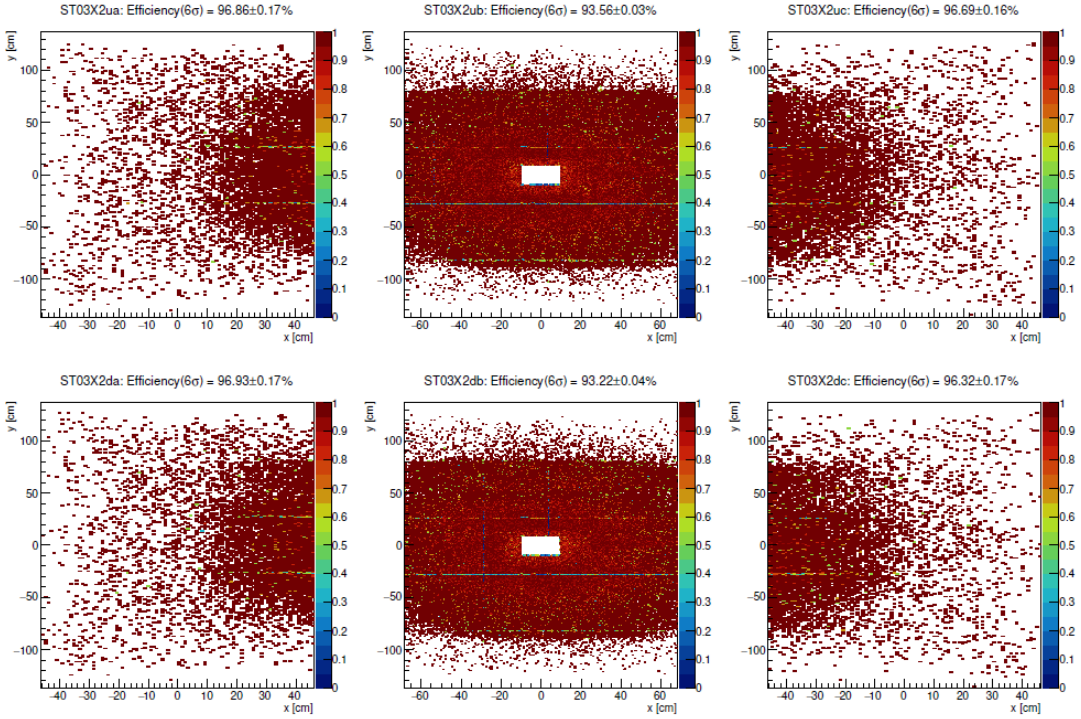

Figure 3.18: The efficiency of the detector for X2 double layer and run n. 287536

Appendix 2 - 1D Histograms of residuals

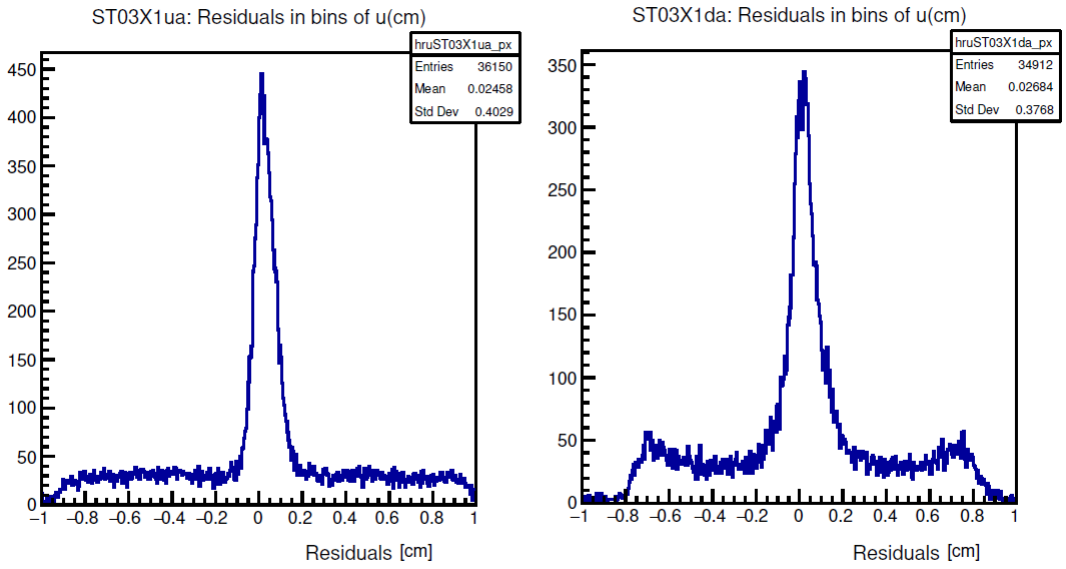

Figure 3.19: Residuals for X1 double layer, section a and run n. 287536

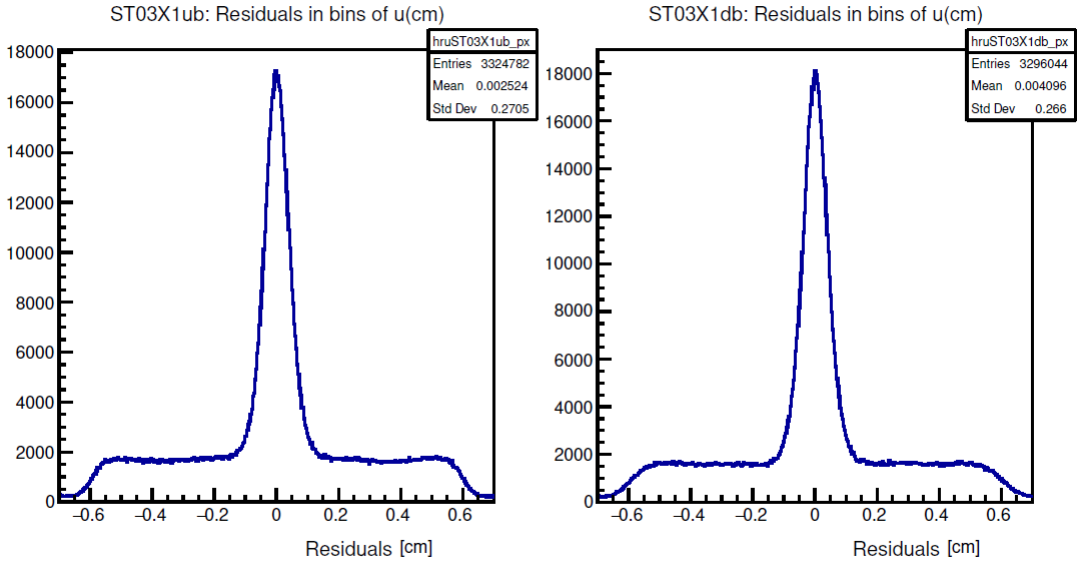

Figure 3.20: Residuals for X1 double layer, section b and run n. 287536

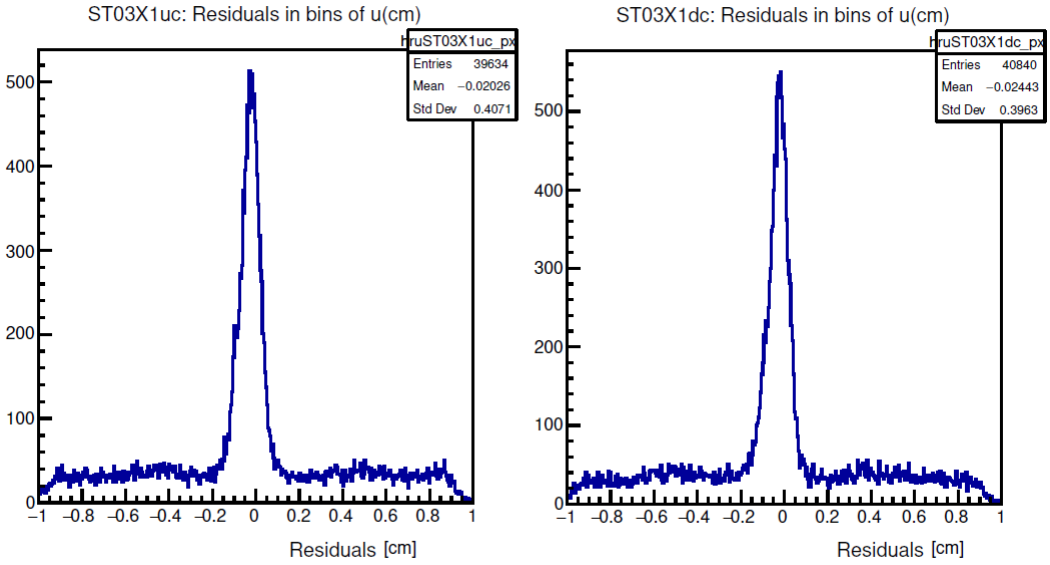

Figure 3.21: Residuals for X1 double layer, section c and run n. 287536

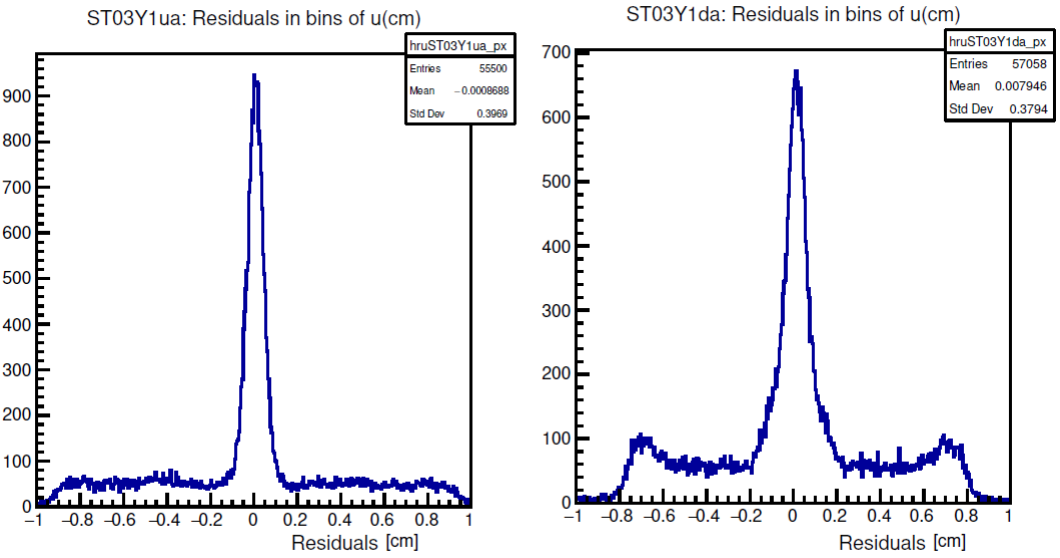

Figure 3.22: Residuals for Y1 double layer, section a and run n. 287536

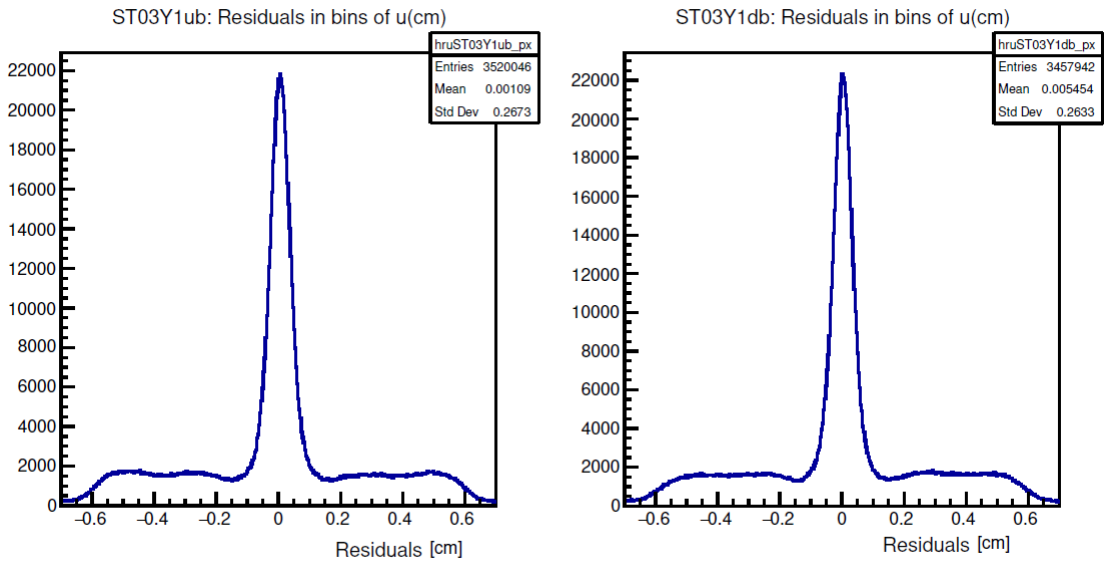

Figure 3.23: Residuals for Y1 double layer, section b and run n. 287536

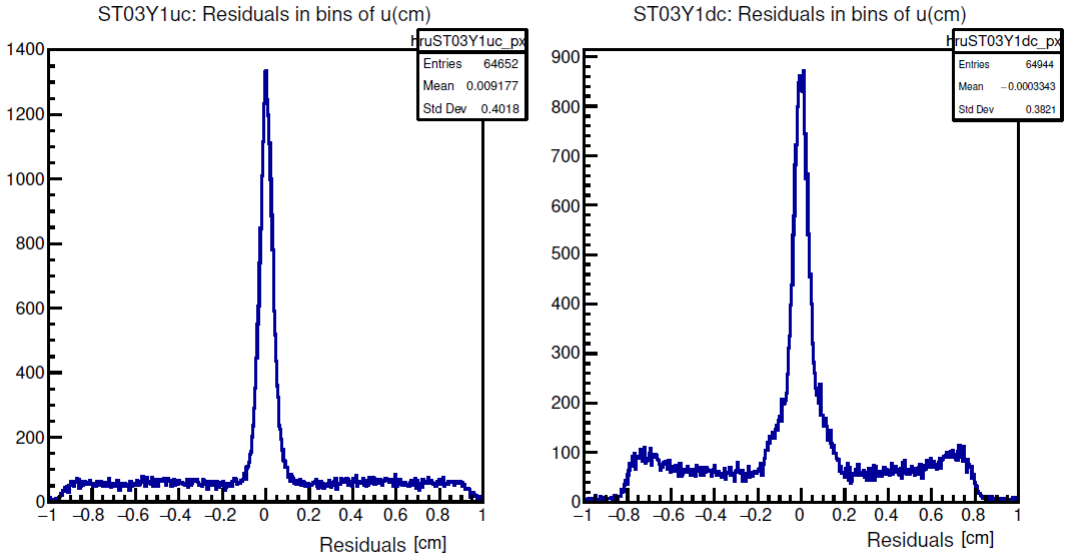

Figure 3.24: Residuals for Y1 double layer, section c and run n. 287536

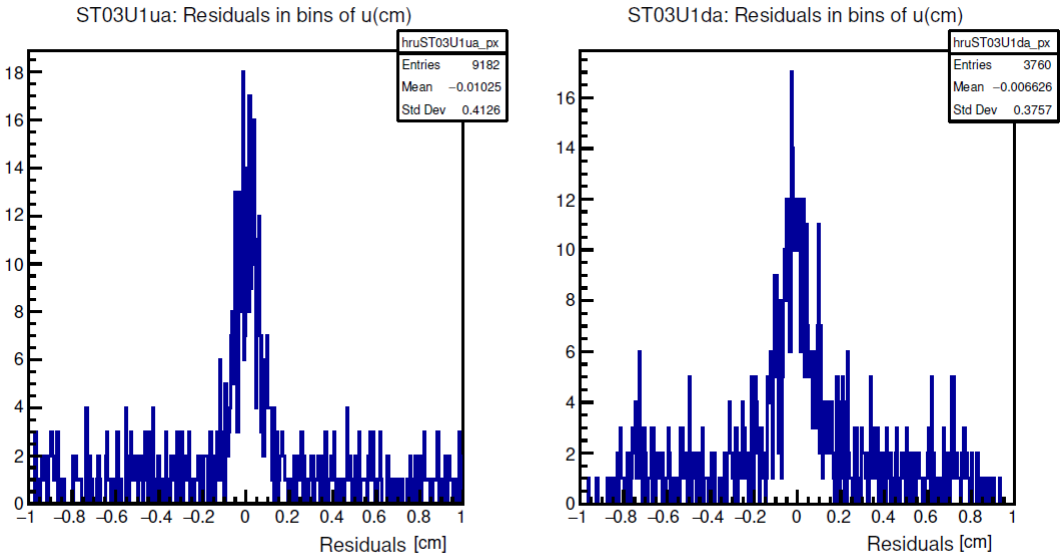

Figure 3.25: Residuals for U1 double layer, section a and run n. 287536

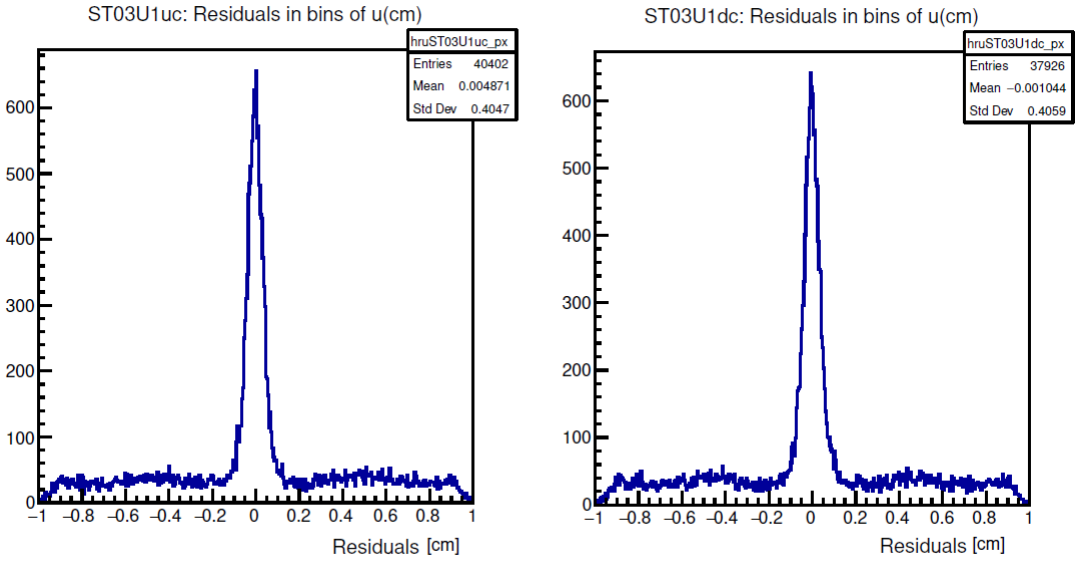

Figure 3.26: Residuals for U1 double layer, section c and run n. 287536

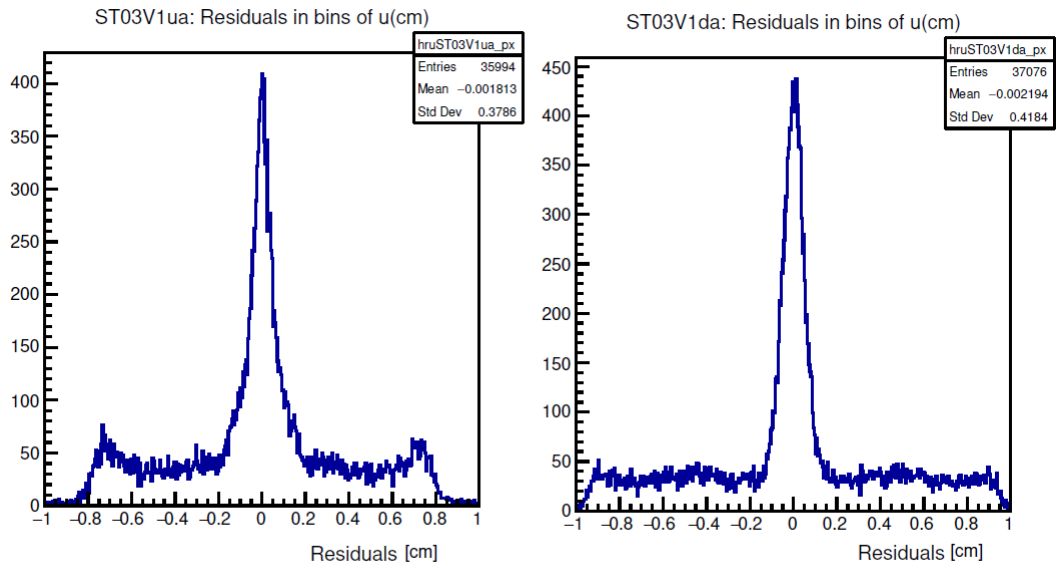

Figure 3.27: Residuals for V1 double layer, section a and run n. 287536

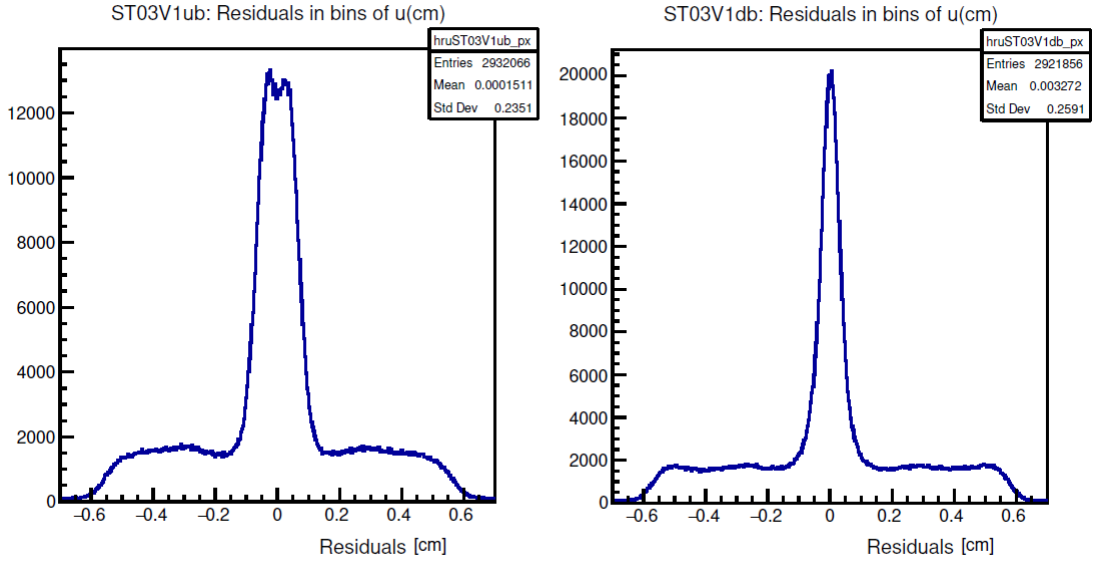

Figure 3.28: Residuals for V1 double layer, section b and run n. 287536

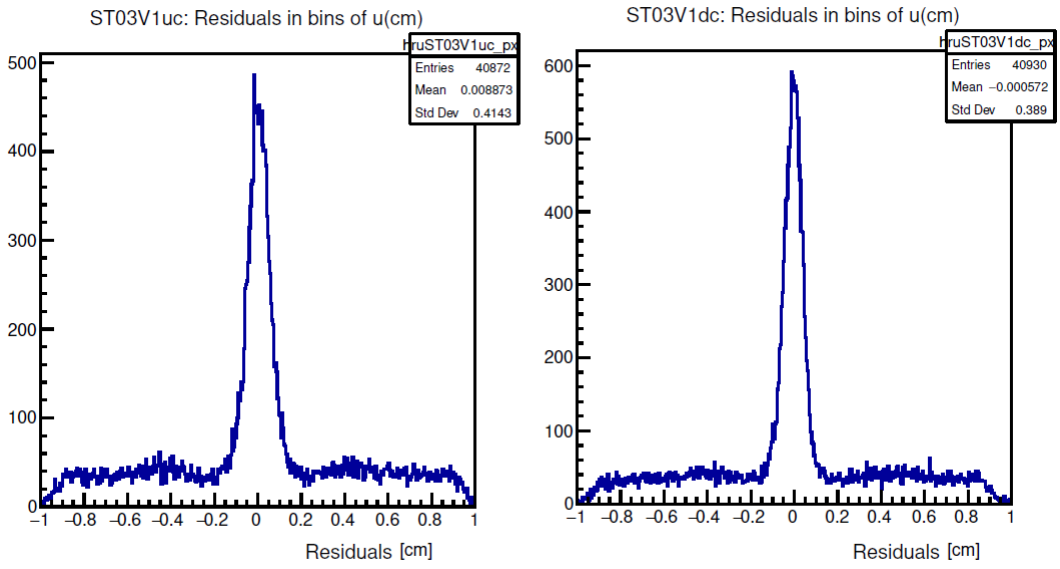

Figure 3.29: Residuals for V1 double layer, section c and run n. 287536

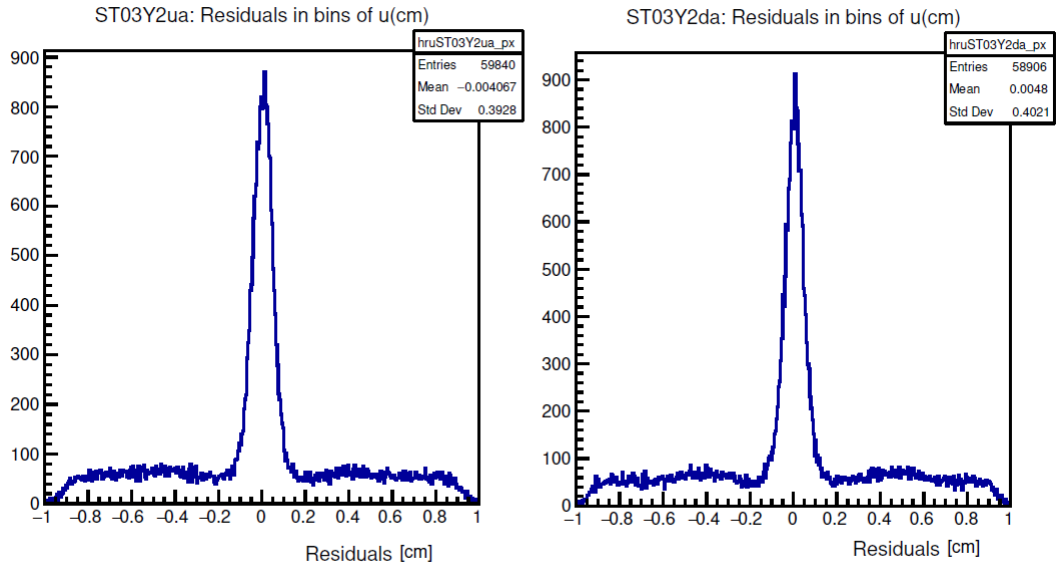

Figure 3.30: Residuals for Y2 double layer, section a and run n. 287536

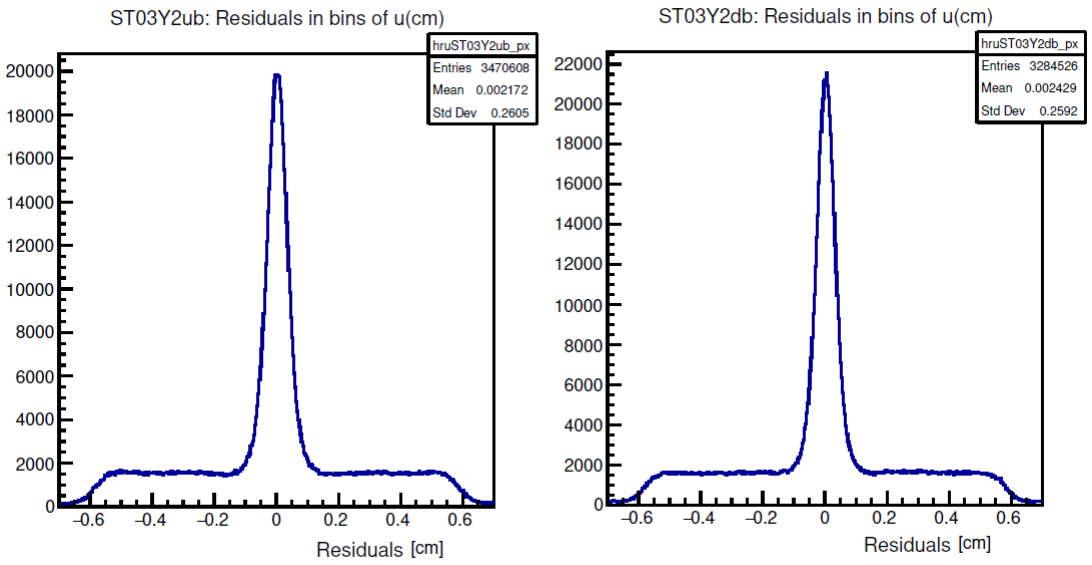

Figure 3.31: Residuals for Y2 double layer, section b and run n. 287536

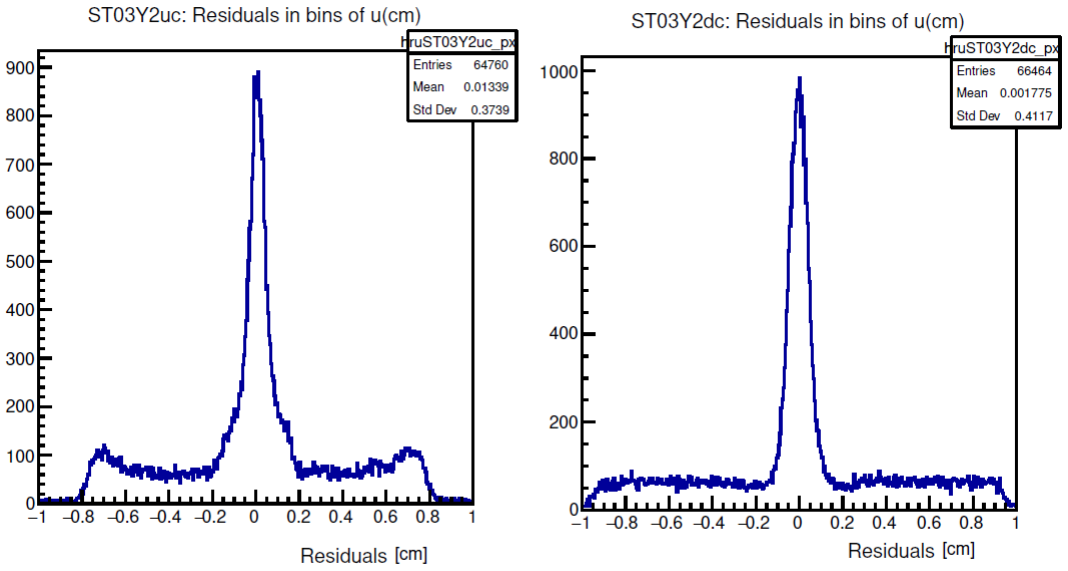

Figure 3.32: Residuals for Y2 double layer, section c and run n. 287536

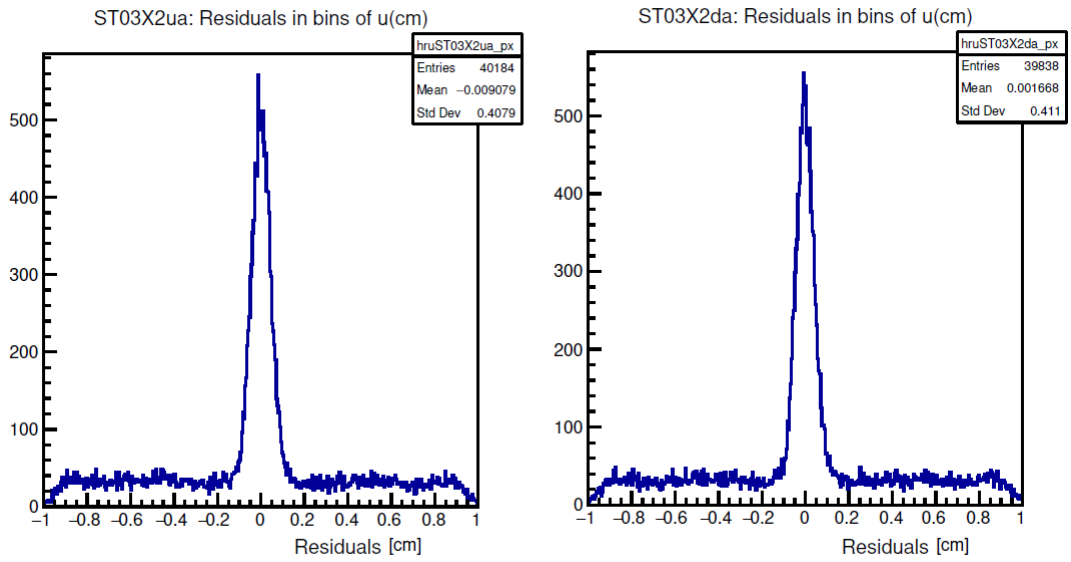

Figure 3.33: Residuals for X2 double layer, section a and run n. 287536

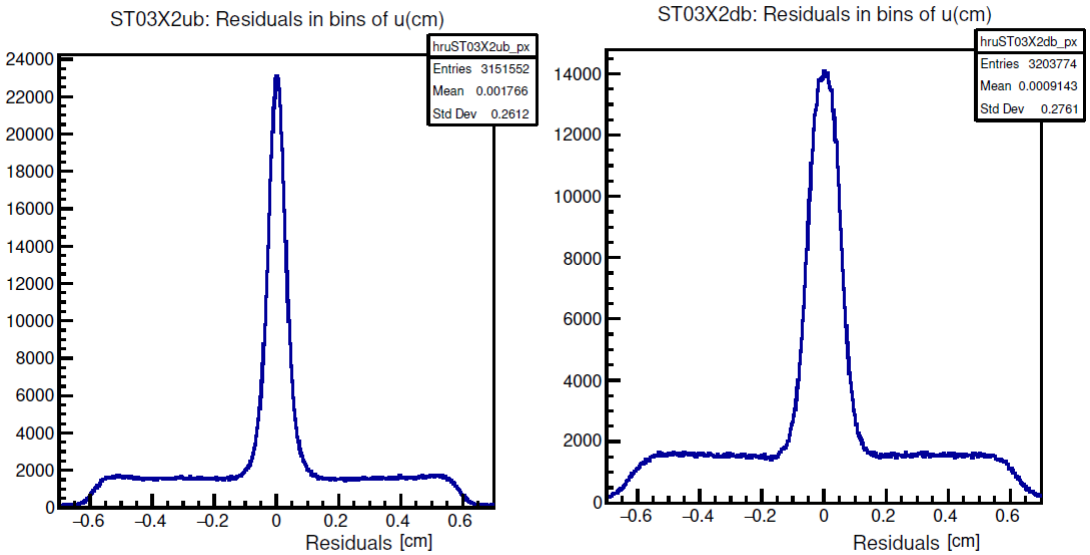

Figure 3.34: Residuals for X2 double layer, section b and run n. 287536

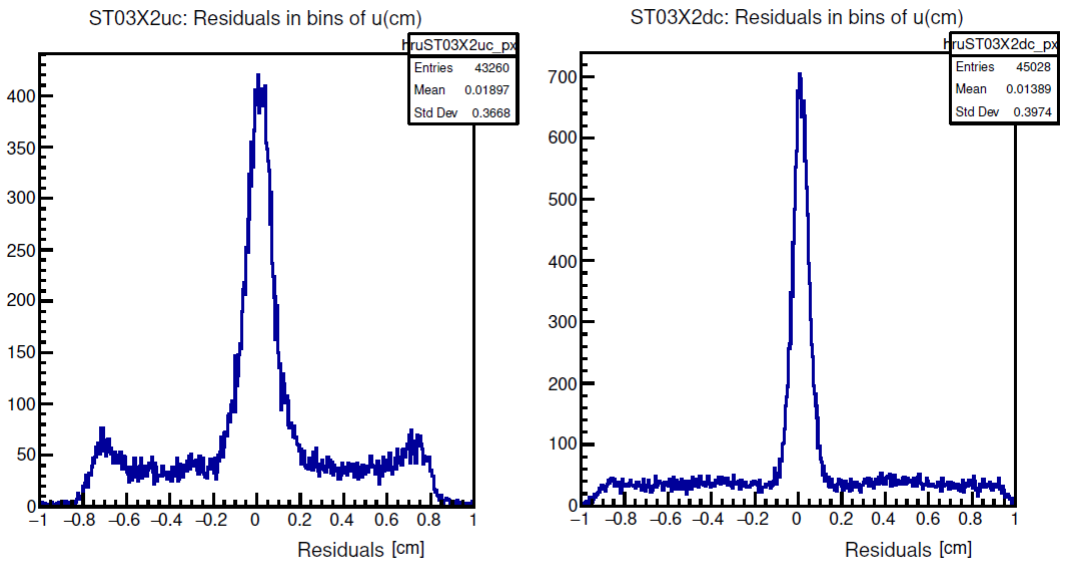

Figure 3.35: Residuals for X2 double layer, section c and run n. 287536